



HAL
open science

Wireless baseband transmission for short distance digital communication with circuits placed at cryogenic temperature

Furat Abayaje

► **To cite this version:**

Furat Abayaje. Wireless baseband transmission for short distance digital communication with circuits placed at cryogenic temperature. Micro and nanotechnologies/Microelectronics. Université Grenoble Alpes, 2017. English. NNT : 2017GREAT017 . tel-01647187

HAL Id: tel-01647187

<https://theses.hal.science/tel-01647187>

Submitted on 24 Nov 2017

HAL is a multi-disciplinary open access archive for the deposit and dissemination of scientific research documents, whether they are published or not. The documents may come from teaching and research institutions in France or abroad, or from public or private research centers.

L'archive ouverte pluridisciplinaire **HAL**, est destinée au dépôt et à la diffusion de documents scientifiques de niveau recherche, publiés ou non, émanant des établissements d'enseignement et de recherche français ou étrangers, des laboratoires publics ou privés.

THÈSE

Pour obtenir le grade de

DOCTEUR DE LA COMMUNAUTE UNIVERSITE GRENOBLE ALPES

Spécialité : **Nano Électronique et Nano Technologies**

Arrêté ministériel : 7 août 2006

Présentée par

Furat ABAYAJE

Thèse dirigée par **Pascal FEBVRE**

Préparée au sein du **Laboratoire IMEP-LAHC**
dans l'**École Doctorale E.E.A.T.S**

**Transmission numérique sans fil en bande
de base pour la communication à courte
distance avec des circuits cryogéniques**

Thèse soutenue publiquement le **13 mars 2017**
devant le jury composé de:

Mr. Pascal XAVIER

Professeur à l'Université Grenoble Alpes (Président)

Mr. Matthieu CHATRAS

Professeur à l'Université de Limoges (Rapporteur)

Mr. Emanuel RADOI

Professeur à l'Université de Bretagne (Rapporteur)

Mr. Faouzi BOUSSAHA

Ingénieur de recherche à l'Observatoire de Paris (Examineur)

Mr. Gilles SICARD

Senior scientist au CEA Grenoble (Examineur)

Mr. Pascal FEBVRE

Maitre de Conférences à l'Université Savoie Mont Blanc



To the lord of time who surely will come...

Acknowledgements

Firstly, I would like to express my sincere gratitude to my supervisor Dr. Pascal FEBVRE for the continuous support of my Ph.D. study and related research, for his patience, motivation, and immense knowledge. His guidance helped me in all the time of research and writing of this thesis. I could not have imagined having a better advisor and mentor for my Ph.D. study.

I would appreciate the engineers in IMEP-LAHC: Magali ASTIC, Nicolas CARROA, Antoine GACHON, Serge BAS, and Xavier MESCOT for their strong support during the experiments.

I would like thank my colleges and friends in IMEP-LAHC Chambéry and Grenoble, Aline COELHO DE SOUZA, Matthieu BERTRAND, Zyad ISKANDAR, Frederic PARMENT, Hamza HALLAK ELWAN, Abdel Kader TAIBI, Habab RZAIGUI, Ramin KHAYATZADEH, Nisrine ARAB, Mohamad AWAD, Ali Waqar AZIM, Abdelaziz HAMANI, Theano KARATSORI, Christofors THEODOROU, Elodi JORDAN, Victoria NASSERDDINE, Anh Tu HO, Maher HAMDE, Ines KHARRAT, Fatoumata SY, and so on.

Also, I would like to thank: Dalhila ALOUANI, Fernanda DOS-REIS, Isabelle MICHELIN, Valerie MISCIOSCIA, Brigitte RASOLOFONIAINA, and Annaick MOREAU.

Last but not the least, I would like to thank my family: my parents and to my brothers and sisters for supporting me spiritually throughout writing this thesis and my life in general.

Finally, I would like to thank my wife TOHALA Luma and my children: Sarah, Hassan, and Yasmin. You sacrificed your own happiness, just so that I could be happy.

Grenoble, 13 Mars 2017

F.AB.

Abstract

Rapid Single-Flux-Quantum (RSFQ) logic circuits based on superconducting Josephson junctions are used to generate, process and transmit very short quantized pulses whose area is the quantum of magnetic flux $h/2e$ and corresponds to 2.07 mV.ps. Such circuits are used to process signals at very high speed with clock frequencies in the 10-120 GHz range and a power consumption about 100 to 1000 times lower than their best available semiconductor counterparts (including the cost of cooling down to 4.2K). RSFQ logic is an interesting alternative for supercomputers and offers unsurpassed performances for processing microwave signals on the fly. Once digital signals are processed at cryogenic temperature the key challenge is to transfer at room temperature the low-voltage output digital signals (about 200-1000 μ V) at high rates of about 1-10Gbps per channel, by limiting the thermal burden on the cryogenic system, in order to build high performance high throughput systems.

A solution is to transmit the signals with a wireless emitting-receiving antenna set with a suitable bandwidth. This work examines several wireless baseband transmission systems in a short distance configuration, associated to the distance between the cryogenic and room temperature stages, for data rates in the range of a few Gbps. It elaborates on four crucial issues:

- ❖ the choice and study of the proper line codes to be used for baseband transmission of digital signals without the need for analogue modulations, such as Polar Return-to-Zero and Manchester encodings ;
- ❖ the study and selection of ultra-wide bandwidth antennas with a focus on small size Antipodal Vivaldi Antennas and monopole antennas to meet cryogenic constraints ;
- ❖ The study of the Bit Error Rate (BER) of the transmitting system. Two methods were developed to recover the digital output signals and minimize the BER.
- ❖ The comparison between simulations and measurements to assess the performance of the overall system.

Key words: Manchester encoding, Polar RZ encoding, wireless baseband transmission, near field, high-data rate, small size antenna, ultra-wide band, UWB, Antipodal Vivaldi antenna, Monopole antenna, superconducting electronics, RSFQ

Résumé

Les circuits logiques "Rapid Single-Flux-Quantum" (RSFQ) à base de jonctions Josephson supraconductrices sont utilisés pour générer, traiter et transmettre des impulsions ultra-courtes dont l'aire quantifiée est celle du quantum de flux magnétique $h/2e$ et correspond à 2,07 mV.ps. De tels circuits sont utilisés pour traiter le signal à très haute fréquence avec des fréquences d'horloge dans la gamme 10-120 GHz et une puissance consommée environ 100 à 1000 fois plus faible (incluant le coût énergétique du refroidissement à 4,2 K) que celle des meilleurs circuits semi-conducteurs équivalents. La logique RSFQ est une alternative intéressante pour les super-ordinateurs et offre des performances inégalées pour traiter les signaux micro-ondes à la volée. Une fois les signaux numérisés et traités à température cryogénique, le défi principal est de transférer à température ambiante les signaux numériques de faible tension (dans la gamme 200-1000 μ V) à des débits de 1 à 10 Gbps par voie, tout en limitant la charge thermique sur le système de réfrigération cryogénique, afin de construire un système performant à très haut débit numérique.

Une solution à ce verrou est de transmettre les signaux par un système d'émission-réception sans fil avec la bande passante suffisante. Ce travail examine différents systèmes de transmission sans fil à courte distance, correspondant à la configuration physique entre les étages à températures cryogénique et ambiante, pour des taux de transmission de quelques Gbps. Il s'est construit sur quatre points cruciaux à résoudre:

- ❖ le choix et l'étude du codage numérique approprié pour être utilisé comme support de transmission en bande de base des signaux sans utiliser de modulation analogique, comme les codages Polar Return-to-Zero et Manchester ;
- ❖ l'étude et la sélection d'antennes ultra large bande avec une attention particulière portée sur les antennes Vivaldi antipodales et les antennes monopôles pour satisfaire aux contraintes cryogéniques ;
- ❖ l'étude du taux d'erreur du système de transmission. Deux méthodes ont été développées pour récupérer les signaux numériques et minimiser le taux d'erreur ;
- ❖ la comparaison entre simulations et mesures afin d'évaluer la performance du système global.

Mots-clés: codage Manchester, codage Polar RZ, transmission sans fil en bande de base, champ proche, taux de transmission élevé, antenne miniature, ultra large bande, UWB, antenne Vivaldi antipodale, antenne monopôle, électronique supraconductrice, RSFQ

Contents

ACKNOWLEDGEMENTS	I
ABSTRACT	II
RESUME	III
LIST OF FIGURES	VII
LIST OF TABLES	XIV
ACRONYMES	XV
1 SUPERCONDUCTING CIRCUITS AND ENCODINGS	1
1.1 Introduction.....	1
1.2 Digital processing and superconductivity.....	2
1.2.1 Introduction to superconductivity.....	2
1.2.2 Analog Superconductor Quantum Interference Device (SQUID)	3
1.2.3 Rapid single flux quantum (RSFQ) digital electronics.....	4
1.2.4 Digital SQUID magnetometer	6
1.3 Presentation of the objective	7
1.4 Coding of Rapid Single-Flux Quantum signal.....	10
1.4.1 Desirable properties for line codes	11
1.4.2 Line Codes used to transmit digital baseband signals.....	12
1.4.3 Choice of Wireless Baseband Transmission encodings.....	13
1.4.4 Simulation of Manchester and Polar RZ encoded signals	17
1.5 Organization of thesis.....	19
2 ANALYSIS OF WIRELESS BASEBAND TRANSMISSION FOR TRANSMISSION OF RSFQ DIGITAL SIGNALS	24
2.1 Introduction.....	24
2.2 Wireless Baseband Transmission concept	25
2.3 Transfer functions of UWB transmission antenna system	26
2.3.1 Definition of transfer functions	26
2.4 Baseband Transmission of line codes.....	35

2.5	Estimation BER for Polar RZ and Manchester encodings	36
2.5.1	BER calculation based on averaging values of bit samples	36
2.5.2	BER calculation based on specific sampling of each bit	37
2.6	Baseband transmission of line codes at 1Gbps data rate	38
2.6.1	Transmission of the first harmonic of the digital signal	38
2.6.2	Use of higher harmonics of the digital signal	41
2.7	Conclusion	46
3	STUDY OF UWB ANTENNAS FOR WIRELESS BASEBAND TRANSMISSION	49
3.1	Introduction.....	49
3.2	Fundamental properties of antennas.....	50
3.2.1	Input impedance	50
3.2.2	Radiation Pattern.....	51
3.2.3	Bandwidth	52
3.2.4	Friis Transmission Formula.....	53
3.2.5	S-parameters	54
3.2.6	Radiated fields regions	57
3.3	Design of compact Antipodal Vivaldi Antennas	62
3.3.1	Antipodal Vivaldi Antenna geometry and design.....	63
3.3.2	Results and analysis.....	65
3.4	Improvement of radiation characteristics by using Tapered Slot Edge (TSE)	76
3.4.1	Results and discussion.....	76
3.5	Comparison of AVAs using a slot or a TSE.....	82
3.5.1	Measured return loss of AVA with TSE and slot.....	82
3.5.2	Measured VSWR and gain of AVA with TSE and slot.....	84
3.6	Design of a small size UWB monopole antenna.....	85
3.6.1	Results and discussion.....	85
3.7	SATIMO dual ridge horn antenna.....	89
3.8	Conclusion	91
4	EXPERIMENTAL ASSESSMENT OF WBT WITH A SHORT DISTANCE CONFIGURATION.....	96
4.1	Introduction.....	96
4.2	Small size antennas used for wireless baseband transmission in a short distance configuration	97
4.2.1	WBT measurements with Antipodal Vivaldi Antenna.....	98

4.2.2	Monopole UWB antennas for WBT	110
4.2.3	Large size horn antenna for WBT	112
4.3	Conclusion	114
5	CONCLUSIONS AND PROSPECTS.....	115
	APPENDIX A: POWER SPECTRAL DENSITY (PSD) OF LINE CODES.....	117
	APPENDIX B: A COMPACT ANTIPODAL VIVALDI ANTENNA (AVA).....	121

List of Figures

1.1	Josephson tunnel junction. (a) Physical structure in niobium technology. (b) Circuit symbol.....	2
1.2	(a) Superconductor and non-superconductor resistance versus temperature. (b) Meissner effect: superconductor's magnetic flux lines above and below critical temperature. (http://www.globalspec.com).....	3
1.3	(a) A highly sensitive magnetometer: the superconducting quantum interference device (SQUID). (b) SQUID based on Nb/Al-AlOx/Nb Josephson junctions. (c) SQUID schematics.....	3
1.4	Shunted-Josephson junction (left), current-voltage characteristics (center), Rapid signal flux quantum logic (right).....	4
1.5	D-flip-flop RSFQ cell, layout size is $110 \times 60 \mu\text{m}^2$	5
1.6	Chip photograph of a digital SQUID magnetometer, fabricated at FLUXONICS Foundry: (http://www.fluxonics.eu). (1) dc/SFQ converter, (2) balanced comparator, (3) output interface (SFQ/dc converter), (4) pickup loop with 0.9 mm^2 area, and (5) line for inductively coupled input current.....	6
1.7	(a) Typical output digital signal of a RSFQ superconducting electronics circuit. In black the original signal. In blue the intrinsically filtered signal of interest. (b) Block diagram of short distance configuration setup for wireless transmission of digital data from the cryogenic environment. D is the typical diameter of the cryogenic windows, of about 5 to 20mm.	8
1.8	Line codes schemes (left). An arbitrary bit pattern in various binary line codes formats (right).	12
1.9	Spectral distributions of several types of line codes. There is no dc-component with Manchester and Bipolar NRZ while Polar RZ and NRZ exhibit a dc-component. http://article.sapub.org/10.5923.j.ijnc.20160605.02.html	13
1.10	Pulse shapes of "1" and "0" for Polar RZ line code.....	14
1.11	Power spectrum density versus normalized frequency for the Polar RZ line code where t is the duration of bit. PSD value is different from 0 at dc frequency (there is a dc-component).	15
1.12	Pulse shapes of "1" and "0" for Manchester line code.....	15
1.13	Power spectrum density versus normalized frequency for the Manchester line code where t is the duration of bit. There is no dc-component.	16

1.14	Manchester encoded signal at 1Gbps data rate with random data input (20 bits code pattern). The data input is [10110010110101011001] (top). Fast Fourier Transform of Manchester (bottom). There is no dc-component.	17
1.15	Polar RZ encoded signal at high data rate of 1Gbps with random data input (20 bits code pattern). The data input is [10110010110101011001] (top). Fast Fourier Transform of Polar RZ (bottom). There is a dc-component.....	18
1.16	Polar RZ line code signal at a data rate of 1Gbps with random data input. Number of zeros is equal to number of ones at data input sequence. There is no a dc-component.	19
2.1	Transceiver architecture. Mod (modulator), BPF (band-pass filter), PA (power amplifier), LAN (low-noise amplifier), and Demod (demodulator). (a) Conventional wireless system. (b) Wireless baseband transmission system.	25
2.2	Transmitting-receiving antennas system model.	27
2.3	<i>ABCD</i> parameters and S-parameters of the antenna system.....	28
2.4	Procedure used to simulate the transmission of Polar RZ and Manchester line codes in the frequency domain with an antenna transmission transfer function. FT: Fourier Transform; T.F: Transfer Function; DSP: Digital Signal Processing.	35
2.5	S-parameters used for the set of emitting and receiving antennas. f_L and f_H represent respectively the lower and the upper theoretical frequency of the antenna bandwidth.....	35
2.6	Sampling method used to calculate the output digital signal and deduce the BER, illustrated for Polar RZ and Manchester encoding for which the digital sequence [1 0 1] is represented. Only the samples of the first half of each bit are used to calculate the average value of the half-bit. This average is transformed in a "1" or "-1" level, depending on the sign of the average. The second part of the bit is automatically set to the "0" level according to the Polar RZ encoding used to find the bits. The sequence of the two levels of the bit, "-1&0" or "1&0", corresponds respectively to a digital "0" or "1" with Polar RZ encoding. The resulting digital output signal is also valid for Manchester encoding.....	36
2.7	Approach to calculate the BER of digital output signal based on specific sampling.	37
2.8	Simulations of Polar RZ (left) and Manchester (right) line codes at 1Gbps for a 20 bits input sequence [10110010110101011001]. The antenna bandwidth $f_H - f_L$ is supposed infinite in theory and limited by the sampling rate in practice. (a) Data input of encoded signal (b) Frequency spectrum at input of transmission antenna. (c) Output signal at the receiver antenna. (d) Inverse FFT of the output signal of the receiving antenna superposed with the digital input signal.....	38
2.9	Simulations of the transmission of Polar RZ (left) and Manchester (right) line codes across a theoretical set of antennas with 0-2 GHz bandwidth according to the S-parameters of Figure 2.5. (a) Input data with Polar RZ and Manchester encoding at 1Gbps. (b) FFT of encoded signals where the transmission bandwidth is limited to 0-2 GHz. (c) Comparison of input and output signals.	39
2.10	BER versus bandwidth of transmission for a digital signal at 1Gbps made of a random pattern of 2^{20} bits, with Polar RZ and Manchester line codes.	40

2.11	BER versus SNR for Polar RZ and Manchester encodings. A gaussian noise has been added to the input or the output digital signal for a code pattern of 2^{16} random bits with 12 samples per bit. The bandwidth is 1GHz (0.5-1.5 GHz).....	41
2.12	Simulated FFT for (a) Polar RZ encoding and, (b) Manchester encoding, with a data rate of 1Gbps and a 1000 bit-code pattern. Results are shown for 24, 12 and 8 samples per bit.....	42
2.13	Simulations of FFTs for two encoded signals at a data rate of 1Gbps with a 1000-bit code pattern. (a) Manchester and Polar RZ encoded signals using 12 samples per bit (BW=4-6GHz). (b) Manchester and Polar RZ encoded signals using 24 samples per bit (BW= 4-12GHz)	43
2.14	Simulations of WBT with Polar RZ encoded signal at a data rate of 1Gbps. (a) with a 20 bits code pattern using 12 samples per bit. The bandwidth is 4-6 GHz. (b) with a 20 bits code pattern using 24 samples per bit. The bandwidth is 4-12 GHz. (c) with 2^{16} bits code pattern using 12 samples per bit. The bandwidth is 4-6 GHz. (d) with 2^{16} bits code pattern using 24 samples per bit. The bandwidth is 4-12 GHz.	44
2.15	Simulations of WBT with Manchester encoded signal at a data rate of 1Gbps. (a) with a 20 bits code pattern using 12 samples per bit. The bandwidth is 4-6 GHz. (b) with a 20 bits code pattern using 24 samples per bit. The bandwidth is 4-12 GHz. (c) with a 2^{16} bits code pattern using 12 samples per bit. The bandwidth is 4-6 GHz. (d) with a 2^{16} bits code pattern using 24 samples per bit. The bandwidth is 4-12 GHz.	45
2.16	Simulation of WBT for two encodings at a data rate of 2Gbps with a 2^{16} bits code pattern using 6 samples per bit. The bandwidth ranges from 4 GHz to 6 GHz. (a) Polar RZ encoding. (b) Manchester encoding.	45
3.1	The radiation pattern of a dipole antenna. Here, the radiation pattern has a main lobe, side lobes and a back lobe.	51
3.2	Transmission & reception antennas separated by the distance R.	53
3.3	Signal flow graph for S-parameters interpretation in voltages.....	55
3.4	Definitions of <i>ABCD</i> parameters and S-parameters.....	56
3.5	Field regions for antennas equal to one-half wavelength or shorter than one-half wavelength.	57
3.6	Geometrical arrangement of a dipole antenna (left) and electric field orientation (right). The charges oscillate around the origin along the z axis with infinitesimal amplitude. The vector potential at any point is parallel to the z axis, and oscillates at the same frequency as the dipole, with a phase difference and amplitude depending on the distance from the origin.	58
3.7	(a) Simulated return loss and (b) layout of the AVA. Total size ($L*W$) is $37*21 \text{ mm}^2$ on FR4 substrate thickness with $h=1.6\text{mm}$, $Wf=3\text{mm}$, and $WP =20\text{mm}$	64
3.8	(a) Simulated return loss and (b) layout of AVA. Total size ($L * W$) is $37 * 21\text{mm}^2$ with FR4 substrate thickness $h = 1.6\text{mm}$, $Wf = 2\text{mm}$, and $WP = 20\text{mm}$. The ground plane is shifted by $S= 1\text{mm}$	65
3.9	(a) Return loss performance of the proposed antenna with and without the slot. (b) Surface current distribution of the proposed AVA at 7GHz with and without the slot.....	66

3.10	Return loss performance of the proposed antenna for different widths, lengths, and positions of slot etched on both sides of the antenna. Position of slot: (a) $g=9.5$ (b) $g=8.5$	67
3.11	Return loss simulations of the proposed antenna for different widths, lengths, and positions of the slot etched on the ground plane only. (a) Slot length =6mm, position of slot $g=9.5$ mm, slot widths: 0.5, 1, 1.5, and 2 mm. (b) Slot width of =0.5mm, position of slot $g=9.5$ mm, slot lengths: 3, 5, 6, and 7mm. (c) slot length =6mm, width of slot=0.5mm, positions of slot: 7.5, 8.5, 9.5, and 11.5mm.	68
3.12	Return loss with a ground plane shift of $S=0, 1, 2, 3$ mm. (a) layout of the shifted ground plane (S) with an extended input microstrip line. (b) S_{11} with ground plane slot. (c) S_{11} without ground plane slot.....	69
3.13	Simulated VSWR and peak gain versus frequency for the AVA with a slot resonator and a grounded plane shifted by 1mm.	70
3.14	Simulated and measured radiation patterns of the AVA at 3.5, 7, 9, and 11 GHz. (a) Measured radiation patterns in E-plane. (b) Simulated radiation patterns in E-plane. (c) Measured radiation patterns in H-plane. (d) Simulated radiation patterns in H-plane.....	71
3.15	Simulations of surface current distributions of the AVA. (a) 3.5GHz. (b) 7GHz. (c) 9 GHz. (d) 11GHz.	72
3.16	Comparison of simulated and measured return loss of AVA.	73
3.17	Photograph of the fabricated AVA.	73
3.18	Measured S-parameters with two AVA distance from $R= 2$ cm placed in aligned configuration. (a) Setup of two AVA (b) Magnitude and phase of S_{11} . (c) Magnitude and phase of S_{21}	74
3.19	Measured, simulated return loss and schematic of AVA. Total size is $50*30\text{mm}^2$ with FR4 substrate thickness $h=1.6$ mm, $W_f =2.5$ mm. (a) Measured and simulated return loss versus frequency. (b) Schematic of AVA with slot on ground plane and shifted ground plane edge.	75
3.20	Schematic of the AVA with TSE on ground plane only: Top view (Left). Bottom view (Right).	76
3.21	Simulated return loss of AVA with and without TSE on ground plane only and with shifted ground plane.	77
3.22	Simulated and measured VSWR of AVA with a TSE structure.	77
3.23	Simulated and measured radiation patterns of AVA with TSE structure in E-plane (x-y) and H-plane (x-z) at 3.5 and 7 GHz. (a) H-plane at 3.5 GHz. (b) E-plane at 3.5 GHz. (c) H-plane at 7 GHz. (d) E-plane at 7 GHz.	78
3.24	Simulated and Measured radiation patterns of AVA (TSE structure) in E-plane (x-y) and H-plane (x-z) at 9 and 11 GHz. (a) H-plane at 9 GHz. (b) E-plane at 9 GHz. (c) H-plane at 11 GHz. (d) E-plane at 11 GHz.	79
3.25	Simulated return loss of the AVA for different widths and lengths of the substrate. (a) Change of length with fixed width of 21mm. (b) Change of width with fixed length of 37mm.	80

3.26	Measured and simulated gain of the designed AVA with and without TSE structure on ground plane.....	81
3.27	Comparison of simulated and measured return loss of AVA with TSE structure.....	82
3.28	Photograph of the fabricated AVA.....	82
3.29	Measured return loss of AVAs with slot and TSE structure.	83
3.30	Simulated current distribution at 7 GHz for: (a) AVA antenna with etched slot. (b) AVA antenna with etched TSE structure.....	83
3.31	Measured VSWR of AVAs with slot and TSE structure.	84
3.32	Measured gains of AVAs with slot and TSE structure.....	84
3.33	Configuration of the monopole antenna. (a) Bottom view. (b). Top view.	85
3.34	Measured and simulated return loss of the monopole antenna.....	86
3.35	Measured radiation patterns of the designed monopole antenna in <i>E</i> -plane at (a) 4.5 GHz, (b) 8GHz, (c) 9.5GHz, and (d) 10.5GHz.....	86
3.36	Measured radiation patterns of the designed monopole antenna in <i>H</i> -plane at (a) 4.5 GHz, (b) 8GHz, (c) 9.5GHz, and (d) 10.5GHz.....	87
3.37	Simulated and measured VSWR of the monopole antenna.....	88
3.38	Simulated and measured gain of the designed monopole antenna	88
3.39	Photograph of the fabricated monopole antenna. Size is 18mm × 12mm.	88
3.40	The SATIMO 2GHz–32 GHz dual ridge horn antenna. The nominal impedance is 50 ohms with return loss better than -10dB (VSWR < 1.9).....	89
3.41	Return loss of the SATIMO dual ridge horn antenna.....	89
4.1	Far-field region boundary according to the number of points per bit for (a) antipodal Vivaldi antenna ($D = 3.7\text{cm}$ and $f_{\text{boundary}} = 8.1\text{GHz}$) and (b) horn antenna ($D = 10.5\text{cm}$ and $f_{\text{boundary}} = 2.9\text{GHz}$).	97
4.2	Setup of two antipodal Vivaldi antennas placed in an aligned configuration. The S-parameters of the antenna system were measured using an Anritsu 37369A Vector Network Analyzer (VNA).....	98
4.3	Measured S-parameters of the set of two antipodal Vivaldi antennas placed in an aligned configuration. (a) S_{11} at 2 cm distance. (b) S_{21} at 2 cm distance. (c) S_{11} at 10 cm distance. (d) S_{21} at 10 cm distance.	99
4.4	Simulations of WBT for a Polar RZ encoded signal at 1Gbps with 12 points per bit and 1000-bit code pattern, BER are obtained after 100 simulations with random input sequences.(a) d=2cm. (b) d=4cm. (c) d=8cm. (d) d=12cm. Measured S-parameters were used to perform simulations.	100
4.5	Simulations of WBT for a Manchester encoded signal at 1Gbps with 12 points per bit and 1000-bit code pattern, BER are obtained after 100 simulations with random input sequences.(a) d=2cm. (b) d=4cm. (c) d=8cm. (d) d=12cm. Measured S-parameters were used to perform simulations.	101

4.6	Simulations of WBT for a Polar RZ encoded signal at 2Gbps with 6 points per bit and 1000-bit code pattern, BER are obtained after 100 simulations with random input sequences.(a) d=2cm. (b) d=4cm. (c) d=8cm. (d) d=12cm.	102
4.7	Simulations of WBT for a Manchester encoded signal at 2Gbps using a 100-loops input data with 6 points per bit and 1000-bit code pattern, BER are obtained after 100 simulations with random input sequences.(a) d=2cm. (b) d=4cm. (c) d=8cm. (d) d=12cm.	103
4.8	Simulated BER for polar RZ and Manchester encodings versus distance between two AVA antennas using 1000-bitcode pattern. (a) Data rate at 2Gbps with 6 points per bit. (b) Data rate at 1Gbps with 12 points per bit. Measured S-parameters were used to perform simulations.	103
4.9	Setup of two AVA placed in an aligned configuration for WBT. Encoded signal: Manchester and Polar RZ, AWG: Arbitrary Waveform Generator, DSO: Digital Sampling Oscilloscope, DSP: Digital signal processing (with Matlab).	104
4.10	Simulated spectrum of Polar RZ line code at a data rate of 1Gbps with 8 samples per bit.....	105
4.11	Measured 20-bit Polar RZ encoded signal at a data rate of 1Gbps with 12 points per bit for different distances between antennas: (a) d = 2cm. (b) d = 4cm. (c) d = 8cm. (d) d = 12cm.	106
4.12	Measured and simulated BER of Polar RZ encoding versus distance from 1cm to 15cm at a data rate of 1Gbps using two different random input signals for 20 and 1000-bit code patterns with 12 points per bit. (a) With a 20-bit code pattern. (b) With a 1000-bit code pattern.....	106
4.13	Measured and simulated BER of Polar RZ encoding versus distance from 1cm to 15cm at a data rate of 1Gbps for 20 and 1000-bit code patterns with 24 samples per bit. (a) With a 20-bit code pattern. (b) With a 1000-bit code pattern.	107
4.14	Measured and simulated BER for Polar RZ encoding versus distance antennas at a data rate of 1Gbps using 1000-bit code pattern with 12 and 24 samples per bit.	107
4.15	Measured transmission of a Manchester encoding at a data rate of 1Gbps with 12 points per bit for a 20-bit code pattern and different distances between antennas: (a) d=2cm. (b) d=4cm. (c) d=8cm. (d) d=12cm.	108
4.16	Measured and simulated BER of Manchester encoding versus distance at a data rate of 1Gbps using two different random input signals with 12 points per bit. (a) With a 20-bit code pattern. (b) With a 1000-bit code pattern.....	109
4.17	Measured and simulated BER of Manchester encoding versus distance at a data rate of 1Gbps with 24 points per bit. (a) With a 20-bit code pattern. (b) With a 1000-bit code pattern.....	109
4.18	Measured and simulated BER for Manchester encoding versus distance between antennas at a data rate of 1Gbps a using 1000-bit code pattern with 12 and 24 points per bit.	110
4.19	Setup with two monopole antennas placed face to face in short distance configuration.....	111
4.20	Measured transmission of two different line codes with two monopole antennas placed face to face at d = 4cm with 20 bit-code pattern and 12 points per bit at an input rate of 1Gbps. (a) Polar RZ encoding with input data from AWG, output measured by the DSO	

(20 points per bit), and detection results after Matlab processing. (b) Same curves for Manchester encoding.	111
4.21 Measured BER for (a) Manchester and (b) Polar RZ encodings versus distance between antennas at 1Gbps using 20, 500, 1000 bit-code streams and 12-points per bit.....	112
4.22 Setup with two SATIMO dual ridge horn antennas placed face to face.	113
4.23 Measured BER for (a) Polar RZ and (b) Manchester encodings versus distance between horn antennas at a data rate of 1Gbps with 1000-bit code pattern using 6 and 12 points per bit.	113

List of Tables

1.1 a comparison between several types of line codes.....	12
3.1 comparison of our customized AVA with some other AVA from the literature.....	63
3.2 summary of antennas designed in this chapter.....	90

Acronymes

ADC	Analogue-to-Digital converters
AIO _x	Aluminum Oxide
AVA	Antipodal Vivaldi Antenna
AWG	Arbitrary Waveform Generator
BER	Bit-Error-Rate
BW	Bandwidth
CVA	Coplanar Vivaldi Antenna
DC	Direct Current
Demod	Demodulator
DETTSA	Dual Exponentially Tapered Slot Antennas
DFT	Discret Fourier Transform
DSO	Digital Storage Oscilloscope
DSP	Digital Signal Processing
DS-SS	Direct Sequence Spread Spectrum
DSV	Digital Sum Variation
DSVA	Double Slot Vivaldi Antenna
EMC	Electromagnetic Compatibility
FBW	Fractional Bandwidth
FEM	Finite-Element Method
FFC	Federal Communication Commission
FFT	Fast Fourier Transform
FT	Fourier Transform
HFSS	High Frequency Structure Simulator
HTS	High Temperature Superconductor
IMEP	Institute of Microelectronics and Photonics electromagnetism
IR	Impulse Radio
LAHC	Laboratory microwave and characterization
LAN	Low-Noise Amplifier
Mod	modulator
Nb	Niobium
NRZ	Non Return-to-Zero
OFDM	Orthogonal Frequency Division Multiplexing
PSD	Power Spectral Density
RL	Return Loss
RSFQ	Rapid Signal Flux Quantum
RZ	Return-to-Zero
SATIMO	Applications Technology Corporation of Imaging Microwave SA
SFQ	Single Flux Quantum
SMA	SubMiniature version A Connector
SNR	Signal to Noise Ratio
SQUID	Superconducting Quantum Interference Device
TFA	Transfer Function Antenna
TSA	Taper Slot Antenna
UMR	Mixed Research Unit
UWB	Ultra-WideBand

VNA
VSWR
WBT

Vector Network Analyzer
Voltage Standing Wave Ratio
Wireless Baseband Transmission

1 Superconducting circuits and encodings

1.1 Introduction

For nearly 30 years, digital technology based semiconductor components demonstrated a continued and remarkable progress. Indeed, it is now possible to design integrated circuits on a silicon chip that can be made very compact, having up to several billion transistors operating at several GHz. On the other hand, superconducting digital circuits such as, for example, digital processors operating at clock frequencies of 30 GHz, digital high-speed switches at several gigabits per second (Gbps), and analogue-to-digital converters (ADC) that can process an instantaneous bandwidth of a few hundreds of MHz, can produce digital data at rates in the range of 40 to more than 100 Gbps per channel.

The increasing demand of data transmission rates, in particular for processing signals on microwave carriers, for instance for satellite telecommunications, requires the development of specific circuits and antennas. In particular, some systems that require fast processing at clock rates above 20 GHz rely on superconducting digital circuits to process the signals [1, 2]. For such circuits, which are cooled at the temperature of liquid helium, the processed data need to be transferred at room-temperature for further processing. To do so, since the number of wires needs to be limited to reduce the thermal load on the cryogenic system, a wireless link is an attractive solution. The feasibility has already been shown in the 8-12 GHz band [3] for the transmission of microwave analogue signals, like for instance signals at the intermediate frequency of radiofrequency mixers.

Superconducting electronics relies on materials such as niobium (Nb), NbN or YBaCuO. The basic element is the Josephson junction, which consists of two superconducting electrodes separated by a region of weakened superconductivity known as a weak link. The weak link is a thin layer of insulator, usually aluminum oxide (AlO_x) as shown in Figure 1.1. The Josephson junction is used to create unique and efficient architectures with unprecedented performance [4]. A new logic family was developed with promising features for ultra-high speed signal processing. Digital circuits are based on the storage and transmission of quanta of magnetic flux: the data is stored in form of magnetic flux quanta and transmitted in the form of SFQ voltage pulses. Called Rapid Single Flux Quantum (RSFQ), this technology has no counterpart in semiconductor electronics. RSFQ logic can operate in complex circuits at clock frequencies beyond 100 GHz. The basic RSFQ structure is a superconducting ring that contains one Josephson junction with an external shunt resistance. RSFQ circuits used for transmitting digital data in the form of pico-second voltage pulses are based on the use of shunted Josephson junctions of micrometer or sub-micrometer dimensions [1-10].

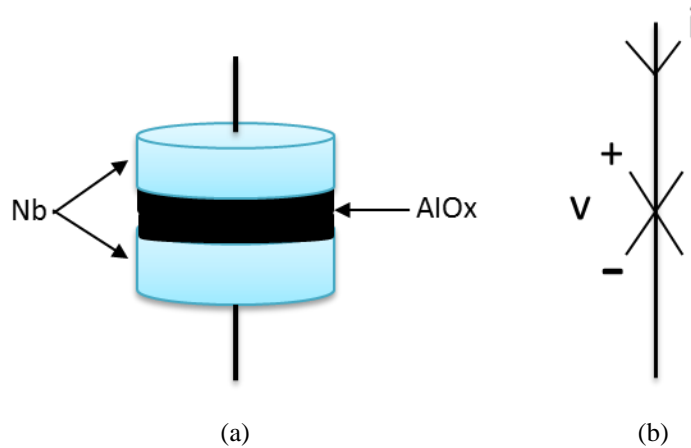


Figure 1.1 Josephson tunnel junction. (a) Physical structure in niobium technology. (b) Circuit symbol.

1.2 Digital processing and superconductivity

Superconductivity is a unique property of certain materials which is mainly characterized by:

- ❖ zero resistance to the flow of dc electrical current;
- ❖ the ability to screen out magnetic fields (perfect diamagnetism);
- ❖ quantum mechanical coherence effects – magnetic flux quantization and the Josephson effects.

1.2.1 Introduction to superconductivity

Superconductivity is the phenomenon of exactly zero electrical resistance. The expulsion of magnetic fields occurs when cooled below a characteristic critical temperature. The value of this critical temperature varies from material to material. Conventional superconductors usually have critical temperatures ranging from around 20 K to less than 1 K. It was discovered by the Dutch physicist Heike Kamerlingh Onnes on April 8, 1911 in Leiden. Like ferromagnetism and atomic spectral lines, superconductivity is a quantum mechanical phenomenon. It is characterized by the Meissner effect, the complete ejection of magnetic field lines from the interior of the superconductor as it transitions into the superconducting state. An electric current flowing through a loop of superconducting wire can persist indefinitely with no power source. There are many superconductors like mercury niobium-tin, lanthanum-baryum-copper oxides, and Yttrium-Baryum-Copper oxides [5, 7]. Superconductor materials can transport charges with no resistance, and hence release no heat, sound, or other energy forms.

When the temperature decreases the material resistance progressively decreases until it reaches a critical temperature. At this point resistance drops off, often to zero, as shown in Figure 1.2 (a). When the superconductor is cooled down below its critical temperature, the ejection of magnetic flux takes place as shown Figure 1.2 (b).

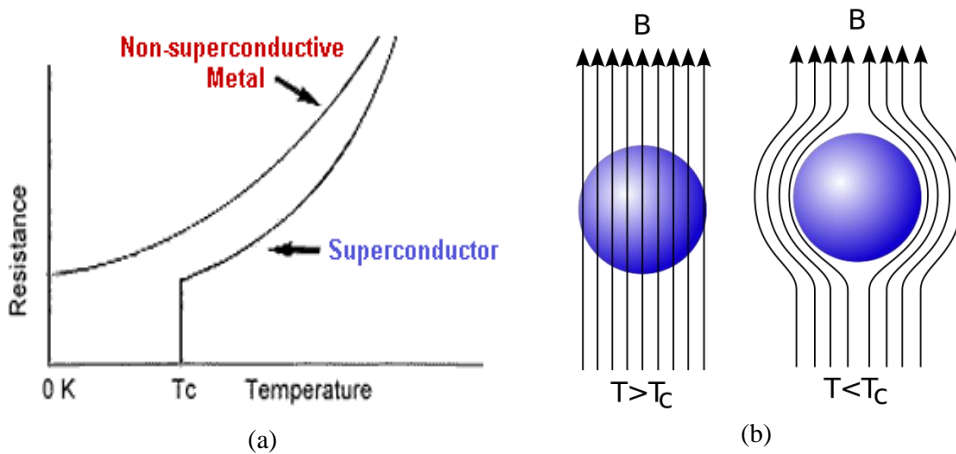


Figure 1.2 (a) Superconductor and non-superconductor resistance versus temperature. (b) Meissner effect: superconductor's magnetic flux lines above and below critical temperature. (<http://www.globalspec.com>).

1.2.2 Analog Superconductor Quantum Interference Device (SQUID)

When one or more Josephson junctions are connected in a superconducting loop, a superconducting quantum interference device (SQUID) is formed as shown in figure 1.3. Since SQUID are the basic building blocks of many superconducting circuits, knowledge of their basic operation facilitates the understanding of more complex circuits. Because the entire loop in a SQUID is superconducting, the current flowing through the loop may be described in terms of a macroscopic electron wave function possessing both magnitude and phase [1-9]. The SQUIDs can be configured as magnetometers to measure all components of the local magnetic field or as gradiometers to remove components of magnetic fields created by remote sources [14]. SQUID magnetometers measure faint magnetic fields and are known as the most sensitive magnetic field sensors. They are used in various fields, such as: material evaluation, bio-magnetism, solid-state physics, medicine with magnetoencephalography and magnetocardiography, archeology, earthquake detection, subsoil sounding for hydrogeology and environmental purposes [1-14].

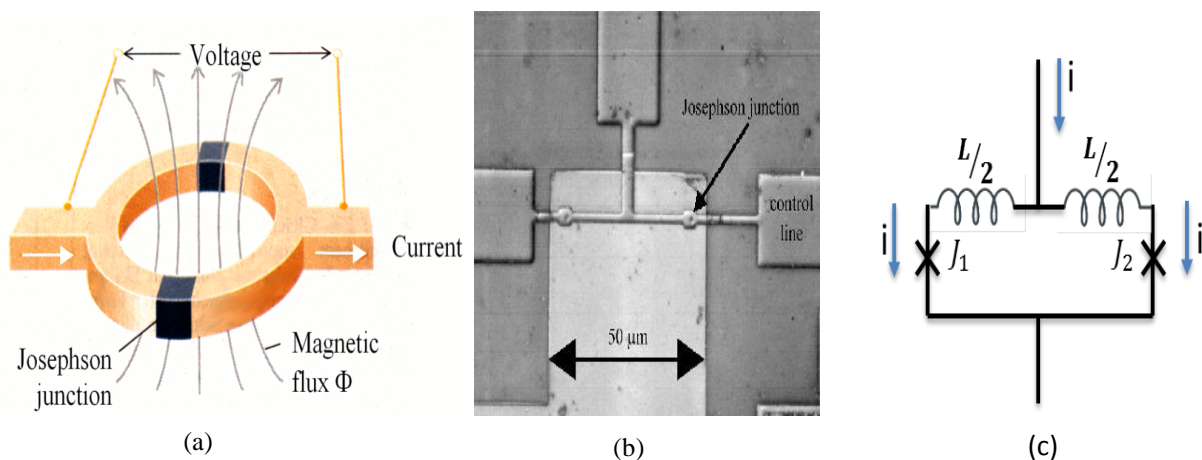


Figure 1.3 (a) A highly sensitive magnetometer: the superconducting quantum interference device (SQUID). (b) SQUID based on Nb/Al-AlO_x/Nb Josephson junctions. (c) SQUID schematics.

There are two main types of SQUIDS: DC-SQUID (Direct Current) and RF-SQUID (Radio Frequency), invented in 1964-1965 by Robert Jaklevic and co-workers [1-5]. The RF-SQUID is based on the AC Josephson effect and uses only one Josephson junction while the DC-SQUID is based on the DC Josephson effect and consists of two Josephson junctions mounted in parallel in a superconducting loop. The RF-SQUID is less sensitive compared to DC-SQUID but is cheaper and easier to manufacture in smaller quantities. Most of the commercially available superconductive magnetic sensors at present are DC-SQUID, which can detect less than 10^{-6} of the flux quantum in a superconductor, Φ_0 ($= 2.07 \times 10^{-15}$ Wb).

1.2.3 Rapid single flux quantum (RSFQ) digital electronics

In electronics, rapid single flux quantum (RSFQ) [1] is a digital electronics technology that relies on quantum effects in superconducting devices, namely Josephson junctions, to process digital signals. Josephson junctions are the active elements for RSFQ electronics, just as transistors are the active elements for semiconductor electronics. However, RSFQ is not a quantum computing technology in the traditional sense. Even so, RSFQ is very different from the traditional CMOS transistor technology used in every day computers. Since it is based on superconductors, a cryogenic environment is required, the digital information is carried by magnetic flux quanta that are produced by Josephson junctions, instead of transistors in semiconductor electronics. The magnetic flux quanta are carried by picosecond-duration voltage pulses that travel on superconducting transmission lines, instead of static voltage levels in semiconductor electronics. The area of the quantized voltage pulses that carry single magnetic flux quanta is constant. Depending on the parameters of the Josephson junctions, the pulses can be as narrow as 1 picosecond with an amplitude of about 2 mV, or broader (typically 5–10 picoseconds) with a lower amplitude.

RSFQ devices are much faster because the junctions are shunted externally with a resistor. Logic functions are built around the voltage pulses that occur each time a flux quantum enters or leaves the superconductor loop. The non-hysteretic current-voltage characteristics and the RSFQ logic principle are shown in figure 1.4.

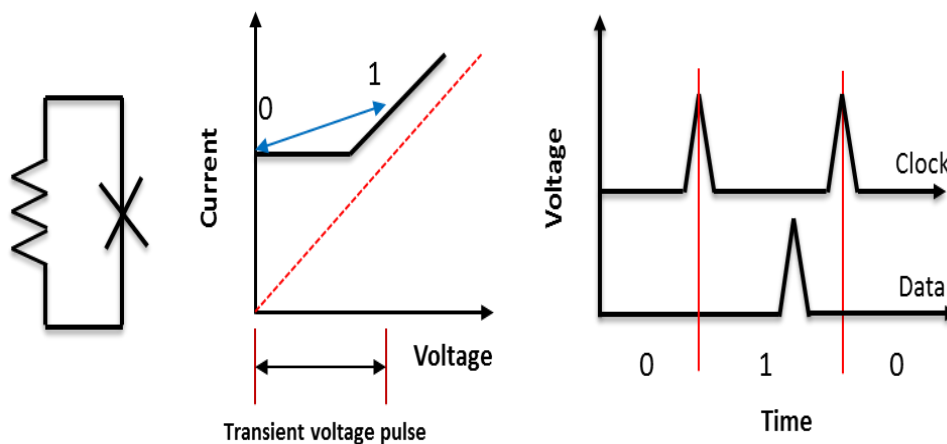


Figure 1.4 Shunted-Josephson junction (left), current-voltage characteristics (center), Rapid signal flux quantum logic (right).

Since pulses usually propagate on superconducting lines, their dispersion is limited and usually negligible if no spectral component of the pulse is above the frequency of the energy gap of the superconductor [10, 11]. In our case, the FLUXONICS technology is used, where the frequency can reach 30GHz. In fact, data rates at clock frequencies higher than 750 GHz have already been experimentally demonstrated for RSFQ toggle flip-flops having simple gates with $0.25\mu\text{m}$ linewidth [1-12]. There are many examples of RSFQ cells and circuits such as: flip-flop, AND, NOT, XOR gates, and A/D converters. Figure 1.5 shows an example of D-flip-flop cell.

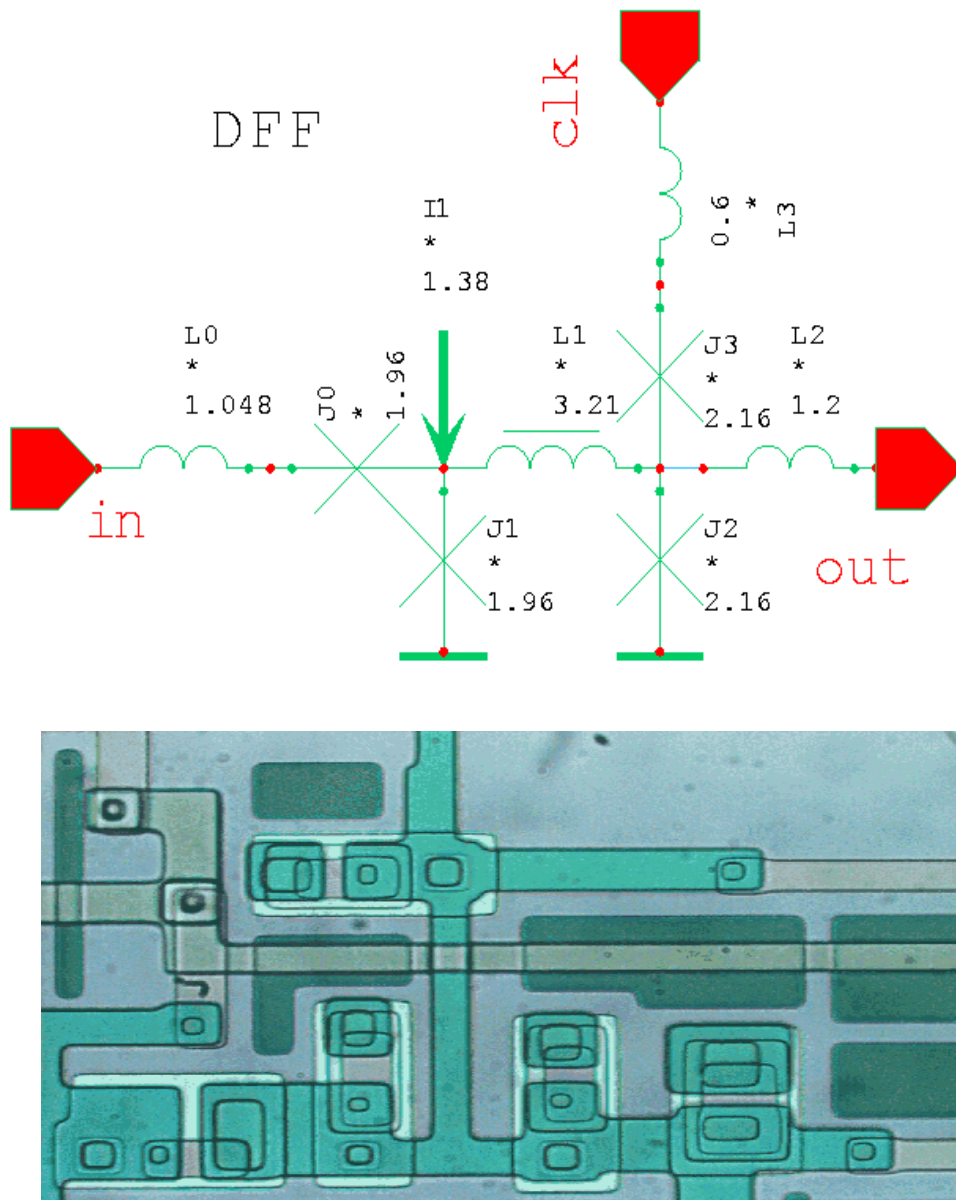


Figure 1.5 D-flip-flop RSFQ cell, layout size is $110 \times 60 \mu\text{m}^2$.
<http://www.physics.sunysb.edu/Physics/RSFQ/Lib/AR/tbi2.html>

1.2.4 Digital SQUID magnetometer

In the eighties, a digital SQUID based on superconductive latching logic circuits has been designed and fabricated [15, 16]. The digital SQUID carries out the digital feedback using a delta modulator. The superconducting digital magnetometer is based on a double or single junction SQUID. It has a fine sensitivity, with a large dynamic range and the ability to handle rapid signals at high slew rates. The slew rate of the digital SQUID magnetometer, which corresponds to the bandwidth of the measurable magnetic field, is much higher than that of the conventional SQUID due to the high-speed operation of SFQ readout circuits. The digital SQUID magnetometer has a wide dynamic range compared with the conventional SQUID. The SQUID can receive a composite signal, including the analog signal, a correction signal, and a high frequency dither signal [12]. For example figure 1.6 shows a chip photograph of a digital SQUID magnetometer with a pickup antenna with a dimension of 0.9mm^2 .

Analog SQUIDs are suitable devices to detect very weak magnetic fields, far below the strength of the Earth field. The application of the superconducting rapid single flux quantum (RSFQ) digital electronics for high sensitive measurement of magnetic fields by using digital magnetometers can bring significant advantages to conventional analog SQUID applications, especially in terms of slew rate and dynamic range. In the digital SQUID, SFQ circuits are used to control and measure SFQ pulses outputted by the SQUID loop. The digital SQUID is an oversampling delta analog-to-digital converter [9-14]. This makes superconducting digital devices also interesting for applications in unshielded environment exposed to magnetic fields.

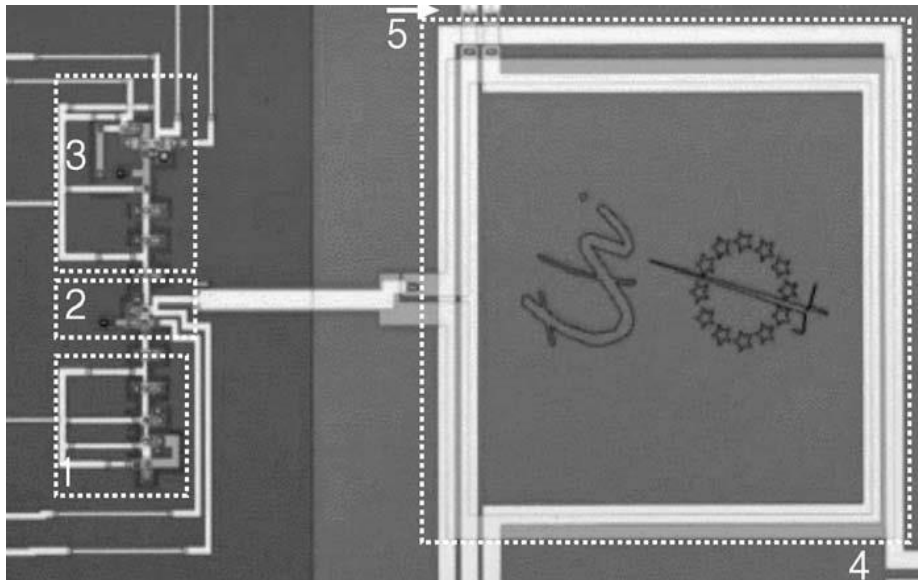


Figure 1.6 Chip photograph of a digital SQUID magnetometer, fabricated at FLUXONICS Foundry: (<http://www.fluxonics.eu>). (1) dc/SFQ converter, (2) balanced comparator, (3) output interface (SFQ/dc converter), (4) pickup loop with 0.9mm^2 area, and (5) line for inductively coupled input current.

1.3 Presentation of the objective

The Laboratory of Microwave and Characterization (IMEP-LAHC, CNRS UMR 5130) develops, in the frame of its superconducting electronics activities, ultrafast superconducting digital circuits that work with clock frequencies of several tens of GHz. Indeed, Rapid Single-Flux Quantum (RSFQ) electronics is able to process pulsed signals with clock rates ranging from tens to hundreds of GHz. At the same time, the fundamental property of magnetic flux quantization allows the same components to measure the magnetic field with unparalleled sensitivity, of the order of $1\text{-}10\text{ fT/Hz}^{1/2}$ in the case of analog sensors. In this framework a first scientific experiment was carried out in 2007 which allowed measuring the magnetic field with a fully digital superconducting magnetometer [12-14]. It is now required to develop a new generation of magnetometers with increased dynamic range. Currently the only known solution is linked to the development of digital magnetometers (digital SQUIDs).

The study of geophysical phenomena and space weather requires the installation of a network of advanced magnetometers that will be deployed, in successive stages, in different points of our planet. This requires the establishment of an infrastructure for the acquisition of the sensors measurements, allowing ultimately scientists to work on centralized data. Also the correlation of digital data between different sensors located in different parts of the world is essential to identify the sources of various phenomena: magnetic storms, earthquakes, etc. Superconductive technology offers unparalleled digital and mixed-signal circuit performance, advancing digital processing from baseband to RF stages. This allows elimination of analog filters and mixers with generally poorly controlled phase performance, causing inter-symbol interference and limiting the overall communication system performance.

In the previous sections, we have described the RSFQ circuits based on quantum effects in superconducting devices to process digital signals and measure magnetic field. An example of such signals is given in Figure 1.7 (a), where the challenge is to transmit this digital data without further need of down conversion. Consequently, after a proper on chip multiplexing of digital data to lower the rates in the 1 to 10 Gbps range, it is preferable to transmit data directly in the baseband with small size antenna placed in short distance configuration. Figure 1.7 (b) shows the simplified system architecture, where the RSFQ processing and the transmission antenna are located in 4K environment. In Figure 1.7 (b), one can see that the cryogenic system is composed of three stages at different temperatures of 4K, 20K, and room temperature, where the output of the RSFQ chip is composed of non-return to zero (NRZ) pulses in the 10-20Gbps range.

The short distance is fixed by the distance between the cryogenic stage at the temperature of liquid helium and the outer part of the cryogenic system at room temperature. We should point out that the broad bandwidth associated to such digital signals does not allow to simply consider that the antennas radiate in far- or near-field, since this feature depends on the frequency. We use the terminology of short distance configuration to discuss the respective positions of the transmitting and receiving antennas.

Since the instantaneous bandwidth to transmit is broad in our case, we investigated the ultra-wideband technology to solve our issue. Indeed, it is a common approach in wireless communication systems to transmit and receive pulses in the time domain, rather than sinusoidal waves processed in the frequency domain.

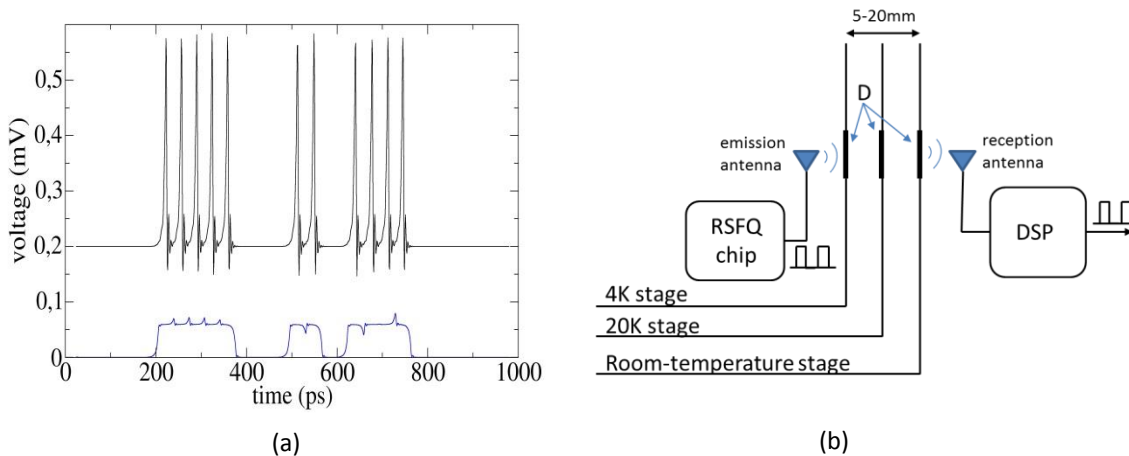


Figure 1.7 (a) Typical output digital signal of a RSFQ superconducting electronics circuit. In black the original signal. In blue the intrinsically filtered signal of interest. (b) Block diagram of short distance configuration setup for wireless transmission of digital data from the cryogenic environment. D is the typical diameter of the cryogenic windows, of about 5 to 20mm.

There are rapid developments in modern wireless communication systems to meet the increasing demand for high data rate transmissions. Wideband wireless communication schemes such as Ultra-Wideband (UWB) [17] and impulse radio (IR) [18] modulation have attracted a lot of attention. The Wireless Baseband Transmission (WBT) scheme is different from conventional wireless transmission schemes. It directly sends digital data through a set of antennas without any modulation technique.

In WBT communication systems, the key to transmit high-data rates using wireless link is the spectrum, since the demand for the data rate is directly translated to demand for the available bandwidth. Thus, it is required to find unlicensed and suitable frequency bands over which we can run ultra-fast applications. In our case we rely on superconducting digital circuits to process the signals [19, 20]. For such circuits which are cooled at the temperature of liquid helium the processed data need to be transferred at room temperature for further processing. To do so, since the number of wires needs to be limited to reduce the thermal load of the cryogenic system and feedback current loss of the cables, a wireless link is an attractive solution.

The use of WBT systems eliminates the need for local oscillator circuits and mixers used in conventional wireless systems and construction is to be simpler. In the design, the two factors which play an important role on the WBT system are the choice of antennas and transmission codes. The Manchester and Polar RZ encoded signals are proposed (detail in 1.4.3) to transmit and receive signal directly from an antenna at 1Gbps on a short distance. The Bit Error Rate (BER) is a key parameter that is used in assessing systems that transmit digital data from one location to another. A technique to calculate the bit error rate of line codes that can be used in baseband wireless communication system was developed.

In summary, for superconducting electronics applications we aim at transmitting and receiving digital signals directly from an antenna between two environments at different temperatures over a short distance. The wireless baseband transmission method has been chosen to transmit directly Polar RZ and

Manchester encoding signals through a set of two small antennas.

In this work, we have selected the data rate at 1Gbps, for several reasons:

- It is compatible with all devices and cables (limitation of channels, bandwidth, speed, processing, computers...etc.), that are used to process digital signals.
- The key to transmitting high-data rate using wireless link is spectrum, since the demand for the data rate is directly translated to the demand for the available bandwidth. Thus, it is required to find unlicensed and suitable frequency bands over which we can run the ultra-fast applications. The wide available bandwidth around UWB spectrum is suitable for 1Gbps wireless communications.
- It is compatible with logical RSFQ output rates of 10-30 Gbps after demultiplexing.

The thesis is structured as follows:

- ❖ The choice and performance of line codes to configure digital data coming from the RSFQ chip, such as Polar RZ and Manchester encodings, are presented in the next section.
- ❖ The concept of WBT and a study of a dedicated transmission system associated to the development of a MATLAB code for calculating the BER are presented in the next chapter.
- ❖ Several sets of antennas have been designed, simulated and fabricated for ultra-wideband applications on 1.6mm thick FR4 substrate. S_{11} and radiation pattern measurements have been done. All this is presented in chapter 3.
- ❖ WBT radiates directly data streams such as Polar RZ and Manchester encoded signals, at high data rate in the Gbps range at short distance through a set of antennas from an antenna and without any modulation technique. The antennas were arranged in an emitter-receiver with a distance range from 1-10 cm. The measured results of WBT at a data rate of 1Gbps and 2Gbps are presented in chapter 4.

1.4 Coding of Rapid Single-Flux Quantum signal

In baseband data transmission, the bits are mapped into two voltage levels for direct transmission without any frequency translation. Such a baseband data transmission is applicable to cable systems (both metallic and fiber) since the transmission bandwidth of most cable systems is in the baseband.

In telecommunication, a line code (also known as Digital Baseband Modulation or Digital Baseband transmission method) is a code chosen for use within a communication channel for baseband transmission purposes. Line coding is often used for digital data transport. In order to be transmitted over a digital communication system, an information signal must first be formatted so that it is represented by digital symbols (usually binary digits or bits). These digital or binary representations must be converted into electrical waveforms that are transmitted over the communication channel [21-25].

A broadband communication channel has a bandwidth that goes from some nonzero lower frequency to some upper frequency (for example the telephone channel uses a bandwidth going from 300Hz to 3400Hz.). Before transmitting a digital signal on a broadband channel, the digital signal must be modulated to shift the signal frequency into the channel bandwidth.

A baseband communication channel has bandwidth that goes from zero frequency to some upper frequency (example: Ethernet cable). A communication is “Base Band” when data is sent with no modulation. It means that the frequency of the digital signal suits the bandwidth of the communication medium. It enables to minimize the power loss, through the transmission line, because each medium has its own bandwidth and would act as a filter if its input signal was not in the frequency band.

As modulation often needs more bandwidth, baseband systems enable to save the bandwidth. This is one advantage of using baseband communication. Therefore the digital signal can be transmitted directly on a baseband channel. In baseband digital transmission, the electrical waveforms are pulses and conversion from digital data to digital waveform is known as line coding. Line codes involve converting a sequence of ‘1’s and ‘0’s to a time-domain signal (a sequence of pulses) suitable for transmission over a channel [21-22].

The baseband communication is often used nowadays and many line coding techniques have been proposed. They have become standards in telecommunication and computer networks. For instance the NRZ line code is used for RS 232 communications on the COM ports of computers, Manchester line code is used for Ethernet communications, Differential Manchester in Token Rings and Bipolar-Alternate Mark Inversion (AMI) in telephone lines [23, 26].

In wireless short distance communication systems (e.g. point-to-point communications), one can also transmit the signal directly without any modulation technique. Some researchers have succeeded to transmit digital signals (Manchester and NRZ line codes) directly from an antenna at short distance and in a radio anechoic chamber by using a disc-cone antenna (designed and constructed by using aluminum pipes with a large volume of 1m^3), the experimental results showed that wireless baseband transmission is realisable when using antennas with a flat amplitude spectrum and a linear phase characteristic over a given band [27-29].

1.4.1 Desirable properties for line codes

Several concepts are needed to help choosing the right line codes [20-29]:

- **Direct-current (DC components):** when the voltage level remains constant for long periods of time, there is an increase of power in the low frequencies of the signal (blocked by some electric devices such as transformers). Most channels are band pass and may not support the low frequencies. Most line codes eliminate the DC-component (they are called: DC-balanced, zero-DC, DC-free, zero-bias, DC equalized). Example: a telephone line cannot pass frequencies below 200 Hz.
- **Transparency:** The performance of the line code should be independent of data, i.e. long string of binary 1's or 0's should not affect the performance.
- **Self-Synchronization:** The clocks at the sender and receiver must have the same bit interval. If the receiver clock is faster or slower it will misinterpret the incoming bit stream.
- **Clock Recovery:** For the line stream to be decoded correctly into the bit stream, the analog signal received must be sampled to a digital signal at constant time intervals. Some types of line codes carry clocks and data at the same time. In other words, the clock is recovered from the incoming signal.
- **Disparity or Digital Sum Variation (DSV):** When there is no DC-component (the average transmitted signal is zero).
- **Baseline wandering (dc wander):** A long string of 0s or 1s can cause a drift in the baseline (baseline: average that receiver calculates from a running average of the received signal power) and make it difficult for the receiver to decode correctly. A good line coding scheme needs to prevent baseline wandering.
- **Data Rate & signal Rate:** The data rate (bit rate) defines the number of data elements (bits) sent in one second; the unit is bits per second (bps). The signal rate is the number of signal elements sent in one second, the unit is baud rate (they are called: signal rate, pulse rate, modulation rate, symbol rate).
- **Transmission power and bandwidth efficiency:** The transmitted power should be as small as possible, and the transmission bandwidth need to be sufficiently small compared to the channel bandwidth so that inter-symbol interference (ISI) will not be a problem.
Generally, digital data is represented by electrical pulse, communication channel is always band limited. Such a channel disperses or spreads a pulse carrying digitized samples passing through it. When the channel bandwidth is greater than the bandwidth of pulse, spreading of pulse is low. But when the channel bandwidth is close to the signal bandwidth, i.e. if we transmit digital data which demands more bandwidth than the channel bandwidth, spreading will occur and cause signal pulses to overlap. This overlapping is called Inter Symbol Interference.
- **Error detection and correction capability:** The line code should have error detection capability, and preferably have error correction capability.
- **Cost and complexity:** higher signal rate lead to higher costs, some code require modulation rate higher than bit rate.

1.4.2 Line Codes used to transmit digital baseband signals

The line coding is the process of converting digital data into a digital signal. There are three basic types of line coding techniques: unipolar, polar and bipolar. All these techniques are with respect to non-return-to-zero and return-to-zero methods. The line coding schemes are categorized as shown in Figure 1.8 [22]. Comparison between several types of line codes is presented in Table 1.1.

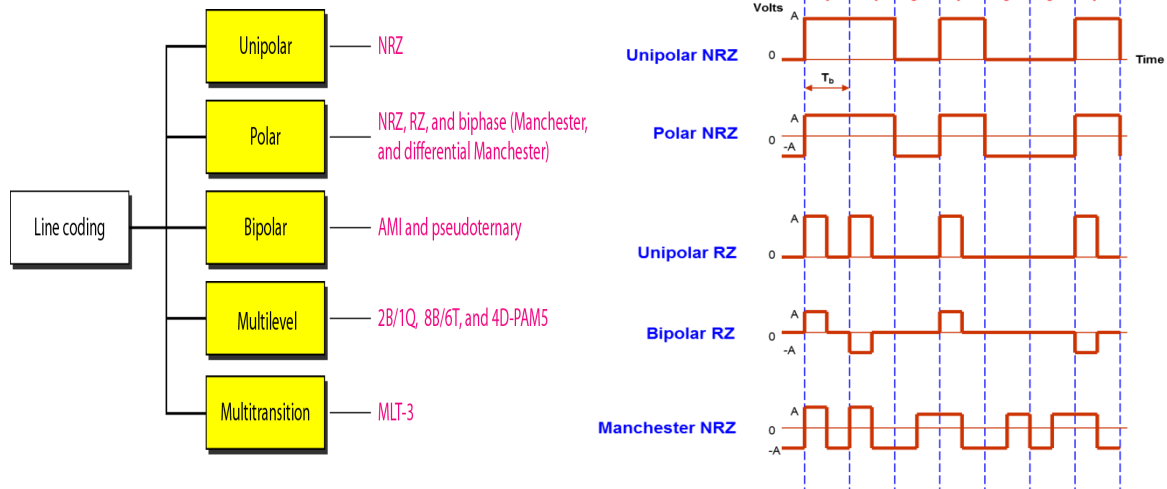


Figure 1.8 Line codes schemes (left). An arbitrary bit pattern in various binary line codes formats (right).

Table 1.1 a Comparison between several types of line codes.

Line codes	Dc component	BW	Clock-recovery	Error-detection	Synch.	Signal- droop// Error- correction	Application, remark
Unipolar NRZ	Yes	bps	Poor	No	No	Yes (low freq.) // No	magnetic Tapes
Unipolar RZ	Yes	2bps	Poor	No	No	Yes // No	Baseband, tape recording
Polar NRZ	No	bps	Poor	No	No	Yes // No	not transparent
Polar RZ	Yes	2bps	Good	Yes	Yes	No // Yes	AMI, telephone system
Bipolar NRZ	No	bps/2	Poor	Yes	No	No // Yes	RS421,422,485 in COM port of Personal computers
Bipolar RZ	No	bps/2	Best	Yes	No	No // Yes	not transparent
Manchester & diff. Manchester	No	2bps	Good	Yes	Yes	No // Yes	Ethernet (IEEE802.3), Token Ring 4Mbps,16Mbps(IEEE802.5)

1.4.3 Choice of Wireless Baseband Transmission encodings

From the analysis of advantages and disadvantages of all the types of line codes above (Table 1.1), the Manchester and Polar RZ line codes were chosen for our application for several reasons:

- There is no DC-component with the Manchester and no DC-component with the Polar RZ if the number of ones in the digital input signal equals the number of zeros.
- Both codes have self-synchronization, clock-recovery and error-detection.
- There is no dc-wander or droops and they are transparent with easy design.

In order to understand how the strength of a signal is distributed in the frequency domain, relatively to the strengths of other ambient signals, Power Spectral Density (PSD) is a measure of a signal's power in the frequency domain. In practice, the PSD is computed from the FFT spectrum of a signal or by computing autocorrelation function and then transforming it. The PSD provides a useful way to characterize the amplitude versus frequency content of a random signal. The unit of PSD is energy per frequency (width).

1.4.3.1 Power Spectral Density (PSD) of line codes

The Power Spectral Density (PSD) shows the strength of the energy variations as a function of frequency. In other words, it shows at which frequencies variations are strong and at which frequencies variations are weak. The unit of PSD is energy per frequency (width) one can obtain energy within a specific frequency range by integrating PSD within that frequency range.

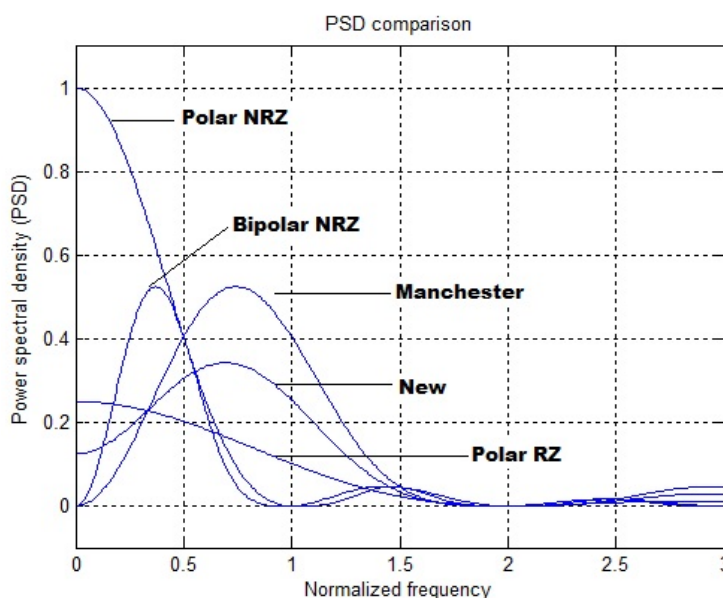


Figure 1.9 Spectral distributions of several types of line codes. There is no dc-component with Manchester and Bipolar NRZ while Polar RZ and NRZ exhibit a dc-component. <http://article.sapub.org/10.5923.j.jinc.20160605.02.html>.

Computation of the PSD of a signal is done directly by Fast Fourier Transform (FFT) or by computing the autocorrelation function and then transforming it by FFT. Figure 1.9 shows the Power Spectrum Density (PSD) of several types of signal line codes.

To study the performance of a line code, we need to consider its PSD. The reason for not being able to use the Fourier transform to find the spectrum of a line code is that the information signals that generate a line code is a stochastic (non-deterministic) signal, and the Fourier transform cannot be applied for non-deterministic signals.

As it is known, pulses have spectra of the form of Sinc functions. So in theory, channels with infinite bandwidths are required to transmit any of the line codes discussed previously. To study spectra of stochastic signals, we use the PSD, which shows the distribution of signal power versus frequency [23-26].

Each line code is described by a symbol mapping function a_k and a pulse shape $p(t)$. Symbol mapping function (a_k) are unipolar, polar, bipolar. The pulse shapes $p(t)$ are NRZ, RZ, and Manchester.

❖ **PSD of Polar RZ encoding**

For Polar RZ line code, a_k is:

for 1's

$$a_k = \begin{cases} +A & 0 \leq t \leq T_b/2 \\ 0 & T_b/2 \leq t \leq T_b \end{cases}$$

for 0's

$$a_k = \begin{cases} -A & 0 \leq t \leq T_b/2 \\ 0 & T_b/2 \leq t \leq T_b \end{cases}$$

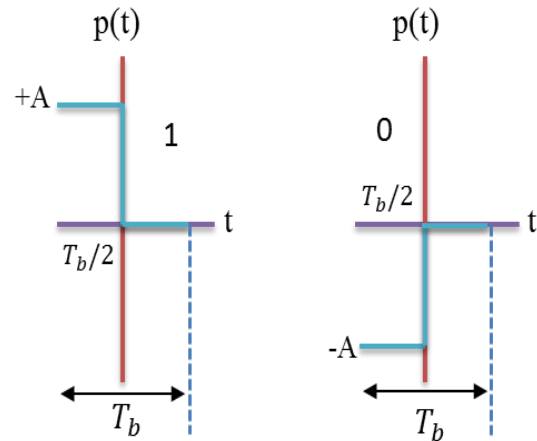


Figure 1.10 Pulse shapes of “1 “and “0 “for Polar RZ line code.

where T_b is the bit duration and A is the amplitude of the pulse.

The power spectrum density of the line code is:

$$G(f) = |P(f)|^2 S(f) \tag{1.1}$$

where $P(f)$ is the PSD of the basic pulse shape $P(t)$ and $S(f)$ is the power spectral density of the digital sequence (a_k). Then, the PSD equation for the polar RZ is (more details on the PSD of Polar RZ are given in appendix A):

$$G(f) = \frac{A^2 T_b}{4} \text{sinc}^2(f T_b / 2) \quad (1.2)$$

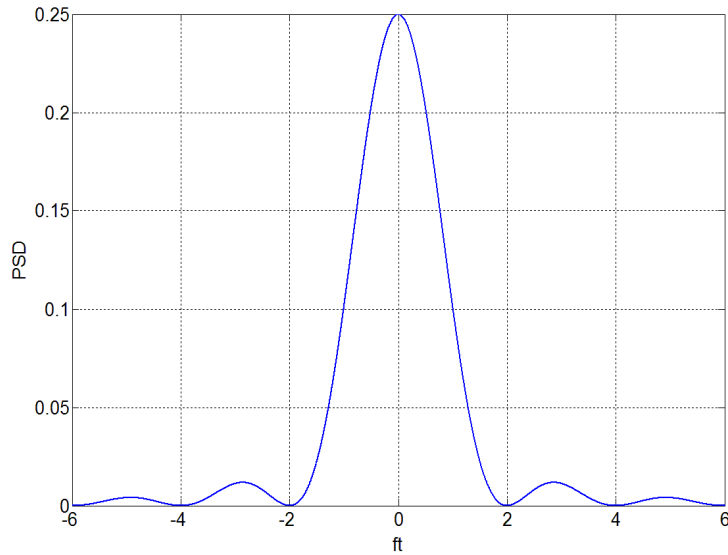


Figure 1.11 Power spectrum density versus normalized frequency for the Polar RZ line code where t is the duration of bit. PSD value is different from 0 at dc frequency (there is a dc-component).

❖ PSD of Manchester encoding

For the Manchester line code, a_k is:

$$\text{for } 1\text{'s} \quad a_k = \begin{cases} +A & 0 \leq t \leq T_b/2 \\ -A & T_b/2 \leq t \leq T_b \end{cases}$$

$$\text{for } 0\text{'s} \quad a_k = \begin{cases} -A & 0 \leq t \leq T_b/2 \\ +A & T_b/2 \leq t \leq T_b \end{cases}$$

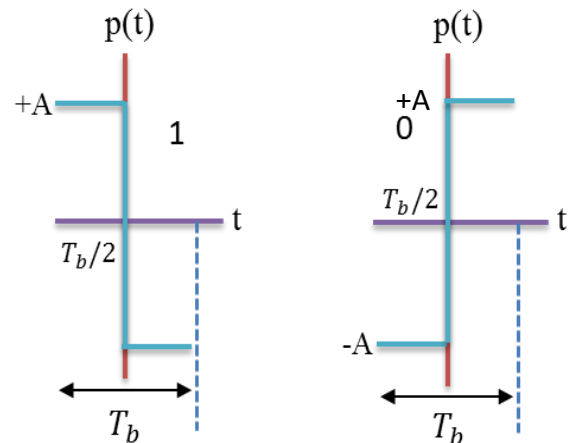


Figure 1.12 Pulse shapes of "1" and "0" for Manchester line code.

Manchester code refers to the combination of a Manchester pulse with polar mapping. Then, the impulse response of Manchester line code is:

$$p(t) = \Pi\left(\frac{t + T_b/4}{T_b/2}\right) - \Pi\left(\frac{t - T_b/4}{T_b/2}\right) \quad (1.3)$$

where Π is the rectangular function.

Following the same procedure (see appendix A):

$$G(f) = A^2 T_b \text{sinc}^2\left(\frac{f T_b}{2}\right) \sin^2\left(\frac{\pi f T_b}{2}\right) \quad (1.4)$$

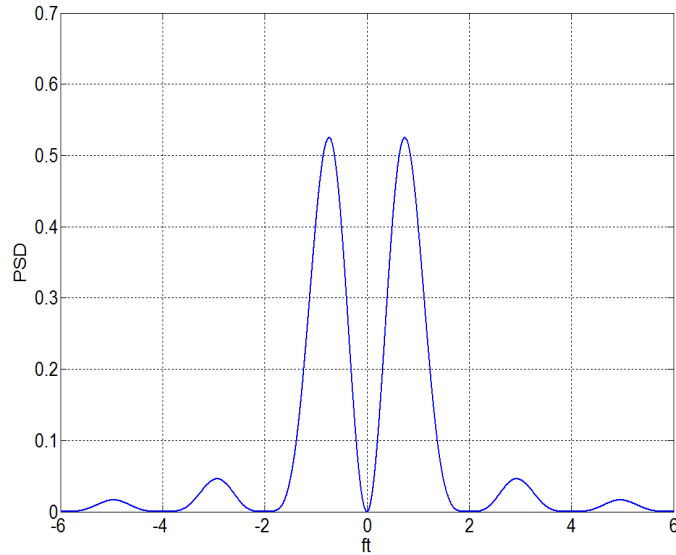


Figure 1.13 Power spectrum density versus normalized frequency for the Manchester line code where t is the duration of bit. There is no dc-component.

1.4.4 Simulation of Manchester and Polar RZ encoded signals

The simulation of Polar RZ and Manchester line codes were achieved with MATLAB 2013a software. Fast Fourier Transform (FFT) is applied on the signal to obtain its frequency representation.

The digital data signal in time domain and the spectrum in frequency domain of Manchester and Polar RZ encodings at 1Gbps are presented in the next section. In the frequency domain, there is clearly some power at zero frequency (dc-component) with Polar RZ encoding while there is no power at zero frequency with Manchester encoding.

1.4.4.1 Manchester encoding

The Manchester encoding was developed by Manchester University in 1998 (also known as bi-phase encoding). The bit '0' is a low-to-high transition, while the bit '1' is a high-to-low transition. The duration of the bit is divided into two halves. The voltage is at one level during the first half and moves to the other level during the second half. Manchester is used in 10-Mbps Ethernet LAN (IEEE 802.3). Differential Manchester is used in Token Ring LAN at 4Mbps & 16Mbps (IEEE 802.5), STP cable [19]. The spectrum of Manchester line code at a data rate of 1Gbps with 20 bits code pattern [101100101101011001] is presented in figure 1.14.

Advantages: there is no DC- component (always a balanced 0 and 1 levels usage); easy to synchronize (self-clocking codes); does not suffer from signal droop (suitable for transmission over AC couple lines); is transparent.

Disadvantages: large bandwidth (twice the bit rate, because of the larger number of transitions it occupies a significantly large bandwidth) and does not have error detection capability [22].

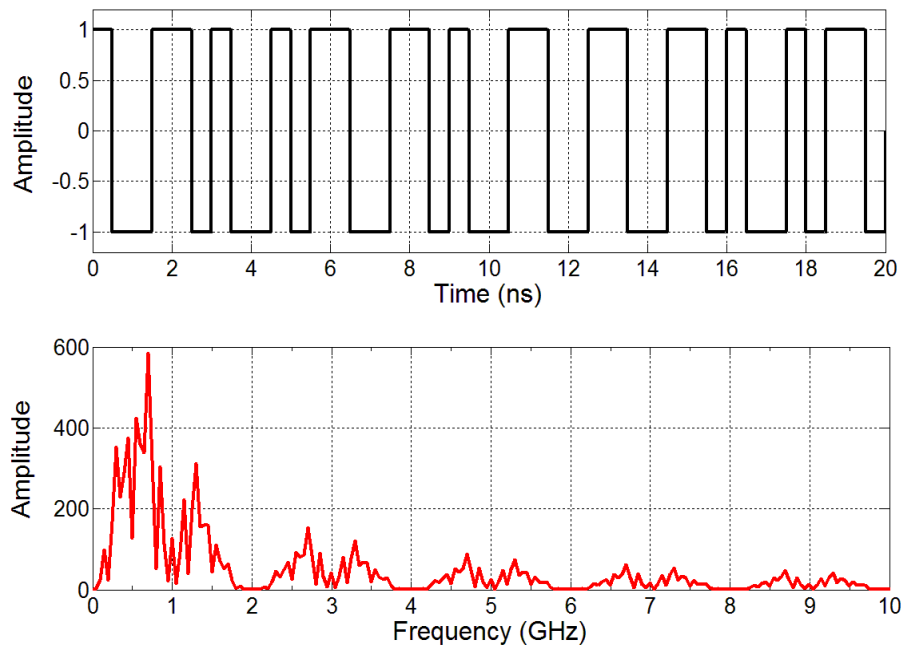


Figure 1.14 Manchester encoded signal at 1Gbps data rate with random data input (20 bits code pattern). The data input is [101100101101011001] (top). Fast Fourier Transform of Manchester (bottom). There is no dc-component.

1.4.4.2 Polar RZ encoding

For a signal bit duration, the information is contained in the first half of the bit interval, while the second half is always at level “zero”. An example of a Polar RZ waveform is shown in figure 1.15 (Top).

Advantages: easy to engineer; self-clocking; use as symbol timing clock.

Disadvantages: DC-component; does not have any error correction capability; not transparent; occupies twice as much bandwidth as polar Non-Return to Zero (NRZ); no DC-component of polar RZ line code if number of zeros is equal to number of ones (see figure 1.16).

The simulation of Polar RZ line code at a data rate of 1Gbps with 20 bits code pattern [101100101101011001] is presented in figure 1.15. Clearly, there is power at zero frequency (dc-component).

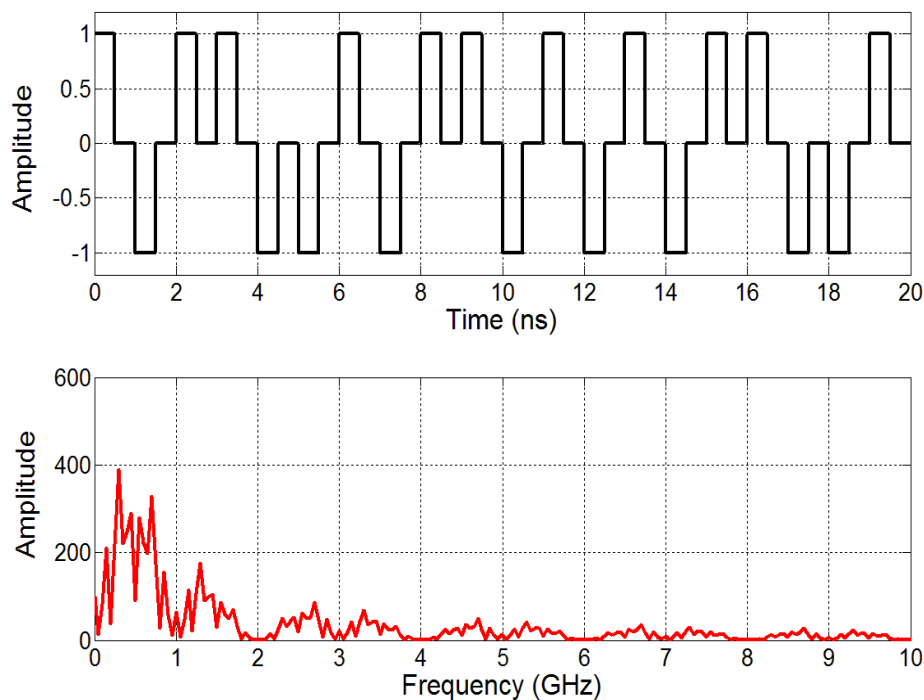


Figure 1.15 Polar RZ encoded signal at high data rate of 1Gbps with random data input (20 bits code pattern). The data input is [101100101101011001] (top). Fast Fourier Transform of Polar RZ (bottom). There is a dc-component.

It is possible to prevent the generation of lower frequency components when successive identical codes, such as ‘111111’ or ‘000000’ or ‘10101010’ or ‘01010101’ are transmitted, as when number of zeros is equal to number of ones in the data input sequence.

Figure 1.16 shows a random digital data input at 1Gbps and the spectrum of Polar RZ line codes with the same number of ones and zeros. As can be seen there is no power at zero frequency (no dc-component).

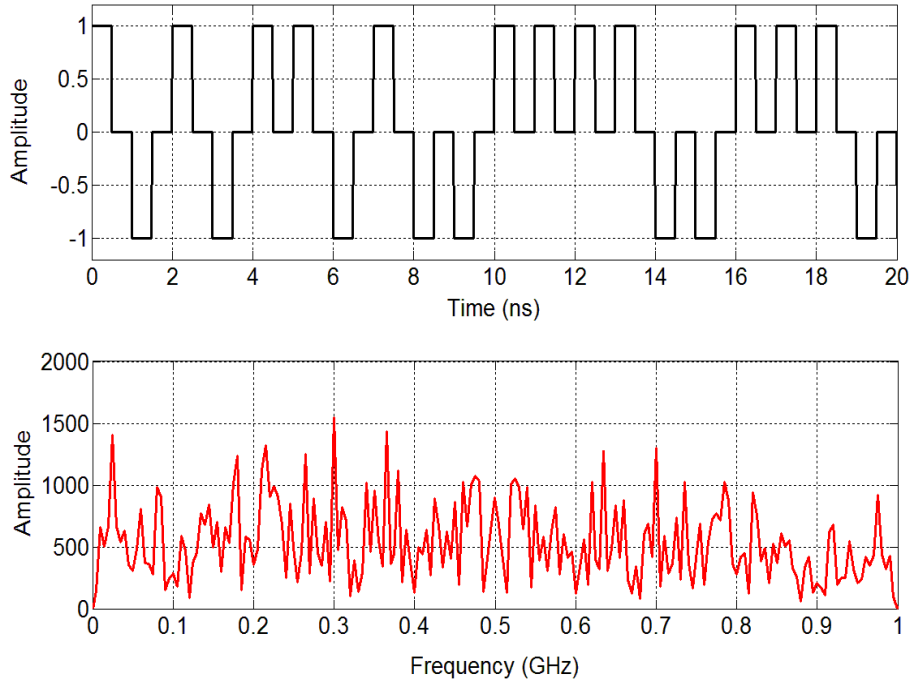


Figure 1.16 Polar RZ line code signal at a data rate of 1Gbps with random data input. Number of zeros is equal to number of ones at data input sequence. There is no a dc-component.

1.5 Organization of thesis

This thesis deals with the study of wireless baseband transmission of Manchester and Polar RZ encoded signals directly through a set of antennas. The emitting and receiving antennas are placed at short distance from each other and data rate has been chosen equal to 1Gbps at least. Two BER techniques of calculation are proposed in order to improve the performance of WBT system. The details of these techniques are presented in the next chapter.

The feasibility of study of the wireless baseband transmission system depends on the number of samples for each bit code pattern. The simulations and measurements to transmit and receive the digital data directly from an antenna at a data rate on a short distance are treated in different chapters.

In **Chapter 2**, the simulations of the transmission of digital input data directly from an antenna with two different approaches are done. First, the first harmonic of the signal in frequency domain is used, since the first harmonic spectrum of line code contains between 80% to 90% of the power of the original digital data. Based on this idea, the first harmonic range of Polar RZ and Manchester encoding at 1Gbps is from 0GHz to 2GHz ($f_L=0$ and $f_H=2GHz$).

In order to estimate the quality of the transmission of the digital signal at the output, the BER has been calculated. Two different ways are considered to calculate the BER of the digital output signal. The first one is based on using the average value of samples, and the second one is based on using the position of a specific sample.

It is required to use a large size antenna in order to reach the bandwidth range. Because of this problem, secondly, we have selected another approach by using harmonics of the signal. The WBT has been simulated using the same antenna transfer function. In this chapter, it is shown that using a small size antenna to transmit and receive the encoded signal directly without modulation technique, one can meet the wireless baseband transmission requirement for our applications.

In **Chapter 3**, a compact size planar printed Antipodal Vivaldi and a monopole antenna have been designed and fabricated to demonstrate the effectiveness of the antennas design. A shifted ground plane edge and an etched or tapered slot on the ground plane are the performed improvements in the proposed antennas of dimensions of $37*21*1.6 \text{ mm}^3$.

Based on this approach, the lower-frequency $S_{11} \leq -10 \text{ dB}$ limitation of the designed antenna is lowered to 3.6 GHz from the original 4.3 GHz. By comparing the two different structures of AVA, one can conclude that the measured gain of 6.56 dBi at 8.5 GHz obtained with an etched Taper Slot Edge (TSE) structure is better than the measured gain of the AVA with an etched slot for which the measured gain was 3.47 dBi at 8.5 GHz.

For the monopole antenna of dimensions $18*12*1.6 \text{ mm}^3$, the measured bandwidth is from 3.1 to 11.3 GHz. Within the operating frequency band, the measured gain is better than 6.21 dBi. According to the measured characteristics, the three smaller size proposed antennas can be better candidates for UWB radio frequency applications.

In **Chapter 4**, experimental work has been done for the wireless baseband transmission system. A good match is observed between experimental and simulation results. Wireless baseband transmission for Polar RZ and Manchester encodings at a data rate of 1Gbps and 2Gbps have been achieved at short distance. Using this approach, we have been able to successfully transmit digital data directly with two AVA and two monopole antennas at short distance without modulation technique.

In order to verify WBT with large antennas, a horn antenna has been proposed to overcome the bandwidth range from 2 up to 32 GHz. Based on the same procedure used with AVA, WBT can be achieved when using horn antennas. BER measurements have been obtained when the distance between horns reached more than 200 cm for Polar RZ and more than 210 cm for Manchester with a 20-bit code pattern. WBT have been achieved for 20, 500, and 1000-bit code patterns and when the number of sample per bit is 4, 6, and 12 samples.

In **Chapter 5**, the results of this thesis are summarized and the perspectives of the possible future works are presented.

Bibliography

- [1] K. K. Likharev and V. K. Semenov, "RSFQ logic/memory family: A new Josephson junction technology for sub-terahertz clock frequency digital systems," *IEEE Trans. Appl. Super.*, vol. 1, no. 1, pp. 3–27, 1991.
- [2] A. Fujimaki, M. Tanaka, T. Yamada, Y. Yamanashi, H. Park and N. Yoshikawa, "Bit-serial Single Flux Quantum microprocessor CORE," *IEICE Trans. Electron.*, vol. E91-C, pp. 342-349, 2008.
- [3] D. Bouis and P. Febvre, "Antennas for Short Distance Communications in Cryogenic Environment," *Int. J. Inf. and Millimeter Waves*, vol. 29, no. 12, pp. 1156-1162, December 2008.
- [4] P. Febvre, S. Badi "Superconductive microwave single-flux-quantum digital circuits and corresponding opto-electronic interfaces: on-going studies and first experimental results," IMEP-LAHC – University of Savoie –73376 Le Bourget du Lac Cedex – France, 13 July 2005.
- [5] S. Badi "Interfaces optoélectroniques ultra-rapides pour l'électronique supraconductrice à quantum de flux magnétique," Thèse présentée à l'Université de Savoie, Mars 2009.
- [6] J. F. Bulzacchelli "A superconducting band pass delta-sigma modulator for direct ADC of microwave radio", PhD thesis, Massachusetts Institute of Technology, June 2003.
- [7] Ya. S. Greenberg, "Application of superconducting quantum interference devices to nuclear magnetic resonance," *Novosibirsk State Technical University*, 630092 Novosibirsk 92, Russia, *Reviews of Modern Physics*. vol. 70, no. 1, January 1998.
- [8] V. K. Semenov, "Digital SQUIDS: New Definitions and Results," *IEEE Transactions on Applied Superconductivity*, vol. 13, no. 2, June. 2003.
- [9] M. Klauda, T. Kässer, B. Mayer, and others," *Superconductors and Cryogenics for Future Communication Systems* , " *IEEE Transactions on Microwave Theory and Techniques*, vol. 48, no. 7, July 2000.
- [10] A. Kirichenko, D. Gupta, and S. Sarwana," *RSFQ Asynchronous Switch Matrix*," *IEEE Transactions on Applied Superconductivity*, vol. 17, no.2, June. 2007.
- [11] O. A. Mukhanov, P. D. Bradley, and others," *Design and Operation of RSFQ Circuits for Digital Signal Processing*," 5th International superconductivity electronics conference (ISEC '95), Nagoya, Japan, 18-21 September 1995.
- [12] T. Reich, T. Ortlepp, and F. H. Uhlmann," *Analysis of a Digital SQUID Magnetometer Utilizing a Direct Coupled DC SQUID for Improved Magnetic Field Resolution*," *IEEE Transactions on Applied Superconductivity*, vol. 17, no. 2, June 2007.

- [13] T. Reich, T. Ortlepp, F. H. Uhlmann, "Development of a digital SQUID device for high sensitive measurement of widely varying magnetic fields," Internationales Wissenschaftliches Kolloquium Technische University at Ilmenau, 11-15 September, 2006.
- [14] T. Reich, P. Febvre, et al., "Experimental study of a hybrid single flux quantum digital superconducting quantum interference device magnetometer," Journal of applied Physics 104, 024509, 2008.
- [15] N. Fujimaki, H. Tamura, T. Imamura, and S. Hasuo, "A single-chip SQUID magnetometer," IEEE Transactions Electron Devices, vol. 35, pp. 2412-2418, Dec. 1988.
- [16] U. Fath, R. Hundhausen, T. Fregin, P. Gerigk, W. Eschner, A. Schindler, and F. H. Uhlmann, "Experimental digital SQUID with integrated feedback circuit," IEEE Transaction on Applied Superconductivity, vol. 7, pp. 2747-2751, Jun. 1997.
- [17] G.R. Aiello, and G. D. Rogerson, "Ultra-Wideband Wireless Systems," IEEE Microwave Magazine, vol.4, no.2, pp.36-47, June 2003.
- [18] M. Z. Win, and R. A. Scholtz, "Impulse Radio: How it works," IEEE Communications Letters, vol.2, pp.36-38, Feb. 1998.
- [19] B. A. Forouzan, "Data communication and network," Book, chapter4, Fourth edition, NDSL, 2008.
- [20] V. S. Latha, "Performance Evaluation of Different Line Codes," Indian Journal of Computer Science and Engineering (IJCSE), ISSN: 0976-5166, vol. 2, no. 4, Aug-Sep 2011.
- [21] A. PhonPhoem, "Encoding Digital Transmission," Computer Engineering Department, Kasetsart University, Bangkok, Thailand, June 2004.
- [22] C. Subrahmanyam, P. K. Babu, "Implementation of Different Code for Baseband Wireless communication System," Dept. of Technical Education A.p., Hyderabad. International journal of Engineering Research & Technology (IJERT) ISSN: 2278-0181 Vol. 1 Issue 7, September- 2012.
- [23] D. C. Dalwadi, B. C. Goradiya, M. Mehfuza, "Performance evaluation of Power Spectral Density of different line coding Technique," B.V.M. Engineering College, V. V. Nagar, Gujarat, India, 13-14 May, 2011.
- [24] B. P. Lathi, ZHI Ding, "Modern Digital and Analog Communication Systems," International Fourth edition, Oxford University Press, chapter 7, 2010. <https://archive.org/details/Analog01>.
- [25] HA H. Nguyen, ED. Shwedyk, "A First Course in Digital Communications," Book, Cambridge University Press, chapter 3, 2009.
- [26] J. L. LoCicero, and B.P. Patel, "Line Coding" Mobile Communications Handbook Ed. Suthan S. Suthersan Boca Raton: CRC Press LLC, 1999.

- [27] J. Kitagawa, T. Taniguchi, and Y. Karasawa, "Transmission Characteristics of Wireless Baseband Transmission Under Multipath Environments Using Real-Valued Signal Analysis," the University of Electro-Communications, Chofu, 182-8585 Japan, part 2, vol.90, no.10, 2007.
- [28] J. Kitagawa, "Wireless baseband transmission-proposal and experiments of a new Wireless transmission scheme," Graduate School of Electro-Communications, The University of Electro-Communications, PhD Thesis, Dec. 2006.
- [29] J. Kitagawa, T. Taniguchi, Y. Karasawa, "Wireless Baseband Transmission Experiments," IEICE, Transaction on communication, vol.E89-B, no.6, pp.1815-1824, June 2006.

2 Analysis of Wireless Baseband Transmission for transmission of RSFQ digital signals

2.1 Introduction

Future networks need to provide data rates up to tens of gigabit per second in order to satisfy new applications requiring for high data rates. There are two schemes used in transmission systems. One is carrier transmission and the other is baseband transmission. Wireless transmissions adopt carrier transmission systems almost exclusively, although both baseband and carrier transmission systems are used in wired transmissions. Conventional wireless transmission systems, i.e., carrier transmission systems, modulate a carrier with a baseband signal carrying the message for transmission through a communication channel including antennas.

A typical carrier is a sinusoidal electromagnetic wave. There are two main reasons for the modulation. First, baseband signals could not be radiated efficiently from antennas because they have low-frequency components. Second, it is possible to use Frequency Division Multiplexing (FDM) schemes which shift the signal spectrum. A baseband transmission scheme for wireless communications is fundamentally different from conventional wireless transmission schemes. When the case of wireless baseband transmission (WBT) is considered, there is no concept of a carrier wave, and processing with an equivalent baseband system is not possible. Because baseband data signals are radiated directly, an extremely wide bandwidth is occupied. Ultra-wide band (UWB) radio systems usually employ short pulses, typically of the order of sub-nanoseconds. These pulses have an extremely broad bandwidth, larger than 500MHz.

The origin of UWB technologies began with time-domain electromagnetics in the 1960's [1-3]. The transfer function characterization of a printed UWB antenna provides information that can be used for better UWB transmission. Communication system designs are presented in this chapter, and their characterization to transmit and receive wireless baseband signals is done using frequency domain simulations. In digital transmission, Bit Error Rate (BER) is a key parameter that is used to assess systems that transmit digital data. Systems for which the BER is applicable include radio data links as well as fiber optical data systems, Ethernet, or any system that transmits data over a network where noise, interference, and phase jitter may cause significant degradation of the digital signal. Characterization of WBT for high data rate communications is under the scope of this chapter. MATLAB codes have been developed for simulating WBT and BER in frequency domain and time domain respectively. Tests and validation of the proposed methods are also parts of the work presented in this chapter.

2.2 Wireless Baseband Transmission concept

As pointed out in the previous chapter, binary digits (or bit) “0” and “1” are used to represent information content. In baseband data transmission, the bits are mapped into two voltage levels for direct transmission without any frequency translation. Such a baseband data transmission is applicable to cable systems since the transmission bandwidth of most cable systems is in the baseband.

The wireless baseband transmission radiates a baseband data sequence directly from an antenna without the need for modulation techniques [3-10].

A schematic diagram of wireless baseband transmission is shown in figure 2.1 (b). Therefore, the use of WBT systems eliminates the need for local oscillator circuits and mixers in conventional wireless systems as shown in figure 2.1 (a) and the construction is to be simpler. Wide-band wireless communications such as UWB and IR have attracted a lot of attentions. When the data rate of transmission becomes higher than a certain level, the data signal itself could be directly transmitted from an antenna without analogue modulation techniques, this is due to the fact that it contains sufficient high frequency components to be propagated through the air.

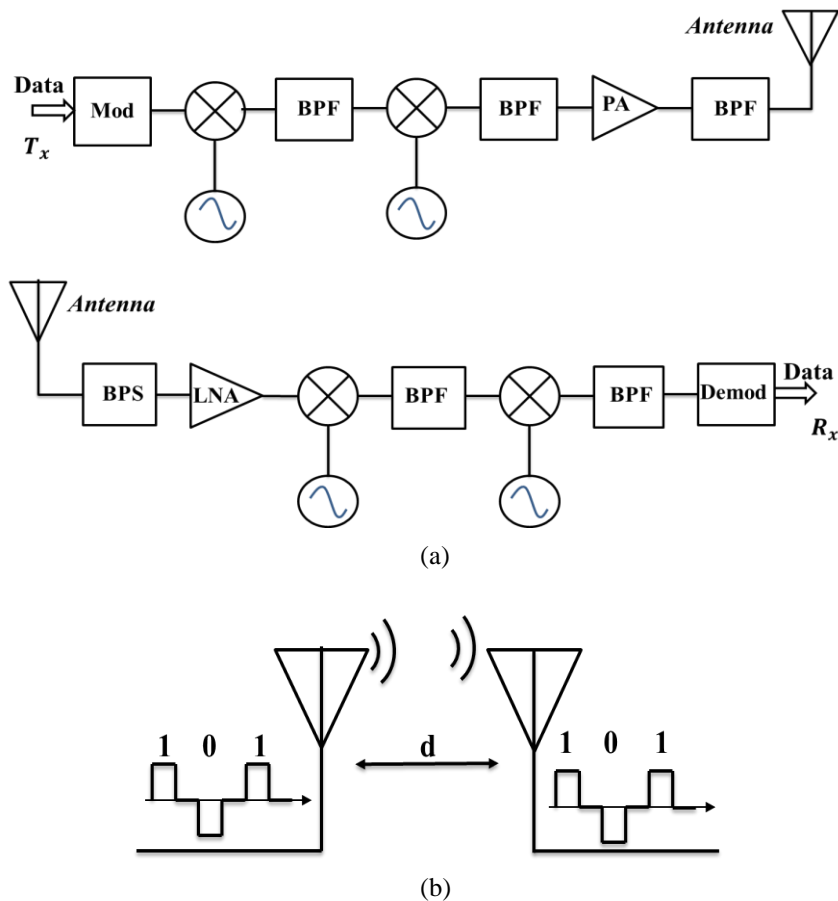


Figure 2.1 Transceiver architecture. Mod (modulator), BPF (band-pass filter), PA (power amplifier), LAN (low-noise amplifier), and Demod (demodulator). (a) Conventional wireless system. (b) Wireless baseband transmission system.

2.3 Transfer functions of UWB transmission antenna system

Since the 1970's, the Federal Communications Commission (FCC) permitted the commercial deployment of Ultra-Wideband communication systems in the 3.1 GHz to 10.6 GHz band, which has been widely investigated and developed for wireless communications applications, that is within a bandwidth of 7.5 GHz. The UWB systems allow to span the entire spectra and to use this band like an industrial, scientific, and medical band. It allows to transmit and receive short pulses without carrier or modulated short pulses with carriers. UWB-based systems can transmit extremely narrow pulses on the order of 1ns, where the impulse response of the antenna is of particular interest because it has the ability to alter or shape the transmitted or received pulses.

UWB antennas act as pulse-shaping filters and have an important impact on the transceiver design complexities. UWB antennas are invariant linear time systems defined by a transfer function in the frequency domain and their associated impulse response in time domain [11-14].

In low frequency systems, Kirchhoff's laws are suitable for analysis of a circuit schematic. Transfer functions provides important features such as gain, stability region, filtering properties, and time-domain output information. On the contrary, at high frequencies (microwave and higher) Kirchhoff's laws are not suitable, and instead we must use the transmission line theory. The Scattering (S) Matrix parameters play a key role at higher frequencies to estimate system's gain, return loss, voltage standing wave ratio (VSWR), and reflection coefficients. S-parameters H (system transfer function) have a causal relationship. S_{11} is nearly the inverse of H which can be derived in a lossless network using the lossless network properties of S-Matrices. We can then use the reciprocity and symmetry properties of S-Matrices such as $|S_{22}| = |S_{11}|$ and $|S_{21}| = |S_{12}|$ where S_{22}, S_{11}, S_{21} , and S_{12} may have different phase properties.

When transmitting over an instantaneous bandwidth of several giga-hertz as it is possible in UWB systems, traditional approaches to antenna characterization prove insufficient for system design and characterization. A solution to this difficulty is to employ transfer function methods for characterizing antennas. Several authors have proposed transfer function definitions to associate with antennas. Two different approaches for defining antenna transfer functions are presented in [11] and [12]. In [11], the authors presented a method to characterize UWB antenna systems using transfer functions described by $ABCD$ parameters and S-parameters when the antenna system is considered as a two-port network. Another approach for modeling UWB antennas was also presented in [14], the determination of directional impulse responses uses singularity expansion method. For more publications interested readers are referred to [15-20]. One can find different expressions of the transfer functions, coming from different definitions.

2.3.1 Definition of transfer functions

In principle, the antenna transfer function can be determined in the frequency or time domain as was shown in [11-21]. Typically, narrow-band antennas and propagation are described in the frequency domain. Usually the characteristic parameters are assumed to be constant over a few percent bandwidths. For UWB systems, the frequency-dependent characteristic of the antennas and the frequency-dependent behavior of the channel have to be considered. Therefore, UWB systems are often

realized in an impulse-based technology and the time domain effects and properties have to be known as well.

The system transfer function $H(\omega, \theta, \varphi, R)$ is a crucial parameter to obtain the impulse response affected by the communication. It can be defined as the ratio between the voltage received at the receiver antenna terminal and the voltage at the input of the transmitter antenna. It has been explained in [11-20] that UWB impulse radio transmission can be formulated using the extension of Friis Transmission Formula [21]. In one word, if $H_{TA}(\omega, \theta, \varphi)$ is the transfer function of the transmitter antenna, $H_{RA}(\omega, \theta, \varphi)$ is the transfer function of the receiver antenna, and $H_{ch}(\omega, R)$ is the free space transfer function, then equation (2.1) represents the system transfer function:

$$H(\omega, \theta, \varphi, R) = H_{TA}(\omega, \theta, \varphi) \cdot H_{RA}(\omega, \theta, \varphi) \cdot H_{ch}(\omega, R) \quad (2.1)$$

where $\omega = 2\pi f$, f is the operating frequency, (θ, φ) the orientation, and R the distance between the transmitting and receiving antennas.

Transfer functions based on voltage ratio definition are described by $ABCD$ parameters and S-parameters when the antenna system is considered as a two-port network. Consider a transmitting-receiving antenna system as shown in figure 2.2, two identical antennas point towards each other with a distance R , the system transfer function is the voltage ratio V_{out}/V_{in} , according to microwave network theory [22], $ABCD$ parameters describe the relationships of the input and output voltage and current. Therefore, the transfer function of antenna system, which is defined by a voltage ratio, can be easily described by the $ABCD$ parameters. Because, the S-parameters can be measured with a Vector Network Analyzer (VNA) at very high accuracy, while the $ABCD$ parameters cannot be obtained easily with high accuracy because it is difficult to measure the voltage and current at microwave frequencies, the antenna system transfer function is derived from $ABCD$ parameters and then converted to equivalent S-parameters [23]. Also, the measured S-parameters can be converted back into the $ABCD$ matrix. The $ABCD$ parameters and S-parameters are presented in figure 2.3.

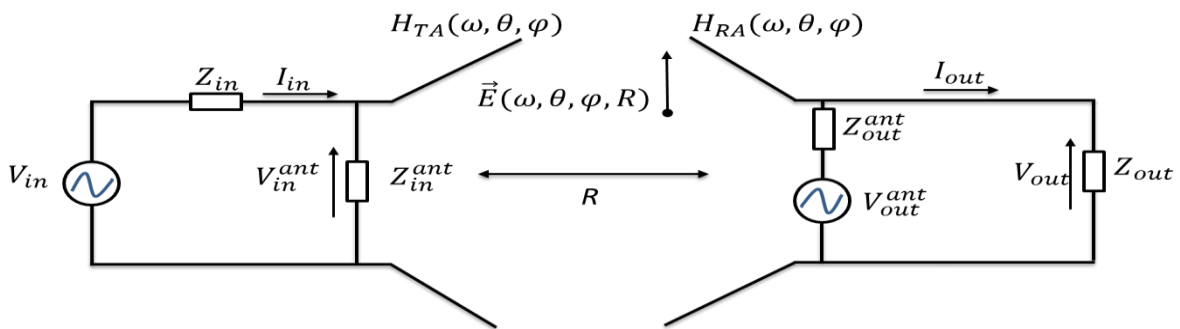


Figure 2.2 Transmitting-receiving antennas system model.

In this work, two different approaches are considered to characterize the transfer function of the set of the two antennas. The first approach is based on using a source generator (an Arbitrary Waveform Generator (AWG)) as a voltage signal (V_{in}), and on a sampling oscilloscope at the output. The second

approach is based on characterizing the transfer function by estimating the contribution of each antenna and of the channel of communication.

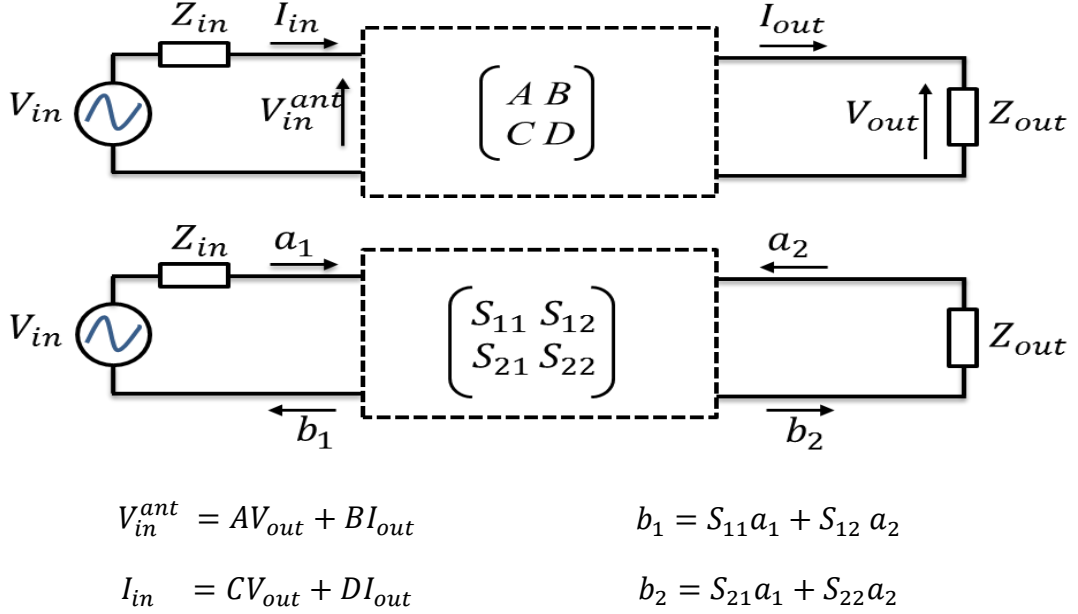


Figure 2.3 ABCD parameters and S-parameters of the antenna system.

2.3.1.1 Approach based on electrical model

The first step to derive a relationship between transfer functions and S-Matrices is to describe a two-port network in terms of impedances, voltages and power-waves. Figure 2.3 shows a basic representation of what S_{11} , S_{22} , S_{21} , and S_{12} are in terms of reflection and transmission of voltage-waves in a circuit. In practice, we send a signal from a source generator (AWG) as a voltage signal (V_{in}) and it is measured at the output with a Digital Storage Oscilloscope (DSO) (V_{out}). The total transfer function in frequency domain is represented as follows:

$$V_{out}/V_{in} = H(\omega, \theta, \varphi, R) \quad (2.2)$$

As illustrated in figure 2.2, the receiving antenna is connected to a receiver which is loaded by impedance. The relationship between the signal at the input of the transmitting antenna and the voltage and current at the output can be written as:

$$V_{in} = Z_{in}I_{in} + V_{in}^{ant} \quad (2.3)$$

$$V_{out} = Z_{out}I_{out} \quad (2.4)$$

In figure 2.3, the set of two antennas can be modeled with an $[ABCD]$ matrix as follows:

$$\begin{bmatrix} V_{in}^{ant} \\ I_{in} \end{bmatrix} = \begin{bmatrix} A & B \\ C & D \end{bmatrix} \cdot \begin{bmatrix} V_{out} \\ I_{out} \end{bmatrix} \quad (2.5)$$

then

$$V_{in}^{ant} = AV_{out} + BI_{out} \quad (2.6)$$

$$I_{in} = CV_{out} + DI_{out} \quad (2.7)$$

Combining (2.4) and (2.6)

$$V_{in}^{ant} = AV_{out} + B \frac{V_{out}}{Z_{out}} = V_{out} \left(A + \frac{B}{Z_{out}} \right) \quad (2.8)$$

and

(2.4) + (2.7):

$$I_{in} = CV_{out} + D \frac{V_{out}}{Z_{out}} = V_{out} \left(C + \frac{D}{Z_{out}} \right) \quad (2.9)$$

Substituting (2.8) and (2.9) in (2.3)

$$V_{in} = Z_{in}I_{in} + V_{in}^{ant} = Z_{in}V_{out} \left(C + \frac{D}{Z_{out}} \right) + V_{out} \left(A + \frac{B}{Z_{out}} \right) \quad (2.10)$$

hence

$$V_{in} = V_{out} \left[Z_{in} \left(C + \frac{D}{Z_{out}} \right) + \left(A + \frac{B}{Z_{out}} \right) \right] \quad (2.11)$$

Since it is easier to measure S-parameters, it is wise to use the expression of the $ABCD$ matrix as a function of S-parameters. Two-port parameter conversion for scattering and voltage-and current-based matrices can be written as [23]:

$$A = \frac{(1 + S_{11})(1 - S_{22}) + S_{12}S_{21}}{2S_{21}} \quad S_{11} = \frac{A + B/Z_0 - CZ_0 - D}{A + B/Z_0 + CZ_0 + D}$$

$$B = Z_0 \frac{(1 + S_{11})(1 + S_{22}) - S_{12}S_{21}}{2S_{21}}$$

$$S_{12} = \frac{2(AD - BC)}{A + B/Z_0 + CZ_0 + D}$$

$$C = \frac{1}{Z_0} \frac{(1 - S_{11})(1 - S_{22}) - S_{12}S_{21}}{2S_{21}}$$

$$S_{21} = \frac{2}{A + B/Z_0 + CZ_0 + D}$$

$$D = \frac{(1 - S_{11})(1 + S_{22}) + S_{12}S_{21}}{2S_{21}}$$

$$S_{22} = \frac{-A + B/Z_0 - CZ_0 + D}{A + B/Z_0 + CZ_0 + D}$$

Based on the definition of ABCD parameters and S-parameters above, equation 2.11 can be rewritten as:

$$V_{in} = V_{out} \left[Z_{in} \left(\frac{\frac{1}{Z_0} ((1 - S_{11})(1 - S_{22}) - S_{12}S_{21}) + \frac{1}{Z_{out}} ((1 - S_{11})(1 + S_{22}) + S_{12}S_{21})}{2S_{21}} \right) + \left(A + \frac{B}{Z_{out}} \right) \right] \quad (2.12)$$

Here, we assume that the two antennas are identical and that their impedance seen from connector port is $Z_0 = Z_{out} = Z_{in}$. The following relations are achieved:

$$V_{in} = V_{out} \left[\frac{(1 - S_{11})(1 - S_{22}) - S_{12}S_{21} + (1 - S_{11})(1 + S_{22}) + S_{12}S_{21}}{2S_{21}} + \left(A + \frac{B}{Z_0} \right) \right] \quad (2.13)$$

$$V_{in} = V_{out} \left[\frac{(1 - S_{11})[1 - S_{22} + 1 + S_{22}]}{2S_{21}} + \left(A + \frac{B}{Z_0} \right) \right] = V_{out} \left[\frac{(1 - S_{11})}{S_{21}} + \left(A + \frac{B}{Z_0} \right) \right] \quad (2.14)$$

where

$$A + \frac{B}{Z_0} = \frac{1}{2S_{21}} [(1 + S_{11})(1 - S_{22}) + S_{12}S_{21} + (1 + S_{11})(1 + S_{22}) - S_{12}S_{21}] = \frac{1 + S_{11}}{S_{21}}$$

and

$$V_{in} = V_{out} \left[\frac{1 - S_{11}}{S_{21}} + \frac{1 + S_{11}}{S_{21}} \right] = V_{out} * \frac{2}{S_{21}} \quad (2.15)$$

then

$$\frac{V_{out}}{V_{in}} = H(\omega, \theta, \varphi, R) = \frac{S_{21}}{2} \quad (2.16)$$

Observing (2.16), this expression can be used to simulate the performance of the antenna system for the transmission of any signal, provided that S_{21} is known for each frequency. This expression is general and valid in near-field as well.

2.3.1.2 Approach based on transmitter and receiver transfer function

The second approach to characterize the transfer function consists of estimating the contribution of each antenna and of the channel of communication. We consider the case of the transmitting-receiving antenna system shown in figure 2.2 by following the formalism used in [14, 11]. The transmitting antenna transfer function is defined as the ratio of the radiated electric field at the spatial test point to the signal at the input of the emitting antenna:

$$H_{TA}^{total}(\omega, \theta, \varphi, R) = \frac{E(\omega, \theta, \varphi, R)}{V_{in}} \quad (2.17)$$

The \vec{E} field can be taken anywhere in space but, in practice, we consider it is taken at the place where the receiving antenna is placed. The receiving antenna transfer function is defined as the ratio of the output signal of the receiving antenna to the incident electric field. The receiving antenna transfer function is:

$$H_{RA}(\omega, \theta, \varphi) = \frac{V_{out}}{E(\omega, \theta, \varphi, R)} \quad (2.18)$$

Note that, even if it not explicit in the expression, H_{RA} depends on the point where the receiving antenna is placed from the emitting antenna defined by (θ, φ) and on its orientation. H_{RA} depends on the antenna geometry and physical parameters (material of substrate, impedance match to output port). H_{TA}^{total} depends on the same parameters but also on the propagation, rather communication channel, comprised between the physical emitting antenna and the place where \vec{E} is measured by the receiving antenna. It is convenient to separate the communication channel from the antenna itself wherever possible. It is the case in the far-field region where it is well known that the fields decrease as:

$$H_{ch}(\omega, R) = \frac{e^{-jkR}}{R} \quad (2.19)$$

where $k = 2\pi/\lambda$ is the free space wave number, and R is the distance between the transmitting antenna and receiving antenna. In this case, the emitting antenna transfer function can be rewritten as:

$$H_{TA}^{total}(\omega, \theta, \varphi, R) = H_{TA}(\omega, \theta, \varphi) * \frac{e^{-jkR}}{R} = \frac{E(\omega, \theta, \varphi, R)}{V_{in}} \quad (2.20)$$

then

$$H_{TA}(\omega, \theta, \varphi) = \frac{E_o(\omega, \theta, \varphi)}{V_{in}} \quad (2.21)$$

which depends only on the direction of emission of interest. The term e^{-jkR} takes into account the variation of the wave phase with distance, while $\frac{1}{R}$ is related to the variation of amplitude with distance (for an isotropic antenna power decreases with $\frac{1}{R^2}$ then the amplitude with $\frac{1}{R}$). The fact that the antenna does not have an isotropic radiation pattern is included in $E_o(\omega, \theta, \varphi)$ and in $H_{TA}(\omega, \theta, \varphi)$.

To summarize:

$$\text{From (2.16): } V_{out} = H(\omega, \theta, \varphi, R)V_{in} \quad \text{with } H(\omega, \theta, \varphi, R) = \frac{S_{21}}{2}$$

$$\text{From (2.17) and (2.20): } E(\omega, \theta, \varphi, R) = H_{TA}^{total}(\omega, \theta, \varphi, R)V_{in} = H_{TA}(\omega, \theta, \varphi) * H_{ch}(\omega, R)V_{in}$$

In the far-field region $H_{ch}(\omega, R) = \frac{e^{-jkR}}{R}$. The expression in near-field region is more complicated.

$$\text{From (2.18): } V_{out} = H_{RA}(\omega, \theta, \varphi)E(\omega, \theta, \varphi, R)$$

Finally; by combining these last three expressions:

$$\frac{V_{out}}{V_{in}} = H_{TA}(\omega, \theta, \varphi)H_{ch}(\omega, R)H_{RA}(\omega, \theta, \varphi) = H(\omega, \theta, \varphi, R) = \frac{S_{21}}{2} \quad (2.22)$$

Remark 1: in the case of our applications, for which some energy lies at frequencies corresponding to the near-field, or even in the reactive near-field, it is still possible to use the formalism based on the separation of the emitting antenna properties and of the communication channel in the form

$$H_{TA}^{tot}(\omega, \theta, \varphi, R) = H_{TA}(\omega, \theta, \varphi) * H_{ch}(\omega, R).$$

Remark 2: Another definition is obtained by replacing equation (2.17) by:

$$H_{TA1}^{tot}(\omega, \theta, \varphi, R) = \frac{E(\omega, \theta, \varphi, R)}{V_{in}^{ant}} \quad (2.23)$$

This second definition makes sense at high frequencies since, in practice, it is not easily possible to measure V_{in} (the ideal source generator voltage). On the contrary, V_{in}^{ant} is the voltage associated to the output of the AWG, the same way V_{out} is the voltage read by the oscilloscope that is matched to the device under test (usually at 50Ω impedance). Consequently, the different definitions depend on the different ways to configure the generator and oscilloscope.

In the case of the definition of equation (2.23), equation (2.16) becomes:

$$\frac{V_{out}}{V_{in}^{ant}} = H_1(\omega, \theta, \varphi, R)$$

From (2.8) and (2.14):

$$\frac{V_{out}}{V_{in}^{ant}} = \frac{1}{A + B/Z_{out}} = \frac{S_{21}}{1 + S_{11}}$$

Then

$$\frac{V_{out}}{V_{in}^{ant}} = \frac{S_{21}}{1 + S_{11}} = H_1(\omega, \theta, \varphi, R) = H_{TA1}(\omega, \theta, \varphi)H_{ch}(\omega, R)H_{RA1}(\omega, \theta, \varphi) \quad (2.24)$$

A third definition is taken by measuring the input and output voltages of the antenna when it is not connected to a load at the output. Though it corresponds to a non-desirable case, with a high reflection at the output, it is an obvious definition for very low frequencies. In this case, equation (2.2) is replaced by:

$$\frac{V_{out}(I_{out} = 0)}{V_{in}^{out}} = H_2(\omega, \theta, \varphi, R) \quad (2.25)$$

Since $I_{out} = 0$ (see Figure 2.3), from (2.6):

$$V_{in}^{ant} = AV_{out}$$

and

$$H_2(\omega, \theta, \varphi, R) = \frac{1}{A}$$

then

$$\begin{aligned} \frac{V_{out}(I_{out} = 0)}{V_{in}^{out}} &= \frac{2S_{21}}{(1 + S_{11})(1 - S_{22}) + S_{12}S_{21}} = H_2(\omega, \theta, \varphi, R) \\ &= H_{TA2}(\omega, \theta, \varphi)H_{ch}(\omega, R)H_{RA2}(\omega, \theta, \varphi) \end{aligned} \quad (2.26)$$

The transfer functions H, H_1 and H_2 can be expressed in more details by using the reciprocity theorem ($S_{ij} = S_{ji}$) [24, 25] that states for two identical antennas, that:

$$H_{TA}(\omega, \theta, \varphi) = \frac{j\omega}{2\pi c} H_{RA}(\omega, \theta, \varphi) \quad (2.27)$$

From (2.22):

$$H(\omega, \theta, \varphi, R) = \frac{j\omega}{2\pi c} H_{RA}^2(\omega, \theta, \varphi) H_{ch}(\omega, R) = \frac{S_{21}}{2}$$

then

$$H_{RA}^2(\omega, \theta, \varphi) = \frac{2\pi c}{j\omega} [H_{ch}(\omega, R)]^{-1} H(\omega, \theta, \varphi, R)$$

$$H_{RAi}(\omega, \theta, \varphi) = \sqrt{H_i(\omega, \theta, \varphi, R) \frac{2\pi c}{j\omega} \frac{1}{H_{ch}(\omega, R)}} \quad (2.28)$$

$$H_{TAi}(\omega, \theta, \varphi) = \sqrt{H_i(\omega, \theta, \varphi, R) \frac{j\omega}{2\pi c} \frac{1}{H_{ch}(\omega, R)}} \quad (2.29)$$

For the case where:

$$H(\omega, \theta, \varphi, R) = \frac{S_{21}}{2}$$

and for the far-field region where:

$$H_{ch}(\omega, R) = \frac{e^{-jkR}}{R}$$

one obtains:

$$H_{RA}(\omega, \theta, \varphi) = \sqrt{\frac{S_{21}}{2} \frac{2\pi c}{j\omega} R e^{jkR}} \quad (2.30)$$

$$H_{TA}(\omega, \theta, \varphi) = \sqrt{\frac{S_{21}}{2} \frac{j\omega}{2\pi c} R e^{jkR}} \quad (2.31)$$

For the two other definitions of the transfer functions, $\frac{S_{21}}{2}$ should be replaced by:

$$\frac{S_{21}}{1 + S_{11}} \quad \text{or} \quad \frac{2S_{21}}{(1 + S_{11})(1 - S_{21}) + S_{12}S_{21}}$$

2.4 Baseband Transmission of line codes

The digital data input in frequency domain are obtained by Fast Fourier transform (FFT) as in the previous chapter. Equation (2.16) gives the expression of the transfer function that can be used to simulate the performance of the antenna system for the transmission of digital data with the procedure shown in figure 2.4. The procedure is basically a multiplication of the line code in frequency domain with the transfer function of the system.



Figure 2.4 Procedure used to simulate the transmission of Polar RZ and Manchester line codes in the frequency domain with an antenna transmission transfer function. FT: Fourier Transform; T.F: Transfer Function; DSP: Digital Signal Processing.

The antenna transmission transfer function is described by S-parameters when the antenna system is considered as a two port network. As shown before the overall transfer function of the antenna system is $S_{21}/2$ where S_{21} is the forward gain. For a two-port device the four S-parameters describe the properties of the set of emitting and receiving antennas: S_{11} and S_{22} are the forward and reverse reflection coefficients while S_{21} and S_{12} are the forward and reverse gains. For the case of an ideal transmission within the bandwidth of the antennas: $S_{11} = S_{22} = 0$ and $S_{21} = S_{12} = 1$ while for out of band components: $S_{11} = S_{22} = 1$ and $S_{21} = S_{12} = 0$.

For our study where both antennas are assumed identical and according to the scattering matrix properties for lossless networks [25], are has the relation:

$$|S_{11}|^2 + |S_{21}|^2 = 1 \quad (2.32)$$

We used the following S-parameters: $S_{12} = S_{21} = -60dB$ outside the bandwidth and $S_{12} = S_{21} = -9dB$ within the bandwidth of the antenna, as shown in figure 2.5.

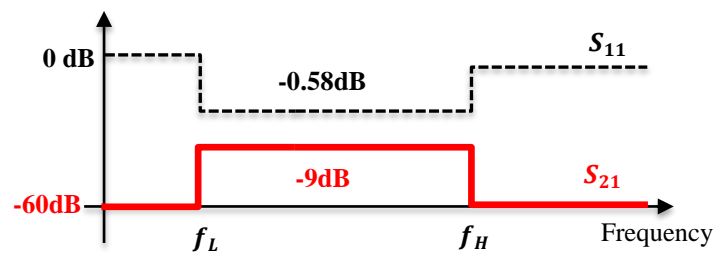


Figure 2.5 S-parameters used for the set of emitting and receiving antennas. f_L and f_H represent respectively the lower and the upper theoretical frequency of the antenna bandwidth.

According to the energy conservation of equation (2.32), the reflection coefficients are $S_{11} = S_{22} = -0.58\text{dB}$ inside the bandwidth and $S_{11} = S_{22} \approx 0\text{dB}$ outside the bandwidth. The values chosen for in-band signals correspond to what is reasonably expected for the transmission of signals over a few centimeters without any focusing system.

2.5 Estimation BER for Polar RZ and Manchester encodings

In order to improve the quality of the transmission of the digital signal two different approaches are considered to calculate the BER of digital output signal. The first approach is based on using the average value of samples for each bit, and the second approach is based on using a specific sample for each bit.

2.5.1 BER calculation based on averaging values of bit samples

A method was developed to calculate the BER of the transmission to compare different configurations. It is dependent on the number of samples N taken for each bit of duration T_b of the input digital signal. The method calculates the average value of samples from the first half of each bit, corresponding to $N/2$ points taken over the $(0 \rightarrow \frac{T_b}{2})$ time period as shown in figure 2.6.

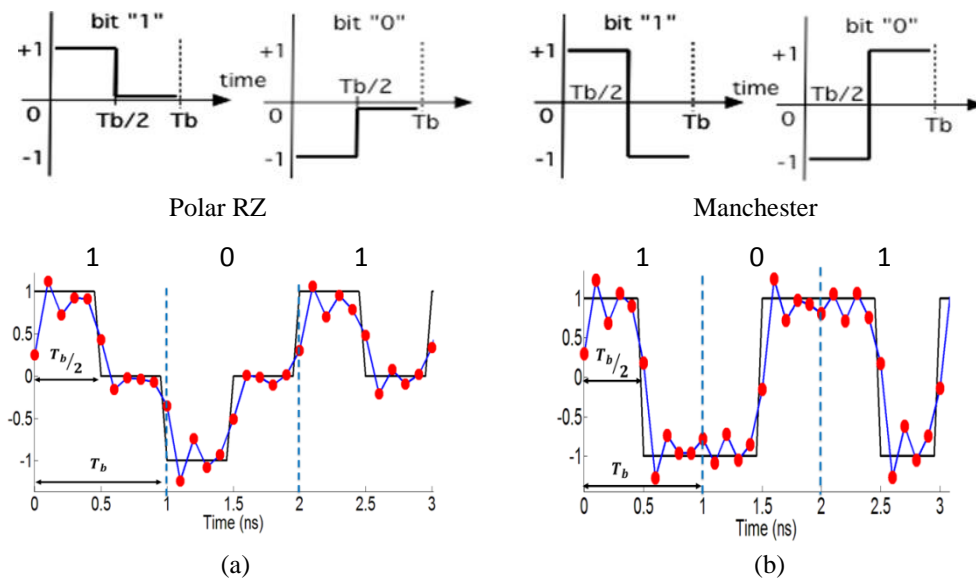


Figure 2.6 Sampling method used to calculate the output digital signal and deduce the BER, illustrated for Polar RZ and Manchester encoding for which the digital sequence [1 0 1] is represented. Only the samples of the first half of each bit are used to calculate the average value of the half-bit. This average is transformed in a "1" or "-1" level, depending on the sign of the average. The second part of the bit is automatically set to the "0" level according to the Polar RZ encoding used to find the bits. The sequence of the two levels of the bit, "-1&0" or "1&0", corresponds respectively to a digital "0" or "1" with Polar RZ encoding. The resulting digital output signal is also valid for Manchester encoding.

Depending on the sign of the average, it is converted to a "1" or "-1" level. The remaining second half of each bit, that corresponds to the next $N/2$ samples of the $(\frac{T_b}{2} \rightarrow T_b)$ time period, is automatically converted to "0" level. Depending on the value of the couple of levels obtained for the two parts of each bit ("1&0" or "-1&0"), and assuming that the Polar RZ encoding is used, it is possible to deduce the value of the bit : "-1&0" corresponds to bit "0", while the sequence "1&0" corresponds to bit "1". Let us notice here that, when the Manchester encoding is used, the average of the first half of the bit gives the same level as for Polar RZ encoding: "1" level corresponds to bit "1" and "-1" level to bit "0".

Consequently the described method works to find the bits associated with both encodings.

In the next step, to compare the output signal with the input signal sent to the transmission antenna, the output signal is reconstructed from the digital output sequence obtained with the described method, with its proper encoding (for instance a "1" bit with Manchester encoding is drawn as shown in figure 2.6 b).

In a last step the BER is calculated by comparing the input and output values for each bit. It is the sum of the number of errors divided by the total number of bits.

Figure 2.6 illustrates the BER calculations approach for two encoded signals.

- ❖ The encoding has $n = 10$ samples (values) for every bit of the digital output signal (blue line and red points) as shown in figure 2.6.
- ❖ The first five values are averaged and transformed in 1 or -1 with the "sign" function.
- ❖ The last five values are transformed into zeros, this is done with every bit of the digital output signals.
- ❖ Finally, the digital output signal is converted to ones or minus ones and zeros.
- ❖ This technique allows us to remove 50% of errors when converting the second half of each bit to zero, and requires a very short processing time.
- ❖ The advantage is that it does not depend on the input signal.

2.5.2 BER calculation based on specific sampling of each bit

This method is based on using a specific position of a sample for each bit of duration(T_b). Figure 2.7 shows an overview of the processing method used for BER calculation.

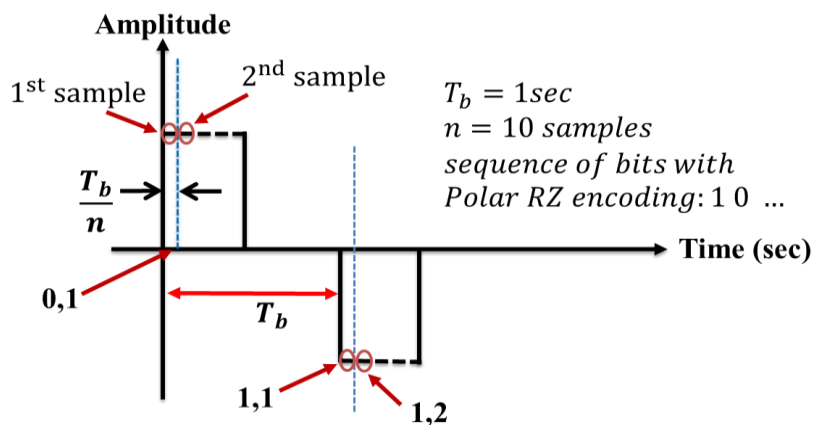


Figure 2.7 Approach to calculate the BER of digital output signal based on specific sampling.

The value of the bits is deduced from the value of only one sample at instant $(mT_b + \frac{T_b}{n})$ where n is an integer corresponding to the number of samples per bit. The value of the bit is obtained by taking the “sign” of the sample. If the value of the output bit is different from the input one then the next sample at $(mT_b + \frac{2T_b}{n})$ is taken, and so on, until the real value is found. This approach assumes that the input signal is known to optimize the procedure, which is acceptable if the antenna system properties are known and do not change.

2.6 Baseband transmission of line codes at 1Gbps data rate

In this section, two different approaches are used to perform simulations. The first approach is based on using the first harmonic of the digital signal to send and receive. The second approach uses higher harmonics.

2.6.1 Transmission of the first harmonic of the digital signal

Simulations in the frequency domain have been done with two identical antennas. Figure 2.8 shows the transmission characteristics of the antenna system for Polar RZ and Manchester line codes. The input data stream and the antenna transmission transfer function are multiplied in the frequency domain, while the output data is shown in the time domain after inverse FFT. The comparison between the digital input and output signals of Figure 2.8 (d) is shown for a total antenna bandwidth $f_H - f_L$ (see Figure 2.5) which is limited to the 0-10 GHz range in practice in the present case.

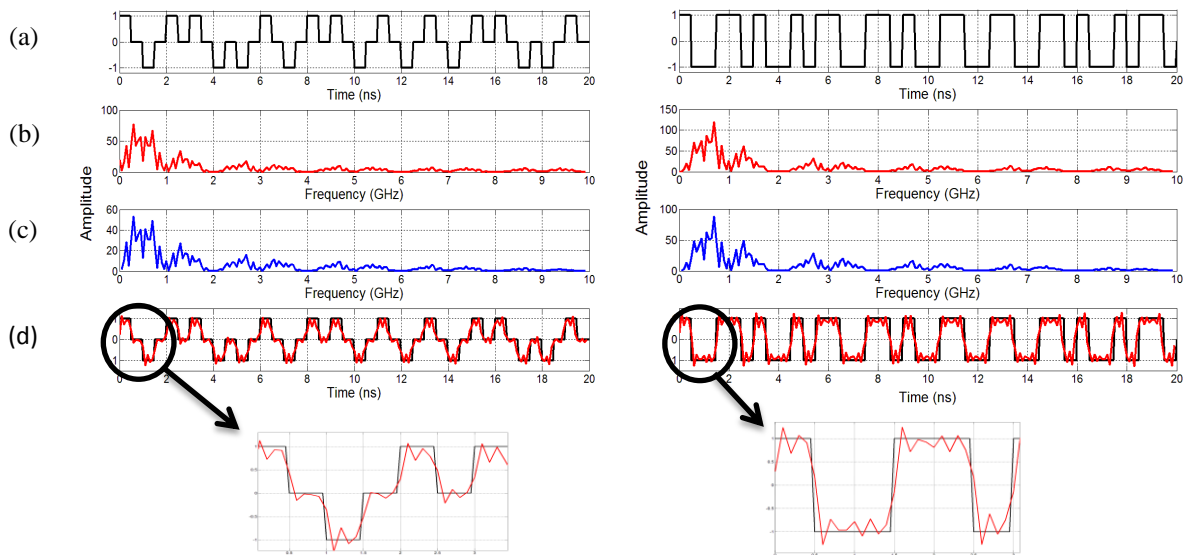


Figure 2.8 Simulations of Polar RZ (left) and Manchester (right) line codes at 1Gbps for a 20 bits input sequence [101100101101011001]. The antenna bandwidth $f_H - f_L$ is supposed infinite in theory and limited by the sampling rate in practice. (a) Data input of encoded signal (b) Frequency spectrum at input of transmission antenna. (c) Output signal at the receiver antenna. (d) Inverse FFT of the output signal of the receiving antenna superposed with the digital input signal.

It is observed that the output digital signal agrees well with the input digital signal when the total bandwidth is considered for the transmission.

The first harmonic of the line code contains about 80% to 90% of the power of the original digital data. For Polar RZ encoding at 1Gbps, the first harmonic ranges from 0 to 2 GHz ($f_L = 0, f_H = 2GHz$). As a first approach the input signal has been filtered over this bandwidth in the transfer function expression deduced from the S-parameters of figure 2.5. Simulated results are shown in figure 2.9. Polar RZ and Manchester encodings are reminded in Figure 2.6.

It is seen that the received signal agrees well with the digital input. Wireless Baseband Transmission requires a broad bandwidth, hence an appropriate design of the antenna is crucial. Consequently a study of the optimum bandwidth compatible with a compact antenna size is necessary for our application.

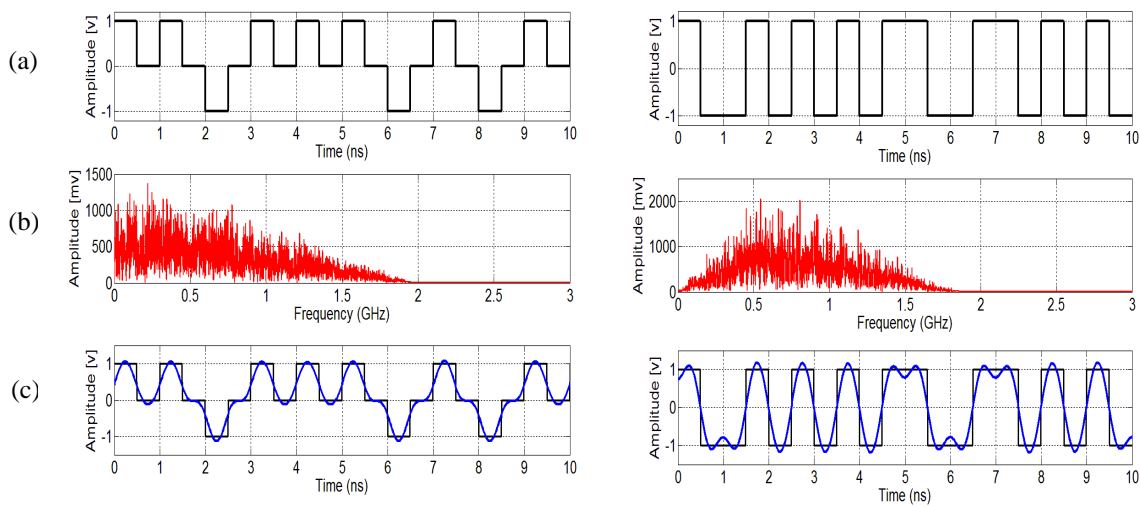


Figure 2.9 Simulations of the transmission of Polar RZ (left) and Manchester (right) line codes across a theoretical set of antennas with 0-2 GHz bandwidth according to the S-parameters of Figure 2.5. (a) Input data with Polar RZ and Manchester encoding at 1Gbps. (b) FFT of encoded signals where the transmission bandwidth is limited to 0-2 GHz. (c) Comparison of input and output signals.

2.6.1.1 Study of BER for different transmission bandwidths

In the previous section, we have observed that using the first harmonic is satisfactory to transmit and receive the signal. Wireless baseband transmission scheme requires an ultra-broad bandwidth and the antenna becomes a critical device. Using a narrower bandwidth associated to smaller size antennas becomes a crucial point when using the WBT scheme.

We studied the BER for different theoretical bandwidths of the antenna system in order to help the design of the proper antennas to be fabricated and used to transmit the digital signals directly in the base frequency band. Figure 2.10 shows the dependence of the BER for different bandwidths centered at a frequency of 1 GHz.

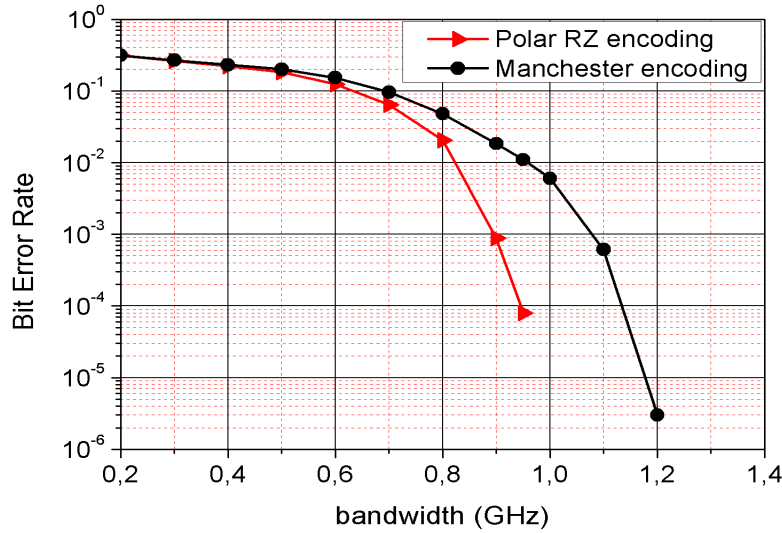


Figure 2.10 BER versus bandwidth of transmission for a digital signal at 1Gbps made of a random pattern of 2^{20} bits, with Polar RZ and Manchester line codes.

Figure 2.10 shows the dependence of the BER for different bandwidths centered at a frequency of 1 GHz. A random sequence of 2^{20} bits (1,048,576 bits) at 1Gbps has been used with both Polar RZ and Manchester encodings. Each bit comprised 12 samples. The bandwidth of 2 GHz corresponds to the signals shown in figure 2.9, with $f_L = 0$ GHz and $f_H = 2$ GHz.

Figure 2.10 shows that the BER improves substantially to reach values below 10^{-4} from 0.9 GHz for Polar RZ and from 1.15 GHz for Manchester encoding. The minimum frequency f_L of 0.5 GHz allows to reduce substantially the antenna size compared to the 2 GHz bandwidth since low frequencies, associated with longer wavelengths and consequently to larger antenna size, do not need to be transmitted. Consequently a bandwidth of 1 GHz is chosen as a reasonable trade-off between a compact antenna size, associated with the minimum frequency that can be transmitted, and a low BER that depends on the total frequency range of the transmitted digital signal. Nevertheless one can see in figure 2.10 that the Manchester encoding is not as performant as Polar RZ, probably because a lower proportion of the energy is concentrated around 1 GHz.

2.6.1.2 Influence of SNR on BER

To estimate the expected performance of the transmission in conditions reflecting a real system, a gaussian noise has been added to the digital signal to estimate the BER with a Signal to Noise Ratio (SNR) varying from 0dB to 20dB.

Simulations have been performed by adding the noise either to the input digital signal or to the output signal with a 2^{16} bit-code pattern. Results are displayed in figure 2.11 for both Polar RZ and Manchester line codes for the 1 GHz bandwidth centered at 1Gbps ($f_L = 0.5$ GHz & $f_H = 1.5$ GHz). The Manchester encoding is not as performant as Polar RZ, in agreement with figure 2.10, since the chosen bandwidth of 1 GHz is not high enough to reach a low bit error rate.

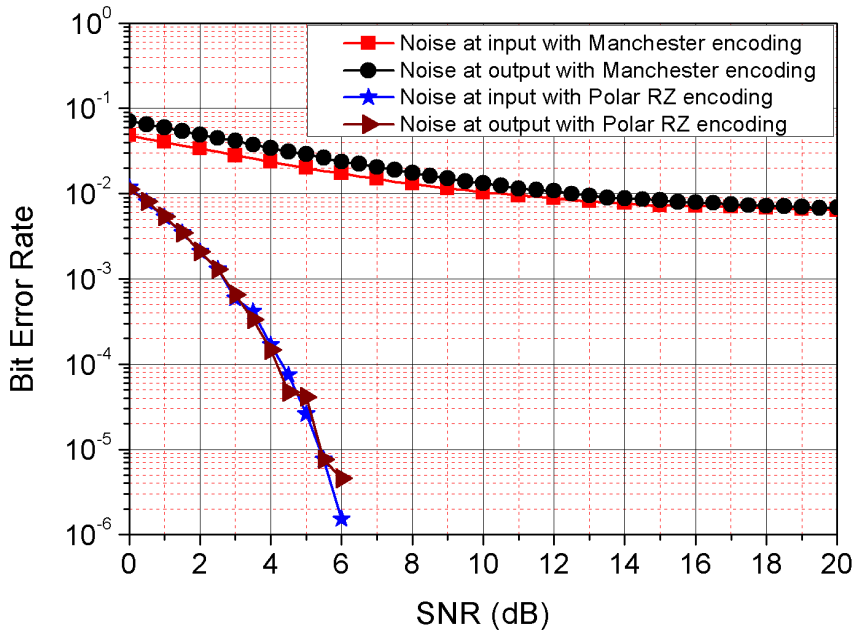


Figure 2.11 BER versus SNR for Polar RZ and Manchester encodings. A gaussian noise has been added to the input or the output digital signal for a code pattern of 2^{16} random bits with 12 samples per bit. The bandwidth is 1GHz (0.5-1.5 GHz).

2.6.2 Use of higher harmonics of the digital signal

The first approach that was presented above requires a large size of antenna in order to transmit the encoded signals over the 0.5-1.5 GHz bandwidth. Because of this problem, we have selected a second approach which is based on a higher number of samples per bit to use rather the higher harmonics of the signal. WBT properties have been simulated using the same procedure shown in figure 2.4.

Since baseband signals are radiated directly, a wide relative bandwidth is used. Interferences with other wireless systems become an important problem. In this context, the UWB spectrum has been limited between 3.1 and 10.6 GHz. To reach such frequencies, a higher sampling rate is necessary. The simulations of the power spectrum of Manchester and Polar RZ encoded signals at 1Gbps are shown in figure 2.12 for 24, 12, and 8 samples per bit. Consequently the Nyquist frequency is pushed at higher values and the upper frequency of the FFT increases with sampling rate while the frequency resolution still depends on the total number of bits of the digital pattern. Increasing the sampling rate per bit leads to a higher frequency harmonic content that can be used to retrieve the signal of interest. The other advantage is that antennas can be made smaller to transmit signals at higher frequencies. Therefore it opens the way to smaller antennas to transmit the digital signals through WBT.

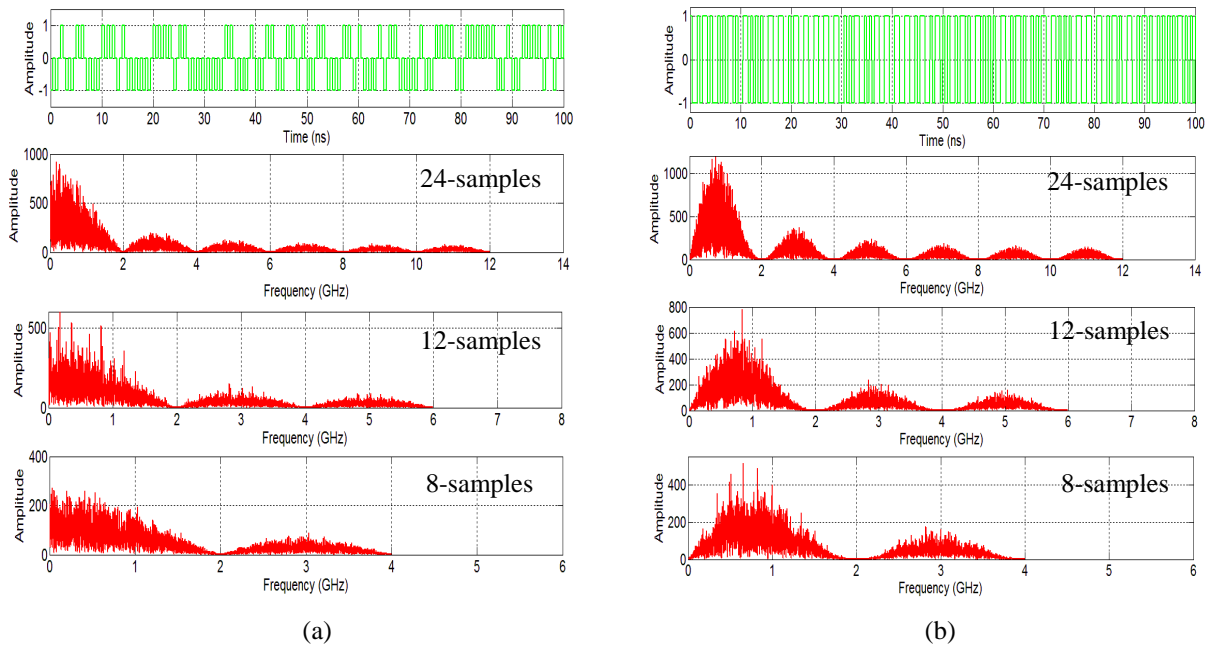


Figure 2.12 Simulated FFT for (a) Polar RZ encoding and, (b) Manchester encoding, with a data rate of 1Gbps and a 1000 bit-code pattern. Results are shown for 24, 12 and 8 samples per bit.

Since the UWB spectral window ranges from 3.1 to 10.6 GHz, a small size antenna structure is required. For data rate at 1Gbps a lower cutoff frequency of 4 GHz makes sense, as it corresponds to the 3rd and higher harmonics. Consequently, simulations have been done for two different bandwidths:

- ❖ 4-6 GHz bandwidth with 12 samples per bit (harmonic 3).
- ❖ 4-12 GHz bandwidth with 24 samples per bit (harmonics 3 to 6).

The power spectrum simulations of Manchester and Polar RZ encoded signals at a data rate of 1Gbps are shown in Figure 2.13 for 24 and 12 samples per bit.

The number of samples per bit plays an important role to reach the power at higher frequencies. The Nyquist frequency is given by:

$$f_{max} = \frac{N_s}{2T_b} \tag{2.33}$$

where N_s is number of samples per bit and T_b is the bit duration.

Therefore, one of the key requirements of this approach is to be able to miniaturize the antenna size with high data rate. Based on this idea, the upper frequencies for two encoded signals can be calculated with (2.33).

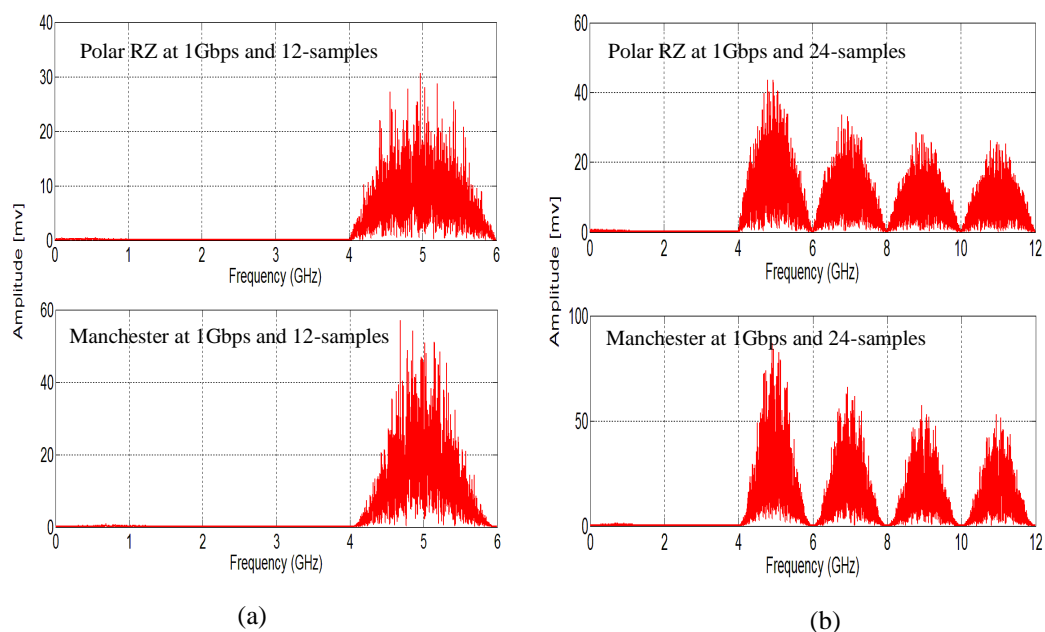


Figure 2.13 Simulations of FFTs for two encoded signals at a data rate of 1Gbps with a 1000-bit code pattern. (a) Manchester and Polar RZ encoded signals using 12 samples per bit (BW=4-6GHz). (b) Manchester and Polar RZ encoded signals using 24 samples per bit (BW= 4-12GHz).

Simulations of Wireless Baseband Transmission for both Manchester and Polar RZ encodings at a data rate of 1Gbps with 12 and 24 samples per bit using 20 bits and 2^{16} bits code patterns are presented in figure 2.14 and figure 2.15. Signals are filtered so that no frequency below 4 GHz is transmitted.

It is seen that the recovered received signal agrees well with the input noiseless digital input when the bandwidth range 4-6 GHz and 4-12 GHz are considered for the transmission.

Simulations have been done with 8 samples per bit of digital data input. In this case in order to verify the accuracy of the suggested method the bandwidth ranges from 0 to 4GHz. Since the UWB bandwidth is 3.1-10.6 GHz, the only transmitted frequency range is 3.1-4 GHz, corresponding to 0.9 GHz bandwidth. We observed higher BER with this case.

Figure 2.16 shows the simulations of WBT with digital data at a rate of 2Gbps with 2^{16} bits code pattern using 6 samples per bit, where one sees that the output signal is detected correctly.

From the above results, one can conclude that Polar RZ and Manchester encoded signals are suitable for wireless baseband transmission at high data rate with small size antennas with the lower operating frequency of antenna at 4GHz.

The number of samples per bit and the data rate play an important role in this communication system since the transmitted energy is mostly located in the high frequency part of the associated digital signal spectrum. The important factors in WBT are the choice of antennas and transmission codes. Consequently a study of the optimum bandwidth compatible with a compact antenna size is necessary for our application.

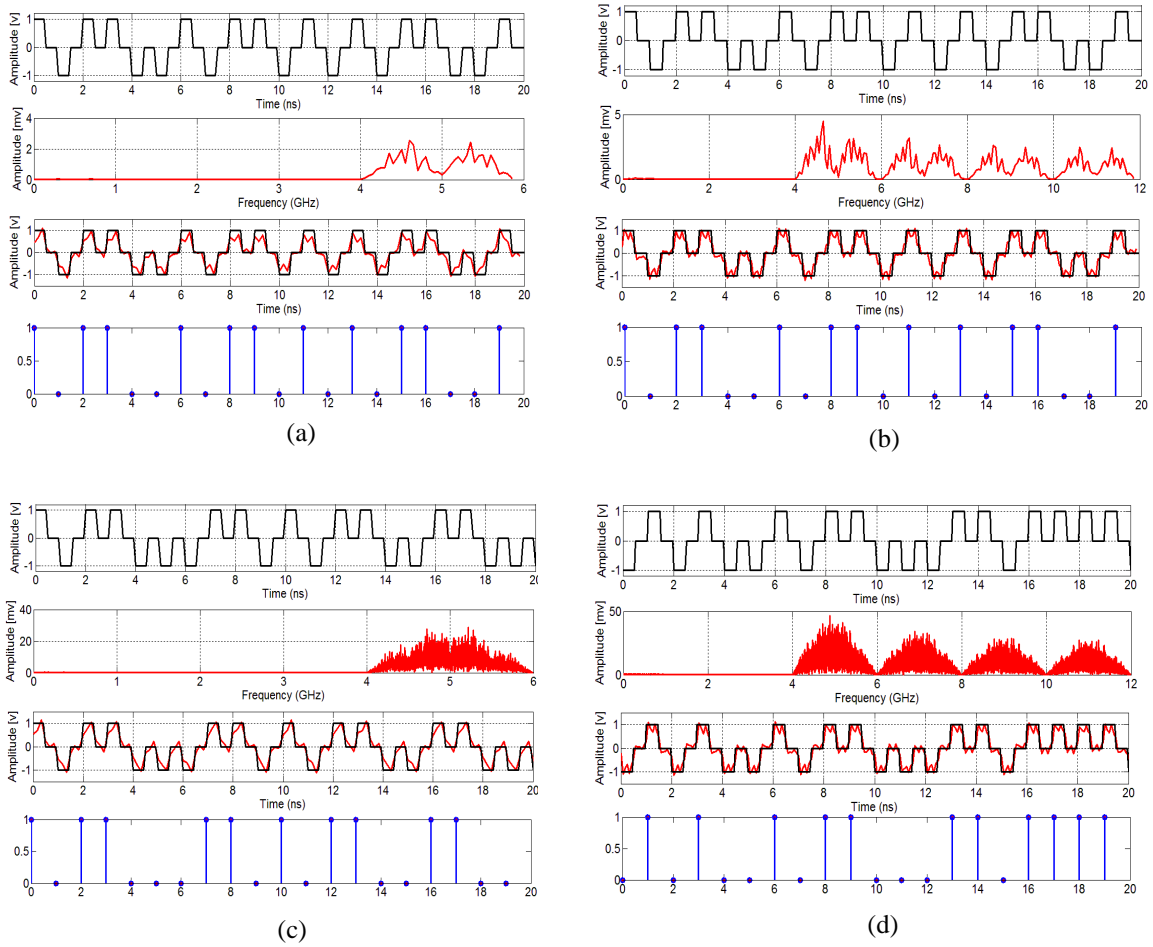


Figure 2.14 Simulations of WBT with Polar RZ encoded signal at a data rate of 1Gbps. (a) with a 20 bits code pattern using 12 samples per bit. The bandwidth is 4-6 GHz. (b) with a 20 bits code pattern using 24 samples per bit. The bandwidth is 4-12 GHz. (c) with 2^{16} bits code pattern using 12 samples per bit. The bandwidth is 4-6 GHz. (d) with 2^{16} bits code pattern using 24 samples per bit. The bandwidth is 4-12 GHz.

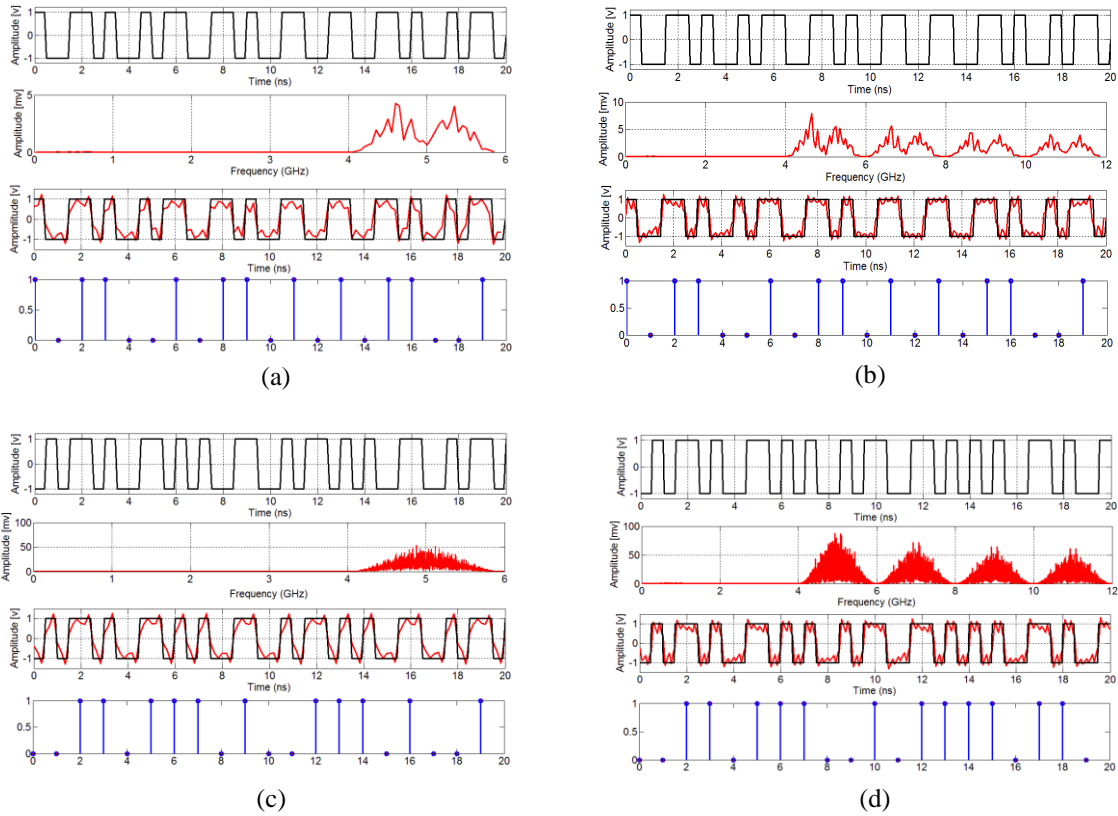


Figure 2.15 Simulations of WBT with Manchester encoded signal at a data rate of 1 Gbps. (a) with a 20 bits code pattern using 12 samples per bit. The bandwidth is 4-6 GHz. (b) with a 20 bits code pattern using 24 samples per bit. The bandwidth is 4-12 GHz. (c) with a 2^{16} bits code pattern using 12 samples per bit. The bandwidth is 4-6 GHz. (d) with a 2^{16} bits code pattern using 24 samples per bit. The bandwidth is 4-12 GHz.

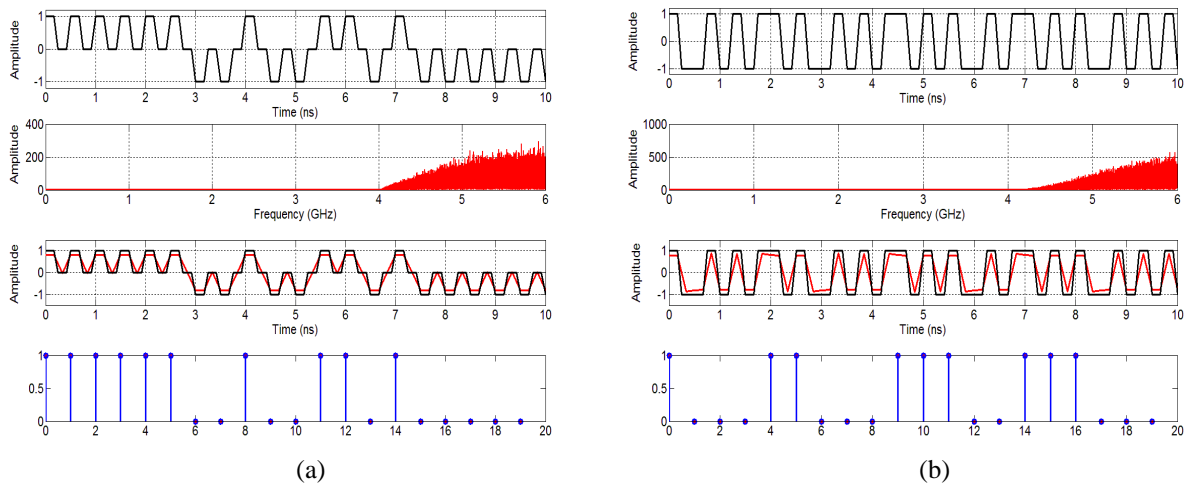


Figure 2.16 Simulation of WBT for two encodings at a data rate of 2 Gbps with a 2^{16} bits code pattern using 6 samples per bit. The bandwidth ranges from 4 GHz to 6 GHz. (a) Polar RZ encoding. (b) Manchester encoding.

2.7 Conclusion

In this chapter, a baseband transmission scheme for wireless communications has been proposed. Simulations to transmit and receive digital data from a set of antennas directly at a data rate of 1Gbps and 2Gbps have been done.

Two methods were developed to calculate the BER of the transmission to compare different configurations. The first technique allows us to remove most of errors when converting the second half of each bit to zero and requires a very short processing time. It does not depend on the input signal while the second technique depends on the input signal and requires a long processing time.

Two simulation approaches are proposed to study the transmission of digital data streams with Manchester and Polar RZ signals directly from an antenna without any modulation technique.

The first approach uses the first harmonic of the signal. It is found that the minimum bandwidth from 0.5 to 1.5 GHz gives BER values below 10^{-4} from 0.9 GHz bandwidth for Polar RZ and from 1.15 GHz for Manchester encoding. The minimum frequency f_L of 0.5 GHz allows to reduce substantially the antenna size compared to the 2 GHz bandwidth since low frequencies are associated with longer wavelengths and consequently to larger antenna size. Because of this problem, we have selected another approach which is based on a higher number of samples per bit to use rather the higher harmonics of the signal. The simulations of the power spectrum of Manchester and Polar RZ encoded signals at 1Gbps were done for 24, 12, and 8 samples per bit.

With more samples per bit the Nyquist frequency is pushed at higher values and the upper frequency of the FFT increases while the frequency resolution still depends on the total number of bits of the digital pattern. The other advantage is that antennas can be made smaller to transmit signals at higher frequencies. Therefore it opens the way to smaller antennas to transmit the digital signals through WBT.

Bibliography

- [1] H. HA. Nguyen, and ED. Shwedyk, "A First Course in Digital Communications," Cambridge CB2 8RU, UK, 2009.
- [2] G.R Aiello, and G.D. Rogerson, "Ultra-Wideband Wireless Systems," IEEE Microwave Magazine, vol. 4, no. 2, pp. 36-47, June 2003.
- [3] M. Z. Win, and R. A. Scholtz, "Impulse Radio: How it works," IEEE Communications letters, vol. 2, no. 2, pp. 36-38, February 1998.
- [4] T. Taniguchi, J. Kitagawa, and Y. Karasawa, "Wireless Baseband Transmission MIMO Communication System," IEEE International Conference on Circuits and System for communication, Bucharest, Rumania, July 2006.
- [5] J. Kitagawa, T. Taniguchi, and Y. Karasawa, "Wireless Baseband Transmission Experiments," IEICE, Transaction on communication, vol.E89-B, no.6, pp.1815-1824, June 2006.
- [6] T. Taniguchi, J. Kitagawa, and Y. Karasawa, "MIMO Communication System Based on Wireless Baseband Transmission Scheme Under Multipath Environment", Department of Electronic Engineering Advanced Wireless Communication research Center (AWCC), the university of Electro-Communications, ,IEEE 1-5-1 Chofugaoka, Chofu, Tokyo, Japan, 2007.
- [7] CH. Subrahmanyam, and P. Kumar Babu. "Implementation of Different Code for Baseband Wireless Communication System", International journal of Engineering Research & Technology (IJERT) ISSN: 2278-0181 vol. 1, Issue 7, Sep. 2012.
- [8] D. Lamensdorf and L. Susman, "Baseband Pulse Antenna Techniques," IEEE Antennas and propagation Magazine, vol.36, no.1, Feb. 1994,
- [9] J. Kitagawa, T. Taniguchi and Y. Karasawa, "Transmission Characteristics of Wireless Baseband Transmission Under Multipath Environments Using Real-Valued Signal Analysis", the University of Electronics Communications in Japan, part 2, vol.90, no.10, 2007.
- [10] S. R. P. Diniz, A. B. E. da Silva, and L. S. Netto, "Digital Signal Processing System Analysis and Design," 2nd ed., Cambridge, 2010.
- [11] X. Qing, Z. N. Chen, and M. Y. W. Chia, "Characterization of ultra-wideband antennas using transfer functions," Radio science, Vol. 41, RS1002, pp. 1-10, Feb. 2006.
- [12] X. Qing, and Z. N. Chen, "Transfer Functions Measurement for UWB antenna", in IEEE AP-S International Symposium, vol. 3, pp. 2532-2535, June 2004.

- [13] Y. Duroc, A. Ghiotto, T. P. Vuong, and S. Tedjini, "UWB Antennas: Systems with Transfer Function and Impulse Response," *IEEE Transactions on Antennas and Propagation*, vol. 55, no. 5, May 2007.
- [14] Y. Duroc, T. P. Vuong, and S. Tedjini, "A Time/Frequency Model of Ultra-wideband Antennas," *IEEE Transactions on Antennas and Propagation*, vol. 55, no. 8, August 2007.
- [15] J. S. Zhang, and F. J. Wang, "Study of a Double printed UWB Dipole Antennas," *Microwave and Optical Technology Letters*, vol. 50, no. 12, December 2008.
- [16] Y. Duroc, R. Khouri, V. Beroulle, T. P. Vuong, and S. Tedjini, "Considerations on the Characterization and the Modelization of Ultra-wideband Antennas," *IEEE International conference on Ultra-Wideband*, 2007.
- [17] B. Scheers, M. Acheroy, and A. V. Vorst, "Time Domain Simulation and Characterization of TEM Horns using Normalized Impulse Response," *IEE Proceeding-microwaves Antennas and Propagation*, vol. 147, pp. 463-468, no. 6, December 2000.
- [18] S. Yiqiong, S. Aditya, and C. L. Law, "Transfer Function Characterization of UWB Antennas Based on Frequency Domain Measurement," *the European Conference on Wireless Technology*, vol. 3, pp. 277-280, 2005.
- [19] X. Qing and Z. N. Chen, and M. Y. W. Chia, "Network Approach to UWB Antenna Transfer Functions Characterization," *the European Conference on Wireless Technology*, vol. 3, pp. 293-296, 2005.
- [20] A. Dumoulin, M. John, P. Mcevoy, and M. Ammann, "An Enhanced method to Measure pulse Dispersion in UWB Antennas," *IEEE International Symposium on Antennas and propagation*, Chicago, IL, USA, 08-07-2012.
- [21] H. T. Friis, "A note on a simple transmission formula," *Proc. TRE*, vol. 34, no. 5, pp. 254-256, May 1946.
- [22] D. M. Pozar, *Microwave engineering*. Addison-Wesley, 1990.
- [23] D. A. Frickey, "Conversions between S, Z, Y, h, ABCD, and T parameters which are valid for complex source and load impedances," *IEEE Transaction on Microwave theory and Techniques*, vol. 42, no. 2, February 1994.
- [24] W. Sörgel and W. Wiesbeck, "Influence of the antennas on the ultra-wideband transmission," *EURASIP J. App. Signal processing*, pp. 296-3.5, 2005.
- [25] R. W. P. King, *the theory of linear antenna*, Cambridge, MA: Harvard University, 1956.

3 Study of UWB antennas for Wireless Baseband Transmission

3.1 Introduction

The key to transmitting high-data rate using wireless link is spectrum, since demand for data rate is directly translated to demand for available bandwidth. The development of wireless communication antennas with ultra-wide bandwidth is becoming important for several multiband applications. Ultra-wideband (UWB) technology becomes increasingly popular among researchers after the 3.1-10.6 GHz frequency band was available for commercial applications in 2002 due to the permission of the Federal Communication Commission (FCC) and has become a highly competitive topic in both academia and industry communities of telecommunications [1-8].

UWB technology is of interest for short-range applications, low-power transmission, low-cost transceivers and low-interference, multi-functionality, high-speed wireless communication system. For UWB applications antennas require a relatively flat gain, a stable group delay, and a linear phase characteristics through the entire band as well as low delays, low distortion, compactness, and lightweight. Therefore, compact UWB antennas with high efficiency and directional radiation patterns are desired for many applications such as: radar systems, high-resolution microwave imaging systems, remote sensing, RF jammer, electromagnetic compatibility (EMC) testing systems, phased arrays, and communication systems [4-7].

When a bandwidth of a few hundreds MHz is needed, it is preferable to transmit digital data in the base band directly with small size antennas placed in a short distance aligned configuration. In this case the challenge is to transmit a broad bandwidth without further need of down conversion. Besides, signals are transmitted through pulses that need to be processed in the time domain. For our application, UWB antennas are an appropriate choice for WBT since we need to transmit digital data at high rates, implying a broad bandwidth.

There are many different types of UWB antennas such as horn, spiral, bowtie, Vivaldi, monopole, loop, dipole [4-11]. A horn antenna is one of the best candidates for short-pulse wireless communication with wideband, high gain, linear polarization and directive pattern, it has also some drawbacks such as a large volume, not capable of working near the ground, high cost, and it needs a UWB balun to connect to coaxial cable.

The bow-tie antenna is the planar form of bi-conical antenna. It has a radiation pattern similar to the one of dipole antennas and a linear polarization. The spiral antenna has a compact dimension and gives the same beam width in both horizontal and vertical planes. The planar monopoles are extremely attractive to be used in emerging UWB applications, and growing research activity is being focused on them. It is a well-known fact that planar monopole antennas present really appealing physical features, such as

simple structure, small size, and low cost. Finally, one of the interesting types is the Vivaldi antenna with several advantages such as low cost, wide bandwidth, smaller volume, and aligned radiation.

In this chapter, a small size ultra-wideband Antipodal Vivaldi Antenna and a monopole antenna are studied. The proposed antennas have two important advantages: the first one has a wide bandwidth while the second one has a constant group delay or linear phase. Numerical techniques are employed in order to optimize antenna geometrical parameters and to meet the requirements of the antennas. Both antennas are simulated with 3-D High Frequency Structure Simulator (HFSS) based on the finite-element method (FEM). All measurements are implemented on the Agilent VNA Network Analyzer (37369A Anritsu).

3.2 Fundamental properties of antennas

In communication systems, the antenna is a device that transfers guided electromagnetic waves from one electronic system to another one at some distant location. Antennas are frequency-dependent devices, each antenna is designed for a certain frequency band. In order to describe the performance of an antenna, definitions of various parameters are necessary. In this section, we will define several important parameters representing the radiation characteristics in transmission and reception, as well as the circuit properties of antennas, and show how these can be computed from a field analysis.

3.2.1 Input impedance

The antenna impedance is the load for the transmitter or for the receiver. The input impedance is also defined as the ratio of the appropriate components of the electric to the magnetic field at a point or is the ratio between voltage and current at the antenna port. It varies with frequency as:

$$Z_{in}(f) = R_{in}(f) + jX_{in}(f)$$

The input antenna impedance can be represented as a circuit element in the system's microwave circuit.

The frequency response of an antenna at its port is defined as input impedance Z_{in} . Thus the antenna will be matched to the interconnecting transmission line and other associated equipment only with a certain bandwidth.

The input impedance can then be used to determine the reflection coefficient Γ and related parameters, such as Voltage Standing Wave Ratio (VSWR) and Return Loss (RL), as a function of frequency [12]:

$$\Gamma = (Z_{in} - Z_s)/(Z_{in} + Z_s) \quad (3.1)$$

where Z_s is the source impedance at the port. For a perfectly matched system, the VSWR is given by:

$$VSWR = (1 + |\Gamma|)/(1 - |\Gamma|) \quad (3.2)$$

A VSWR < 2 is necessary to get a good match and transmit by radiation of the antenna all of the input power at the antenna. Then the reflection at the antenna input is low, the return loss is given by:

$$RL = -20 \log |\Gamma| \quad (3.3)$$

The efficiency of an antenna is the ratio of the radiated power to the total power absorbed by the antenna. It can be expressed in terms of the radiation resistance R_r and loss resistance (R_l) [12, 13]:

$$\text{antenna efficiency}(\%) = 100 \cdot (R_r / (R_r + R_l)) \quad (\text{dimensionless}) \quad (3.4)$$

3.2.2 Radiation Pattern

The radiation pattern is a graphical representation of the electromagnetic power distribution in free space. The pattern can be considered to be representative of the relative field strength of the field radiated by antenna. The directivity of an antenna relates to its radiation pattern. For most cases, it is desirable that the radiation pattern is as close to isotropic as possible; however there are applications which require a directional radiation pattern. An omnidirectional radiation pattern means that the performance of the system is independent of the orientation of the antenna in one two-dimensional plane of reference and allows for more freedom and mobility of the antenna. figure 3.1 shows an example of radiation pattern of a dipole antenna.

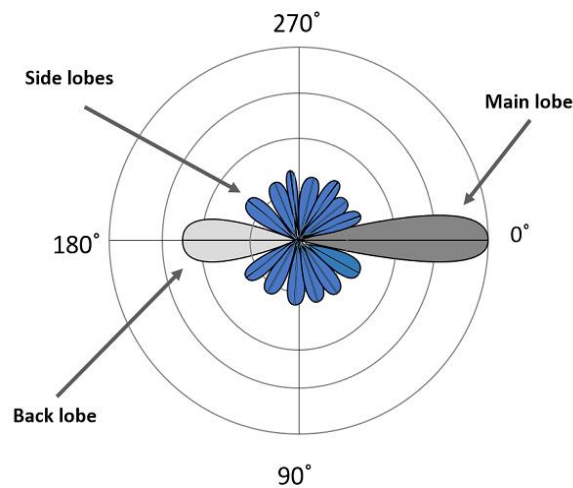


Figure 3.1 The radiation pattern of a dipole antenna. Here, the radiation pattern has a main lobe, side lobes and a back lobe.

The major part of the radiated field, which covers a larger area, is the main lobe or major lobe. This is the portion where maximum radiated energy exists. The direction of this lobe indicates the directivity of the antenna. The other parts of the pattern where the radiation is distributed side wards are known as side lobes or minor lobes. These are the areas where the power is wasted. There is another lobe, which is exactly opposite to the direction of the main lobe. It is known as back lobe, which is also a minor lobe.

The common types of radiation patterns are: (a) omni-directional pattern (also called non-directional pattern), the pattern usually has a doughnut shape in three-dimensional view: (b) pencil-beam pattern, the beam has a sharp directional pencil shaped pattern: (c) fan-beam pattern, the beam has a fan-shaped pattern: (d) shaped beam pattern, the beam which is non-uniform and patternless is known as shaped beam. A referential point for all these types of radiation is the isotropic radiation. It is important to consider the isotropic radiation even though it is impractical.

3.2.3 Bandwidth

The bandwidth (BW) is defined as a range within a band of frequencies or wavelengths. The bandwidth is also defined as the amount of data that can be transmitted in a fixed amount of time. In our case it is the range of frequencies over which the antenna can properly radiate or receive energy. Often, the desired bandwidth is one of the determining parameters used to decide upon an antenna. For instance, many antenna types have very narrow bandwidths and cannot be used for wideband operation. BW is typically quoted in terms of VSWR. For instance, an antenna may be described as operating at 100-400 MHz with a VSWR < 1.5. This statement implies that the reflection coefficient is less than 0.2 across the antenna bandwidth only 4% of the power is reflected back to the transmitter. The corresponding return loss is defined as:

$$S_{11} = 20 * \log_{10}(0.2) = -13.98dB$$

Also, the radiation pattern will vary with frequency. In general, the shape of the radiation pattern does not change radically. There are also other criteria which may be used to characterize BW. This may be the polarization over a certain range. For instance, an antenna may be described as having circular polarization with an axial ratio < 3dB from 1.4-1.6GHz. The BW is often specified in terms of its Fractional Bandwidth (FBW). The FBW is the ratio of the frequency range divided by the center frequency as:

$$FBW = (f_{max} - f_{min})/f_c = BW/f_c \quad (3.5)$$

where f_c is the center frequency. If FBW is equal to 20% or more the antenna is wideband. If FBW is equal to 50% or more the antenna is ultra-wideband. The quality factor Q of the antenna also relates to the bandwidth (as higher Q corresponds to a lower BW, and vice versa). The Q of an antenna is a measure of the BW of an antenna relative to the center frequency of the BW. If the antenna operates over a band between f_{min} and f_{max} with center frequency $f_c = (f_{max} + f_{min})/2$, then Q is given by:

$$Q = f_c/(f_{max} - f_{min}) \quad (3.6)$$

Antennas with a high Q are narrowband, antennas with a low Q are wideband. The higher the value of Q, the more sensitive the input impedance is to small changes in frequency. Also, the antenna bandwidth can be represented in a ratio bandwidth (BW_r) and is defined as:

$$BW_r = f_{max}/f_{min} \quad (3.7)$$

Another definition is the percentage bandwidth (BW_p) and is related to BW_r by [10, 11]:

$$BW_p = 200 \frac{f_{max} - f_{min}}{f_{max} + f_{min}} \% = 200 \frac{BW_r - 1}{BW_r + 1} \% = 100FBW\% \quad (3.8)$$

3.2.4 Friis Transmission Formula

This formula enables us to calculate the power received (P_r) given that a power (P_T) is radiated. Friis assumes that both antennas are isotropic and that they are in free space. To begin the derivation of the Friis equation, consider two antennas in free space (no obstruction nearby) separated by a distance R:

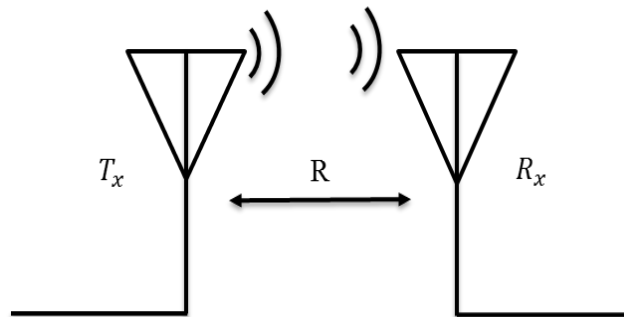


Figure 3.2 Transmission & reception antennas separated by the distance R.

Let's assume that P_T watts of total power are delivered to the transmission antenna. For the moment, assume that the transmission antenna is omnidirectional, lossless, and that the reception antenna is in the far field region of the transmission antenna. Then the power density P (in watts per square meter) of the incident plane wave on the reception antenna at a distance R from the transmission antenna is given by:

$$P = \frac{P_T}{4\pi R^2} \quad (3.9)$$

If the transmission antenna has an antenna gain in the direction of the reception antenna given by G_T then the power density equation above becomes:

$$P = \frac{P_T}{4\pi R^2} G_T \quad (3.10)$$

The gain takes into account the directionality and the losses of a real antenna. Assume now that the reception antenna has an effective aperture given by A_{ER} . Then the power received by this antenna P_R is given by:

$$P_R = \frac{P_T}{4\pi R^2} G_T A_{ER} \quad (3.11)$$

Since the effective aperture antenna can also be expressed as [1-10]:

$$A_{ER} = \frac{\lambda^2}{4\pi} G_R \quad (3.12)$$

The resulting received power can be written as:

$$P_R = \frac{P_T G_T G_R \lambda^2}{(4\pi R)^2} \quad (3.13)$$

where G_T and $G_R = 1$ for an isotropic antenna

This is known as the Friis Transmission formula. It relates the free path loss, the antenna gain and the wavelength to the reception and transmission powers. This is one of the fundamental equations in the antenna theory [1, 10, and 11].

3.2.5 S-parameters

Scattering parameters, also called S-parameters, belong to the group of two-port parameters used in two-port theory. Like admittance matrix (Y) and impedance matrix (Z), they describe the performance of a two-port device completely. However, they relate to the traveling waves that are scattered or reflected when a network is inserted into a transmission line of certain characteristic impedance Z_L . Therefore, S-parameters can be compared to reflection and through path of a pair of spectacles. S-parameters are important in microwave design because they are easier to measure and to work with at high frequencies than other kinds of two port parameters. The S-parameters for a two port device are defined as [12-15]:

$$\begin{pmatrix} |b_1|^2 \\ |b_2|^2 \end{pmatrix} = \begin{pmatrix} |S_{11}|^2 & |S_{12}|^2 \\ |S_{21}|^2 & |S_{22}|^2 \end{pmatrix} * \begin{pmatrix} |a_1|^2 \\ |a_2|^2 \end{pmatrix} \quad (3.14)$$

with:

- $|a_1|^2$ Power incident on the input of the network.

- $|a_2|^2$ Power incident on the output of the network.
- $|b_1|^2$ Power reflected from the input port of the network.
- $|b_2|^2$ Power reflected from the output port of the network.
- $|S_{11}|^2$ Power reflected from the input port and $|S_{12}|^2$ power transmitted from the output port.
- $|S_{21}|^2$ Power transmitted from the input port and $|S_{22}|^2$ power reflected from the output port.

Note: a, b, S, are effective values and not peak values of the corresponding sine functions. This means that S-parameters do relate traveling waves (power) to a two port's reflection and transmission behavior. Since the two port device is imbedded in a characteristic impedance of Z_o , these waves can be interpreted in terms of normalized voltage or current amplitudes. This is explained in figure 3.3:

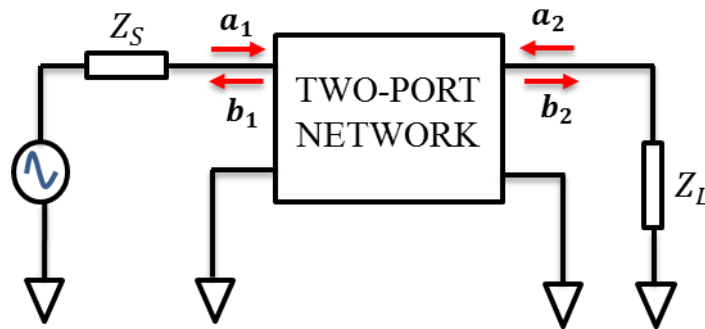


Figure 3.3 Signal flow graph for S-parameters interpretation in voltages.

The traveling wave variables a_1 , b_1 at port1 and a_2 , b_2 at port 2 are defined in terms of V_1 , I_1 and V_2 , I_2 and real valued positive reference impedance Z_o as follows:

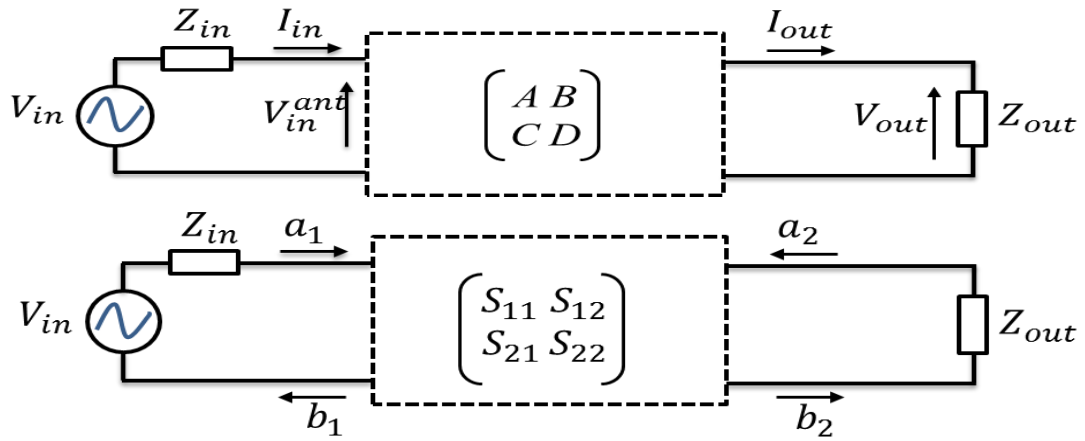
$$\begin{aligned}
 a_1 &= \frac{V_1 + Z_o I_1}{\sqrt{Z_o}} & a_2 &= \frac{V_2 - Z_o I_2}{\sqrt{Z_o}} \\
 b_1 &= \frac{V_1 - Z_o I_1}{\sqrt{Z_o}} & b_2 &= \frac{V_2 + Z_o I_2}{\sqrt{Z_o}}
 \end{aligned}
 \tag{3.15}$$

In practice, the reference impedance is chosen to be $Z_o = 50\Omega$. At lower frequencies the transfer function and impedance are commonly used, but at microwave frequency they become difficult to measure and therefore, the scattering matrix description is preferred. Typical network analyzers can measure S-parameters over a large frequency range, for example, an Anritsu 37369A vector network analyzer covers the range from 40 MHz to 40GHz [14].

The creation of the transfer function was discussed in section 2.3, and it was illustrated with two identical antennas in Figure 2.2. The transfer functions based on voltage ratio definition are described by *ABCD* parameters and S-parameters when the antenna system is considered as a two-port network. The system transfer function is the voltage ratio V_{out}/V_{in} , *ABCD* parameters describe the relationship

of the input and output voltages and currents. Therefore, the transfer function of the antenna system, which is defined by a voltage ratio, can be easily described by the $ABCD$ parameters.

The S-parameters can be measured with a Vector Network Analyzer (VNA) at very high accuracy, while the $ABCD$ parameters cannot be obtained easily because it is difficult to measure the voltage and current at microwave frequencies. Therefore, the antenna system Transfer Function is derived from $ABCD$ parameters and then converted to S-parameters. Also, the S-parameters can be converted back and forth into the $ABCD$ matrix. The $ABCD$ parameters and S-parameters are presented as shown in figure 3.4.



$$\begin{pmatrix} V_{in}^{ant} \\ I_{in} \end{pmatrix} = \begin{pmatrix} A & B \\ C & D \end{pmatrix} \begin{pmatrix} V_{out} \\ I_{out} \end{pmatrix}$$

$$V_{in}^{ant} = AV_{out} + BI_{out}$$

$$I_{in} = CV_{out} + DI_{out}$$

$$\begin{pmatrix} b_1 \\ b_2 \end{pmatrix} = \begin{pmatrix} S_{11} & S_{12} \\ S_{21} & S_{22} \end{pmatrix} \begin{pmatrix} a_1 \\ a_2 \end{pmatrix}$$

$$b_1 = S_{11}a_1 + S_{12}a_2$$

$$b_2 = S_{21}a_1 + S_{22}a_2$$

Figure 3.4 Definitions of $ABCD$ parameters and S-parameters.

The expression in equation (3.16), can be used to simulate the performance of the antenna system for the transmission of any signal, provided that S_{21} is known for each frequency. This expression is general and valid in near-field region as well.

$$\frac{V_{out}}{V_{in}} = H(\omega, \theta, \varphi, R) = \frac{S_{21}}{2} \quad (3.16)$$

As seen in equation (3.16), the antenna system transfer function, can be directly described by S_{21} or S_{12} of a transmitting-receiving antenna system, where the characteristic impedance has an impact on the transmitting and receiving antenna transfer functions.

3.2.6 Radiated fields regions

When RF power is delivered to an antenna, two fields evolve. One is an induction field (or near field), which is associated with the stored energy. The other is the radiated field. At the antenna, the intensities of these fields are large and are proportional to the amount of RF power delivered to the antenna. The radiated field is divided in three distinctive regions: reactive near field, radiating near field, far field [13, 14]. For antennas physically larger than a half-wavelength of the radiation they emit, the near and far fields are defined in terms of the Fraunhofer distance by the following:

$$R_1 = 0.62\sqrt{D^3/\lambda} \quad (3.17)$$

$$R_2 = 2D^2/\lambda \quad (3.18)$$

where D is the largest dimension of the antenna and λ is the wavelength. The field regions of the antenna are presented in figure 3.5.

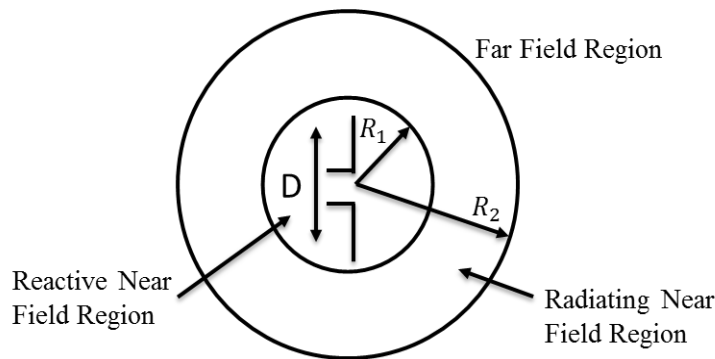


Figure 3.5 Field regions for antennas equal to one-half wavelength or shorter than one-half wavelength.

In the near field, the relationship between E and H becomes very complex. While electromagnetic waves are usually characterized by a single polarization type (horizontal, vertical, circular, or elliptical) all four polarization types can be present in the near field. The near field is a region in which there are strong inductive and capacitive effects from the currents and charges in the antenna that cause electromagnetic components that do not behave like far-field radiation. These effects decrease in power far more quickly with distance than do the far-field radiation effects.

Below we present the general knowledge we can infer from Maxwell's equations regarding the energy and power dynamics surrounding arbitrary antenna systems. we examine these fields and present the behavior of a small (short) dipole antenna ($\lambda/50 < l \leq \lambda/10$).The \vec{E} and \vec{H} fields produced by a small

dipole antenna of current $\bar{I} = \hat{a}_z I$ (where I is constant) and length l , located at origin of the coordinate system, are expressed by the following equations [1-3]:

$$\bar{E}(\bar{r}) = \hat{a}_r E_r + \hat{a}_\theta E_\theta \quad [V/m] \quad \bar{H}(\bar{r}) = \hat{a}_\phi H_\phi \quad (3.19)$$

where

$$H_\phi = -k^2 \frac{I_0 l \sin\theta}{8\pi} \left[\frac{1}{jkr} + \frac{1}{(jkr)^2} \right] e^{-jkr} \quad [A/m] \quad (3.20)$$

$$E_r = -k^2 \eta \frac{I_0 l \cos\theta}{4\pi} \left[\frac{1}{(jkr)^2} + \frac{1}{(jkr)^3} \right] e^{-jkr} \quad (3.21)$$

and

$$E_\theta = -k^2 \eta \frac{I_0 l \sin\theta}{8\pi} \left[\frac{1}{(jkr)} + \frac{1}{(jkr)^2} + \frac{1}{(jkr)^3} \right] e^{-jkr} \quad (3.22)$$

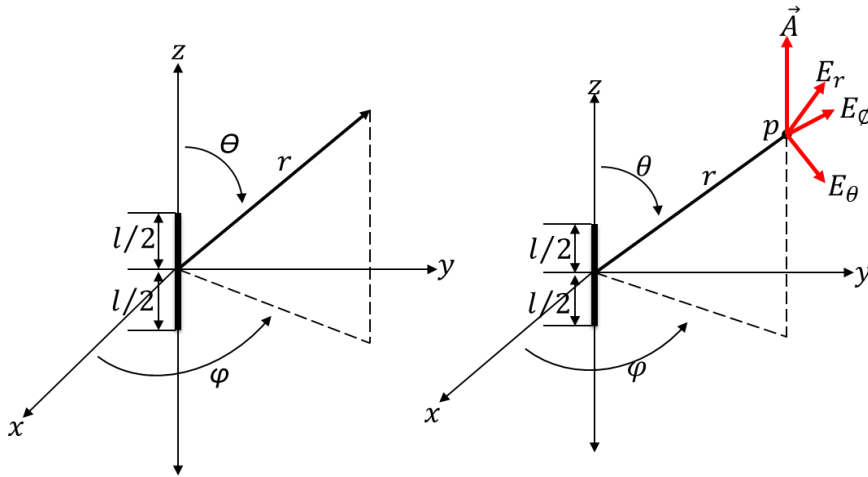


Figure 3.6 Geometrical arrangement of a dipole antenna (left) and electric field orientation (right). The charges oscillate around the origin along the z axis with infinitesimal amplitude. The vector potential at any point is parallel to the z axis, and oscillates at the same frequency as the dipole, with a phase difference and amplitude depending on the distance from the origin.

where η is the intrinsic impedance ($377 = 120\pi$ ohms for free space). The distance $r = \lambda/2\pi$ (or $kr = 1$) is referred to as radian distance and k is referred to as wavenumber. The properties of \bar{E} and \bar{H} fields in (3.19-3.22) are quite different depending if we observe them electrically close or electrically far from the dipole antenna. Figure 3.6 shows the geometrical arrangement of a dipole antenna and electric field orientation, where the dipole is positioned symmetrically around the origin with its direction along the z -axis. The average current on the small or

short dipole is one half of that of the equivalent infinitesimal dipole. Therefore, the fields produced by the short dipole are exactly one half of those produced by an equivalent infinitesimal dipole.

3.2.6.1 Near-Field Region ($kr \ll 1$)

In a region where $kr \ll 1$ or $2\pi r \ll \lambda$, the $1/(jkr)^2$ term can be neglected with respect to the $1/(jkr)^3$ term in (3.21) and the $1/jkr$ and $1/(jkr)^2$ terms can be neglected with respect to the $1/(jkr)^3$ term in (3.22). Additionally, for both (3.20) and (3.21) equations, we employ the series expansion:

$$e^{-jkr} = 1 - jkr - \frac{(kr)^2}{2} - \dots \quad (3.23)$$

The equations (3.22)-(3.23) can be simplified and approximated by:

$$E_r = -j\eta \frac{I_0 l \cos\theta}{4\pi kr^3} e^{-jkr} \quad (3.24)$$

Following a similar process for E_θ in (3.23) we find that:

$$E_\theta = -j\eta \frac{I_0 l \sin\theta}{8\pi kr^3} e^{-jkr} \quad (3.25)$$

Keeping the dominant term in (3.21) where ($kr \ll 1$) gives:

$$H_\phi = \frac{+I_0 l \sin\theta}{8\pi r^2} e^{-jkr} \quad (3.26)$$

$$E_\phi = H_r = H_\theta = 0 \quad (3.27)$$

The E-field components are in phase but they are in phase quadrature with the magnetic field component. The E-field in (3.24)-(3.27) for near field region of the small antenna has exactly the same form as that for an electric dipole:

$$\bar{E}_p = \frac{p}{4\pi\epsilon r^3} (\hat{a}_r 2\cos\theta + \hat{a}_\theta) \quad V/m \quad (3.28)$$

The condition of $kr \ll 1$ can be satisfied at moderate distances away from the antenna provided that the frequency of operation is very low. In summary, the \bar{E} and \bar{H} fields at electrically close distance $kr \ll 1$ from the small dipole antenna have the same form as the fields of the static problem (electric

dipole, static current element), but those fields simply oscillate sinusoidally with time. Thus we usually refer to (3.24)-(3.26) as the quasi-static fields.

3.2.6.2 Intermediate-field region ($kr > 1$)

Under $kr > 1$ condition, the terms that were dominant for $kr \ll 1$ condition become smaller and the two E-field components lose their in-phase property while the E_θ and H_ϕ components approach time-phase. Since their magnitude is not the same, they form a rotating vector in a plane parallel to the direction of propagation and is usually referred to as the cross field. In contrast to the $kr \ll 1$ condition the $1/(jkr)^3$ term can be neglected with respect to the $1/(jkr)^2$ term in (3.21) and the $1/(jkr)^2$ and $1/(jkr)^3$ terms can be neglected with respect to the $1/jkr$ term in (3.22). Thus we can rewrite for $kr > 1$:

$$E_r = +\eta \frac{I_0 l \cos\theta}{4\pi r^2} e^{-jkr} \quad (3.29)$$

$$E_\theta = +j\eta \frac{kI_0 l \sin\theta}{8\pi r} e^{-jkr} \quad (3.30)$$

$$H_\phi = +j \frac{kI_0 l \sin\theta}{8\pi r} e^{-jkr} \quad (3.31)$$

$$E_\phi = H_r = H_\theta = 0 \quad (3.32)$$

The total electric field is given by:

$$\vec{E}(\vec{r}) = \hat{a}_r E_r + \hat{a}_\theta E_\theta \quad \vec{H}(\vec{r}) = \hat{a}_\phi H_\phi \quad (3.33)$$

3.2.6.3 Far-Field Region ($kr \gg 1$)

In the far-field region, the situation is completely different for the \vec{E} and \vec{H} fields at distances electrically far from the antenna. Since (3.29)-(3.32) are valid, E_r will be smaller than E_θ because E_r is inversely proportional to r^2 as shown in equation (3.29) while E_θ is inversely proportional to r . In this case ($kr \gg 1$), equations (3.29) through (3.32) can be simplified as:

$$E_{\theta} = j\eta \frac{kI_0 l \sin\theta}{8\pi r} e^{-jkr} \quad (3.34)$$

$$E_r = E_{\phi} = H_r = H_{\theta} = 0 \quad (3.35)$$

$$H_{\phi} = j \frac{kI_0 l \sin\theta}{8\pi r} e^{-jkr} \quad (3.36)$$

These far zone fields of the antenna behave very differently from the near zone fields:

- because of the e^{-jkr} factor in (3.34) and (3.36), \bar{E} and \bar{H} propagate as waves in the $+\hat{a}_r$ direction (away from the dipole antenna). These are called spherical waves.
- both \bar{E} and \bar{H} components are perpendicular to the direction of propagation (\hat{a}_r) because E_r is vanishingly small with respect to the E_{θ} term.
- the electric and magnetic fields are orthogonal and their ratio is called the characteristic impedance, η :

$$\eta = \frac{E_{\theta}}{H_{\phi}} = \mu_0 c \quad (3.37)$$

where c is the light velocity in vacuum and μ_0 is the magnetic permeability of vacuum. The far fields of the dipole antenna are proportional to $1/r$ and decay in amplitude as they propagate away from the antenna. The real power radiated by the dipole antenna is one fourth of that of the infinitesimal dipole. The radiated power is given by the following expression:

$$P_{rad} = \eta \frac{\pi}{12} \left(\frac{|I_0| l}{\lambda} \right)^2 = \frac{1}{2} |I_0|^2 R_r \quad (3.38)$$

where the associated radiation resistance is:

$$R_r = \eta \frac{\pi}{6} \left(\frac{l}{\lambda} \right)^2 = 20 \pi^2 \left(\frac{l}{\lambda} \right)^2 \quad (3.39)$$

3.3 Design of compact Antipodal Vivaldi Antennas

The tapered slot antenna (TSA) is still one of the most widely used wide-band antenna. This antenna was presented at the 9th European Microwave Conference in 1979 by P. J. Gibson under the name “The Vivaldi Aerial” [17]. A new structure of tapered slot line flaring out in exponential form or linear form, also known as the ETSA or Vivaldi antenna, has been developed [17]. A Vivaldi antenna is basically a planar traveling wave antenna with interesting end-fire radiation. The Vivaldi is a very good candidate for UWB applications due to its planar structure, its highly directive patterns, low cross polarization, frequency-independent radiating property, and wide bandwidth.

There are several advantages of using directional antennas both in UWB impulse radar and communications. First of all the energy efficiency is good. While a standard omnidirectional antenna transmits the energy in all directions, a directional antenna is capable of directing most emitted power in a lobe or beam. In this way a receiving antenna can get more of the radiated energy, thus reducing the required transmission power. Previous research on Vivaldi antennas provides empirical results implying that the UWB properties and the behavior of the Vivaldi antenna appear to be one of the most attractive for UWB pulse radar systems. The Vivaldi antenna has a rather low impulse distortion compared to other UWB antennas [18- 22].

The Vivaldi antennas can be classified into three different categories [18- 23]:

- ❖ Coplanar Vivaldi Antennas (CVA) usually have wideband performance of typically two octaves. Due to their feeding transitions (micro-strip to slot-line) they produce high radiation loss and even distort radiation patterns at high frequencies. In Coplanar Vivaldi antennas the two radiating planes are on the same side of the dielectric material. The antenna can be fed by aperture coupling from the other side of dielectric substrate material.
- ❖ Antipodal Vivaldi Antennas (AVA) have much wider bandwidth ($>10:1$) due to their feeding transitions (micro-strip to parallel strip-line). In this type of Vivaldi antennas one of the layers is printed on top and the other one which is tapered in opposite direction is printed on the bottom of the dielectric substrate material.
- ❖ Balance Antipodal Vivaldi Antennas (BAVA) consists of three copper layers. A dielectric layer has been added on top of the antipodal structure and an additional metal plate just like the one in the bottom of the antenna has been printed on top of the newly added layer.

Several techniques have been used to modulate the radiation characteristics of such antennas: improvement of the lower operation frequency by Tapered Slot Edge (TSE) structures and regular slot edges structures [18-20]. Double slot Vivaldi antennas (DSVA) [21] and Dual Exponentially Tapered Slot Antennas (DE TSA) have also been developed [22]. Polarization improvement is also achieved by modified double layer TSA [23].

3.3.1 Antipodal Vivaldi Antenna geometry and design

Recently, various antennas have been developed for UWB communications [6-16]. In our case, small Antipodal Vivaldi Antennas based on elliptical curves have been designed to transmit and receive digital data streams with Manchester or Polar RZ encodings at a data rate above 1 Gbps.

Table 3.1 summarizes the comparison between the proposed antenna and antennas from literature. To fit our needs with the limited space inside the cryogenic system the proposed AVA is smaller in dimensions than the ones with antipodal configuration reported in [18- 21]. Besides we optimized it to obtain similar or better performance.

Table 3.1 Comparison of our customized AVA with some other AVA from the literature.

AVA ref.	dimension L*W (mm ²)	operating frequency (GHz)	gain (dB)
[18]	60*48	2.4 to >14 measured	3.7 - 10
[19]	42*36	3.7 to >18 measured	1.8 - 6.9
[20]	42*36	3.7 to >18 measured	-1 – 3.8
[21]	66.4*50	4 to >30 simulated	5 - 7
this work	37*21	3.6 to >12 measured	-0.5 - 4.5

The description of the design of the Antipodal Vivaldi Antenna under concern is given in [22-23]. Two AVAs fed by a 50Ω microstrip transmission line have been designed to be simulated and fabricated for wideband operation on a FR4 substrate of thickness $h = 1.6$ mm with $\epsilon_r = 4.4$ dielectric constant, and a dielectric loss tangent of $\delta = 0.02$. It is customized with a slot resonator located on the ground plane only. The distance between the ground plane edge and the connector has been shifted in order to increase the low frequency behavior.

The proposed antenna includes two main parts: feed line and radiation flares. The shape of the flares is designed in the form of elliptical curves. Other shapes can be used, such as exponential ones, but an elliptical taper yields good performance and can be easily created in most CAD tools [25]. The total size ($L \times W$) of the antenna composed of a feed line and radiation flares is 37×21 mm². The elliptical configuration presents good broadband characteristics due to the smooth transition between the radiation flares and the feeding line. It is one of the optimum curvatures [21].

The width of the feeding line to obtain a characteristic impedance $Z_0 = 50 \Omega$ equal to that of the feeding coaxial cable has been calculated to be $W_f = 3$ mm using the following equations [23]:

for $\left(\frac{W_f}{h}\right) < 1$:

$$Z_0 = \frac{60}{\sqrt{\epsilon_{eff}}} \ln \left(\frac{8h}{W_f} + \frac{W_f}{4h} \right) \quad (3.40)$$

for $\left(\frac{W_f}{h}\right) \geq 1$:

$$Z_0 = \frac{120\pi}{\sqrt{\epsilon_{eff}} \left[\frac{W_f}{h} + 1.393 + \frac{2}{3} \ln \left(\frac{W_f}{h} + 1.444 \right) \right]} \quad (3.41)$$

where

$$\epsilon_{eff} = \frac{\epsilon_r + 1}{2} + \frac{\epsilon_r - 1}{2} \left(1 + \frac{12h}{W_f} \right)^{-1/2} \quad (3.42)$$

$\epsilon_{eff} = 3.32$ in our case for $W_f = 3\text{mm}$. Theoretically the upper frequency limit of a Vivaldi Antenna is infinite, while the lower frequency limit depends mainly on the width of antenna and on the effective dielectric constant (ϵ_{eff}). The lower cutoff frequency can be calculated from [25-26]:

$$f_{min} = \frac{c}{W_p * 1.5 * \sqrt{\epsilon_r + 1}} \quad (3.43)$$

where W_p is the total width of two antenna arms of 20 mm, and c is the velocity of light in free space. The lower frequency is found to be 4.3 GHz. Figure 3.7 shows the layout of the initial AVA design, along with the simulated return loss, revealing the UWB performance on a bandwidth ranging from 4.3 to more than 12GHz. The width (W) of AVA is 21mm corresponding to the lowest frequency of operation ($f_{min} = 4.3\text{GHz}$) while the length (L) of the AVA of 37 mm corresponds to $L=0.53*\lambda$, where λ is the wavelength at 4.3GHz. The antenna is fed by a 3 mm-wide microstrip line. The optimal dimensions have been adjusted with the aid of HFSS simulation software.

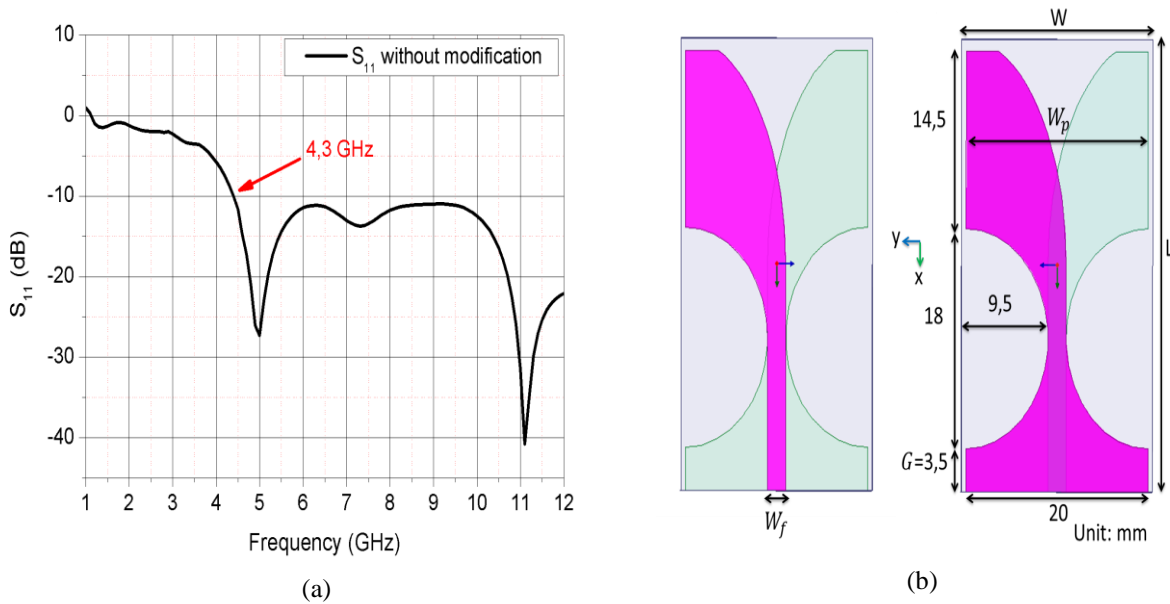


Figure 3.7 (a) Simulated return loss and (b) layout of the AVA. Total size ($L*W$) is $37*21 \text{ mm}^2$ on FR4 substrate thickness with $h=1.6\text{mm}$, $W_f=3\text{mm}$, and $W_p = 20\text{mm}$.

3.3.2 Results and analysis

In a second step, the antenna has been modified by etching a slot resonator on the ground plane only and by shifting the ground plane input port by $S = 1$ mm, as shown in Figure 3.8. As a result, the low-end cutoff frequency of the antenna has been significantly reduced by 20% from 4.3 to 3.6 GHz. The width of the feed line has also been reduced to $W_f = 2$ mm to keep a good match with the same antenna size. The modification of the ground plane line and the addition of a slot to the antenna are the main significant differences compared to other Vivaldi antennas. The slot technique has been used for lengthening the excited surface current on the radiation elements and for improving the antenna bandwidth [25, 27]. Adjusting the length of the slot allows controlling the resonance frequency.

The slot resonator located on the ground plane only, and the shift of the ground plane edge are presented in Figure 3.8. The shift of ground plane line and the slot are introduced to improve the low frequency performance. As shown in the figure, the return loss of the antenna is optimized to be below -10 dB over the frequency band from 3.6 GHz to more than 12GHz to satisfy the requirement of the Ultra-wideband (UWB) technology.

Simulation results show that the antenna operates in the frequency band from 4.3 GHz to more than 12GHz before inserting the slot while, after inserting the slot on the ground plane, the bandwidth ranges from 3.6 GHz to more than 12 GHz. The antenna is matched to a 50-ohms line giving a good match over the ultra-wideband. The influences of the presence of the slot and of the shift of the ground plane are described below.

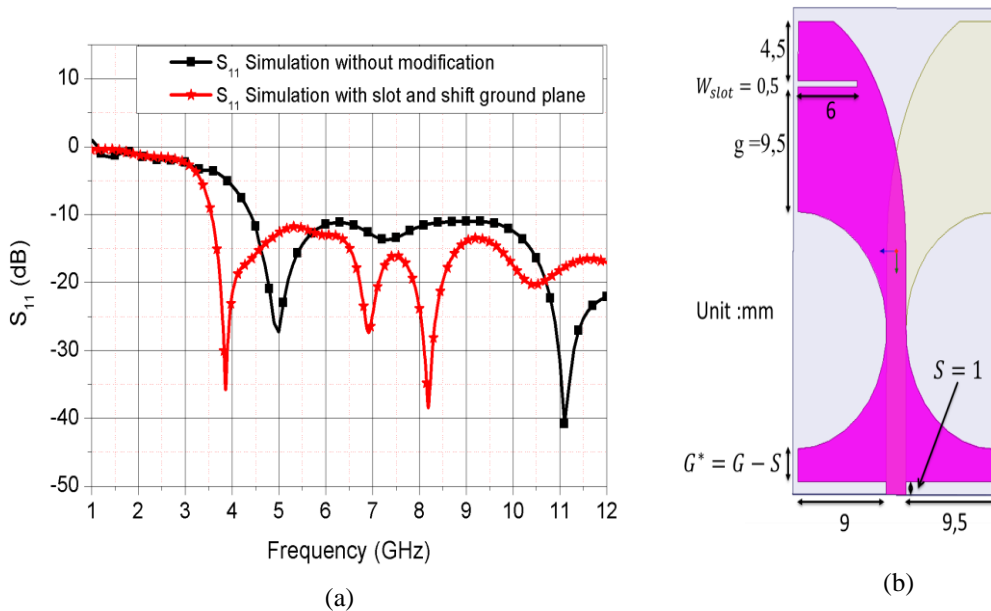


Figure 3.8 (a) Simulated return loss and (b) layout of AVA. Total size ($L * W$) is $37 * 21\text{mm}^2$ with FR4 substrate thickness $h = 1.6\text{mm}$, $W_f = 2\text{mm}$, and $W_p = 20\text{mm}$. The ground plane is shifted by $S = 1$ mm.

3.3.2.1 Effect of the ground plane slot

The length of the slot has been designed for a center frequency of 7 GHz for our application. The corresponding guided wavelength λ_g in presence of the substrate is calculated from the following equation, where $\epsilon_{eff} = 3.22$ is obtained from equation (3.42) for $W_f = 2mm$:

$$\lambda_g = \frac{\lambda_0}{\sqrt{\epsilon_{eff}}} \quad , \quad \lambda_0 = \frac{c}{f} \quad (3.45)$$

The length of the slot has been taken equal to a quarter of the guided wavelength $\lambda_g = 23.9 mm$. The slot of 0.5 mm width and 6mm length ($0.25\lambda_g$) was etched on the ground plane at a suitable position. As a result the S_{11} return loss behavior is improved.

The comparison of return loss between the two Antipodal Vivaldi Antennas, with and without the slot, is presented in figure 3.9 (a). S_{11} is lower than -10 dB from 3.6 to more than 12 GHz in presence of the slot. In order to understand the behavior of the slot on ground plane, especially in the frequencies between 5.5GHz to 9.5GHz where a resonance seems to appear, maps of the current distribution over the antennas with and without the slot on the ground plane have been simulated at 7 GHz and are given in figure 3.9 (b).

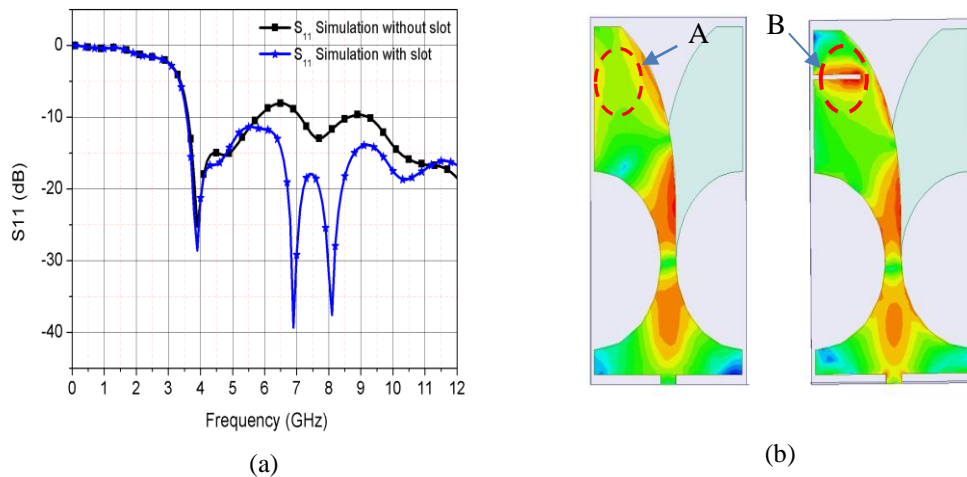


Figure 3.9 (a) Return loss performance of the proposed antenna with and without the slot. (b) Surface current distribution of the proposed AVA at 7GHz with and without the slot.

As the figure reveals, the surface current of antenna without slot in region A is very small at 7GHz. It is demonstrated that most of the input energy is reflected and cannot be radiated. Thus, the return loss of antenna without slot shown in figure 3.9 (a) is high from 5.5 GHz to 9.5 GHz.

On the other hand, by etching the slot, significant current is observed about the edge of the slot in region B (see figure 3.9 (b)). This indicates that the effective length of the current path on the antenna is increased by the modification. The insertion of the slot in the ground plane causes an increase of the bandwidth with a good impedance match in the 5.84-9.38 GHz frequency range, as shown in figure 3.9

(a).The design of the proposed antenna allows for some degrees of freedom to provide some sort of flexibility in the antenna design.

There are several parameters in the design which have a significant effect on the performance of the antenna, e.g., the width of slot, the length of slot, the position of slot. Figures 3.10 and 3.11 show the simulated return losses of four various cases for different lengths, widths, and positions of the slot, etched either only on the ground plane or on both metallic layers.

When the slot is etched on both sides of the antenna as shown in figure 3.10, the lower resonant mode at about 3.8 GHz is not modified while the good impedance match found in figure 3.9 (a) with only one slot in the 5.84-9.38 GHz bandwidth is not as good with two slots on each side. Nevertheless there is an impedance match improvement, but for a different length of slot (7 mm instead of 6mm) likely due to a different lengthening of the current path, and not as good as in figure 3.9 (a), even if other parameters, like the position of the slots, are varied. Effects of the width and length of slot in the antenna can be seen in figure 3.10.

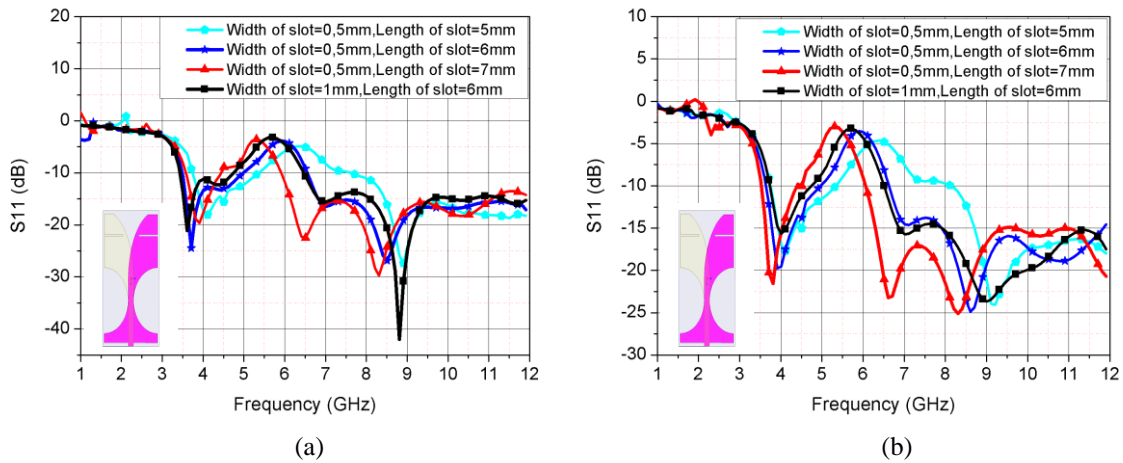


Figure 3.10 Return loss performance of the proposed antenna for different widths, lengths, and positions of slot etched on both sides of the antenna. Position of slot: (a) $g=9.5$ (b) $g=8.5$.

Figure 3.11 (a), shows the variations of S_{11} for different widths of slot etched only on the ground plane from 0.5mm to 2mm for a fixed length of slot of 6mm. One sees that the impedance match is not highly sensitive to the S_{11} parameter while a stronger dependence is observed when varying the length of the slot from 3mm to 7mm for a fixed width of slot as shown in figure 3.11 (b). The effect of the position of the slot for fixed slot length and width is shown in figure 3.11 (c) and needs to be taken into account during the design phase.

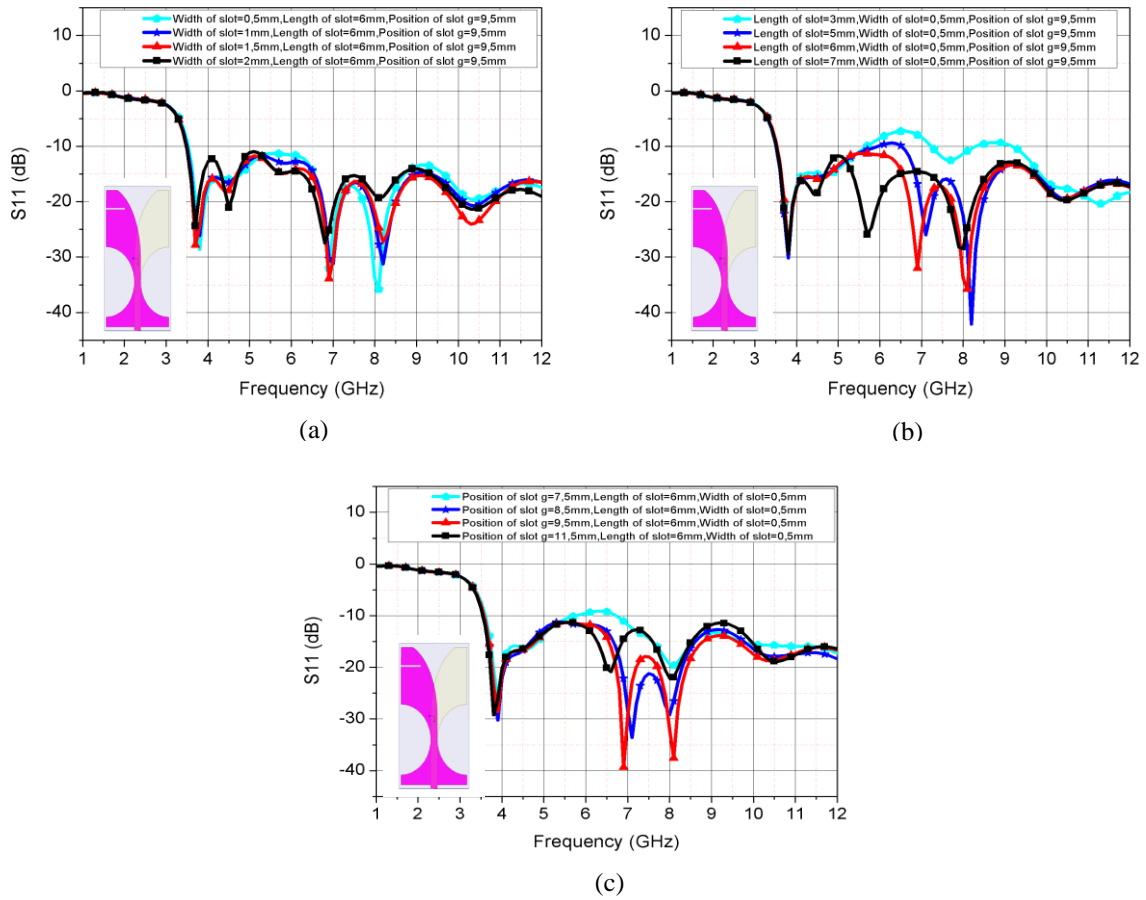


Figure 3.11 Return loss simulations of the proposed antenna for different widths, lengths, and positions of the slot etched on the ground plane only. (a) Slot length = 6mm, position of slot $g=9.5$ mm, slot widths: 0.5, 1, 1.5, and 2 mm. (b) Slot width = 0.5mm, position of slot $g=9.5$ mm, slot lengths: 3, 5, 6, and 7 mm. (c) slot length = 6mm, width of slot = 0.5mm, positions of slot: 7.5, 8.5, 9.5, and 11.5mm.

3.3.2.2 Effect of the shift of the ground plane edge

The layout of the ground plane shifted farther from the connector point is shown in figure 3.12(a). This modification, combined with the presence of the ground plane slot, leads to a remarkable efficiency in the low frequency part of the spectrum, without affecting the original antenna length.

The simulated return loss performance for a shift $S=0, 1, 2, 3$ mm is shown in figure 3.12(b, c), respectively for an antenna with and without ground plane slot. The low-end operating frequency decreases from 4.28 GHz to 3.52 GHz, on the condition that S_{11} is lower than -10 dB.

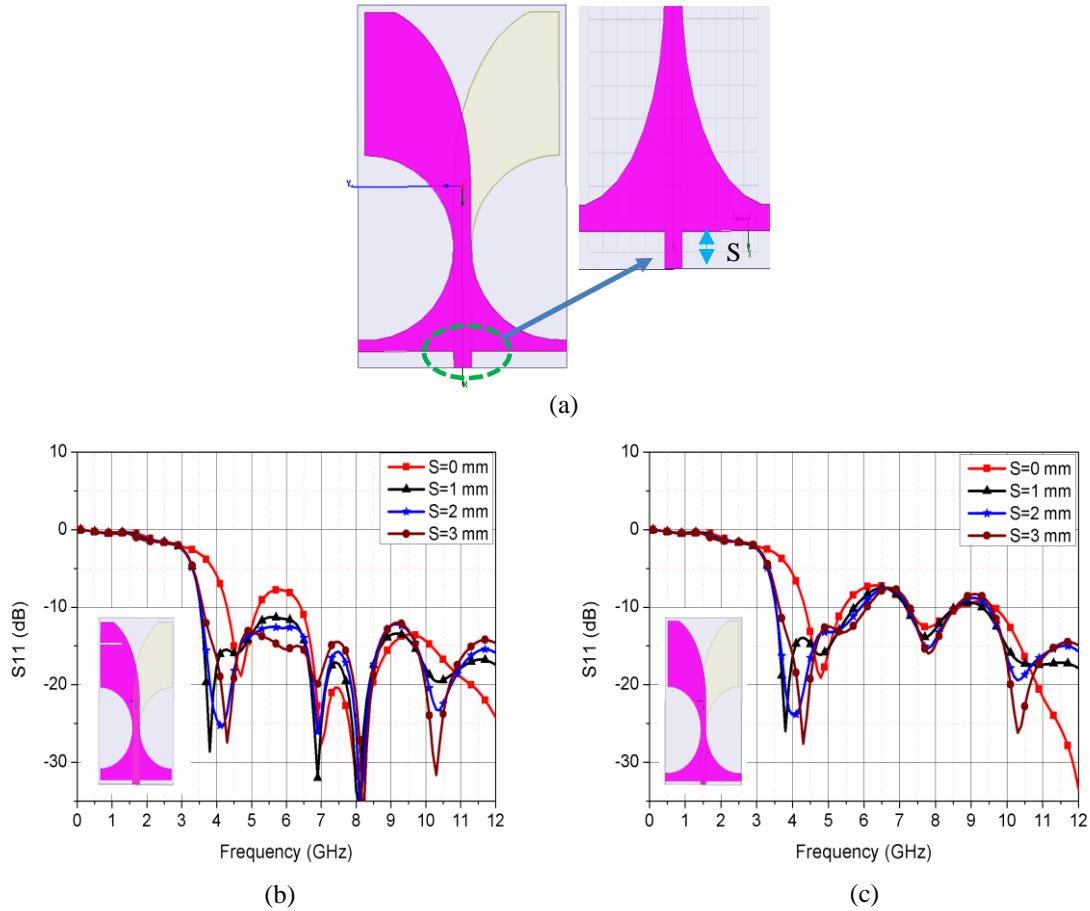


Figure 3.12 Return loss with a ground plane shift of $S=0, 1, 2, 3$ mm. (a) layout of the shifted ground plane (S) with an extended input microstrip line. (b) S_{11} with ground plane slot. (c) S_{11} without ground plane slot.

As shown in the figure, the shift of the ground plane edge along with the presence of a ground plane slot, helps the antenna to be miniaturized by a ratio of 19.5 %. Figure 3.12 (b) shows that the low-end cut-off frequency of the AVA for $S_{11} \leq -10$ dB at $S=0$ mm (without shift) is 4.28 GHz, while at $S=1, 2, 3$ mm ($G^* = G - S$) it is equal to 3.53 GHz. Additional resonances can be observed around the lower frequency part of the working band for several values of S . The AVA structure with $S=1$ mm and a ground plane slot is the best combination to miniaturize the electrical size of the antenna.

3.3.2.3 Voltage Standing Wave Ratio (VSWR) and antenna gain

The VSWR provides an estimate of an antenna's match with its environment. It is required that it stay below 2 across the entire UWB spectrum, from 3.1 to 10.6 GHz, to insure proper match. Simulation results presented in figure 3.13 clearly show that the VSWR is less than 1.7 over the frequency range from 3.6 GHz to more than 12 GHz for this antenna.

When the antenna is used for wideband applications, the impedance mismatch must be taken into account for defining its characteristics, especially when calculating the antenna gain. Figure 3.13 shows the simulated peak gain of the proposed antenna versus frequency. As can be seen, the peak gain varies from -0.5 dBi to 4.5 dBi over the frequency range of operation, which is satisfactory for our application.

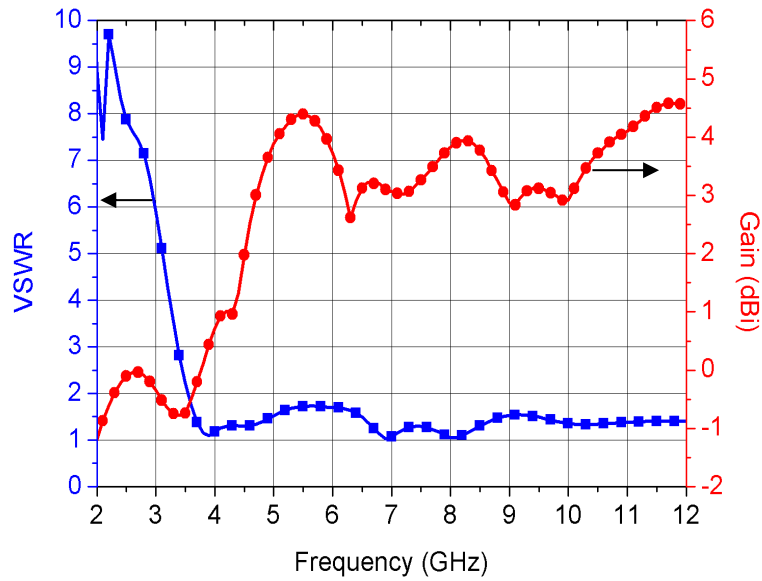


Figure 3.13 Simulated VSWR and peak gain versus frequency for the AVA with a slot resonator and a grounded plane shifted by 1mm.

3.3.2.4 Radiation patterns characteristics of antenna

The simulated and measured radiation patterns of the proposed antenna in the two principal x-y and x-z planes (see geometry in Figure 3.7.b) are presented in Figure 3.14 at the resonant frequencies of 3.5, 7, 9 and 11 GHz. The radiation patterns were measured inside an anechoic chamber using an HP 8720ES Vector Network Analyzer (VNA).

The AVA acted as a receiver and a horn antenna connected to the second port of the VNA acted as the transmitter. The largest dimension of the horn antenna is 22 cm, hence the far-field zone of this horn antenna is valid from 30 cm for the AVA frequency band. The proposed AVA was located at a distance of 250 cm from the horn antenna so that the far-field condition is ensured.

In figure 3.14, it can be seen that the gain in x-y plane (E-plane) and x-z plane (H-plane) exhibits nearly omnidirectional patterns at $\phi=0$ and bidirectional patterns at $\phi=90^\circ$. As shown in the figure, the AVA has end-fire characteristics with the main lobe in the axial direction (x-direction). Also, it can be observed that there is a significant difference between the simulated radiation patterns and the measured ones. Due to the metallic part of the reflecting plane the radiation in the back side goes back towards the front side and more energy is radiated in this orientation.

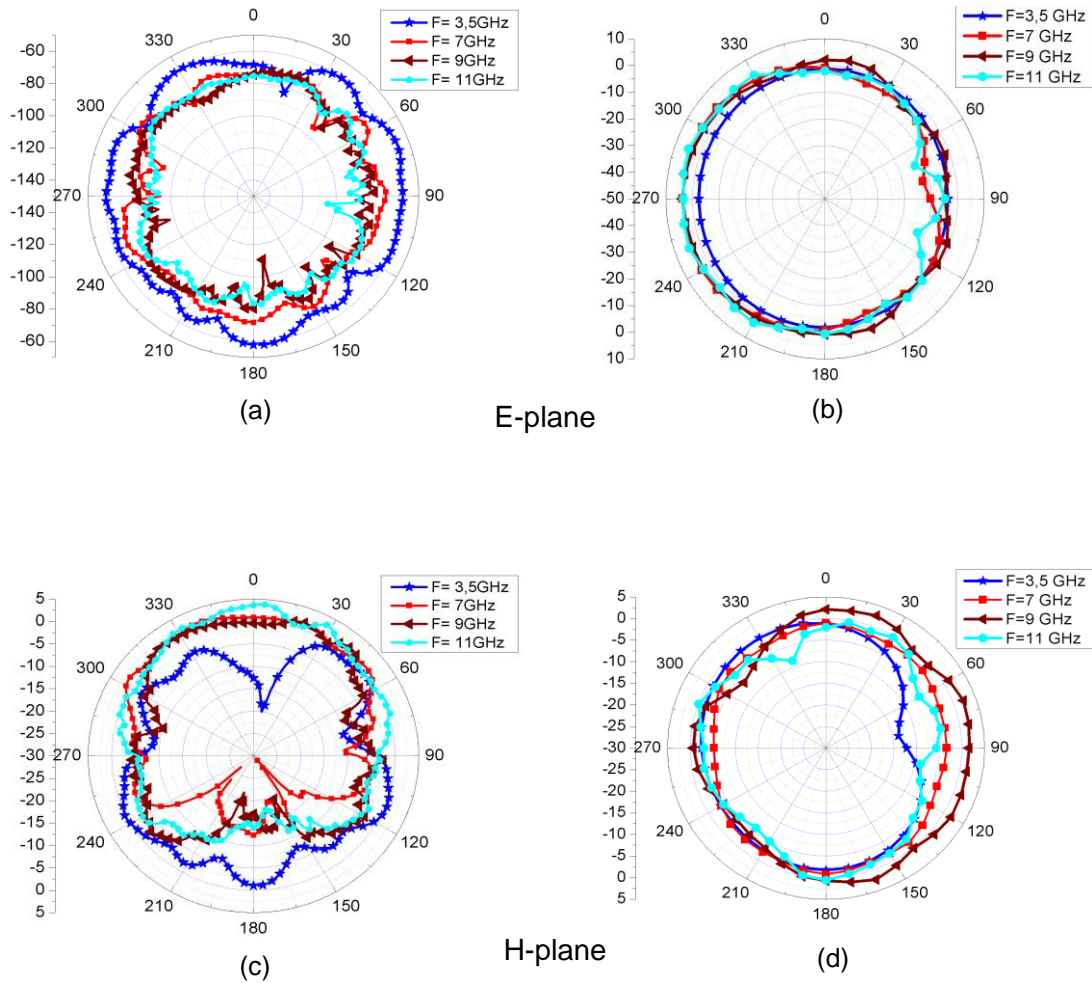


Figure 3.14 Simulated and measured radiation patterns of the AVA at 3.5, 7, 9, and 11 GHz. (a) Measured radiation patterns in E-plane. (b) Simulated radiation patterns in E-plane. (c) Measured radiation patterns in H-plane. (d) Simulated radiation patterns in H-plane.

3.3.2.5 Surface current distributions of antenna

The simulated surface current distributions of the proposed antenna carried out by HFSS at the same frequencies are given in figure 3.15. It can be seen that the current distributions at the four resonant frequencies are different.

For the first resonant frequency of 3.5 GHz the surface current is mainly concentrated on the microstrip feed line while resonant frequencies at 7, 9 and 11 GHz are concentrated at the microstrip line feed and radiation side.

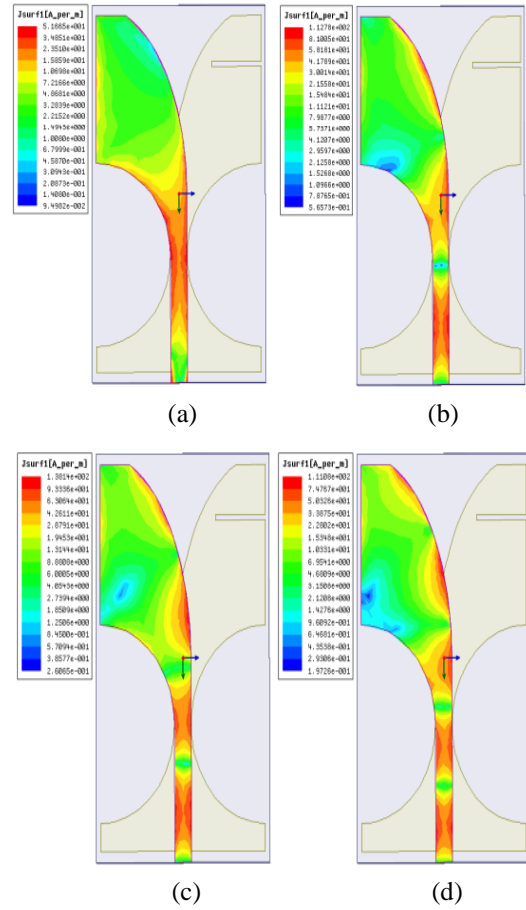


Figure 3.15 Simulations of surface current distributions of the AVA. (a) 3.5GHz. (b) 7GHz. (c) 9 GHz. (d) 11GHz.

3.3.2.6 Simulated and measured return loss

The measured and simulated S_{11} of the proposed antenna are shown in figure 3.16. Measurements were carried out with a 37369A Anritsu Vector Network Analyzer. It can be observed that both simulated and measured S_{11} are lower than -10dB from 3.6 to more than 12 GHz. The comparison of simulated results with measurements shows a 2.2% shift in frequency observed for the low resonant frequency (3.6 GHz for simulation vs. 3.68 GHz for measurements). The difference is mainly caused by slight size shifts during fabrication and numerical errors. Also the connection between the printed circuit board and the SMA connector is not ideal. The photograph of the fabricated antenna is shown in figure 3.17.

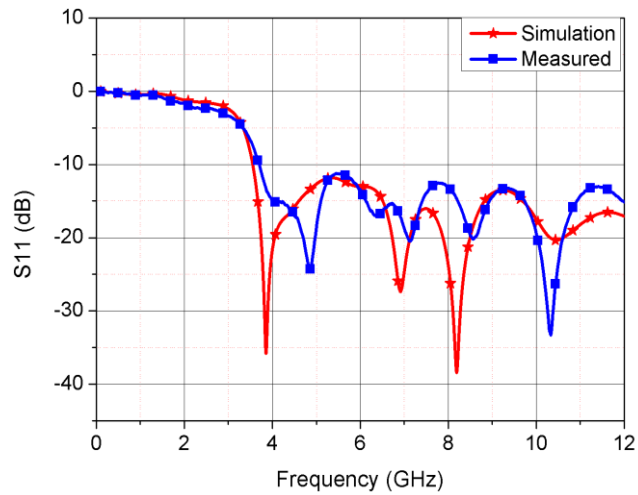


Figure 3.16 Comparison of simulated and measured return loss of AVA.

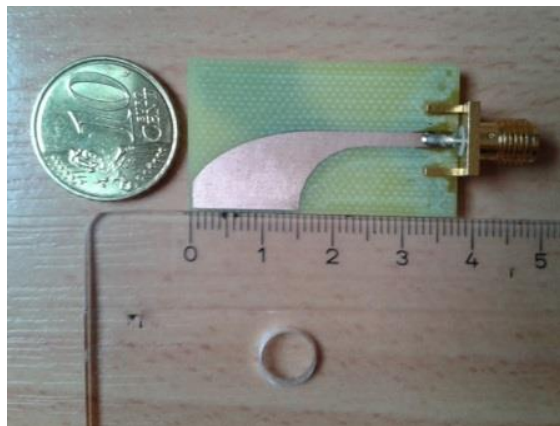
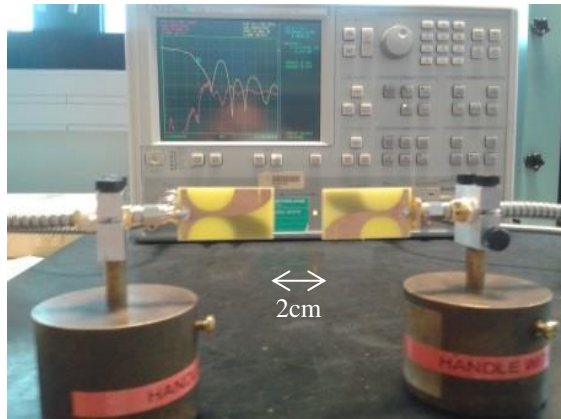


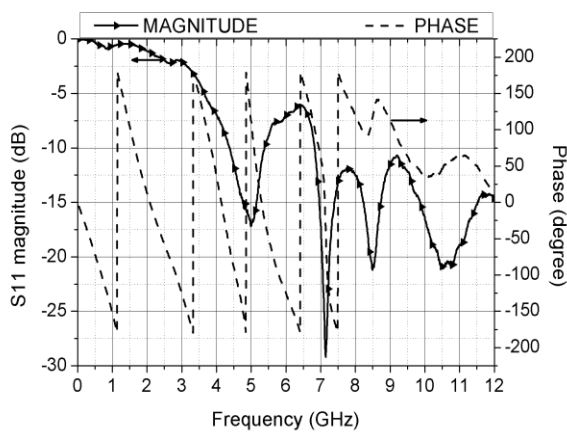
Figure 3.17 Photograph of the fabricated AVA.

3.3.2.7 Experimental characteristic of the transfer function between two identical AVAs

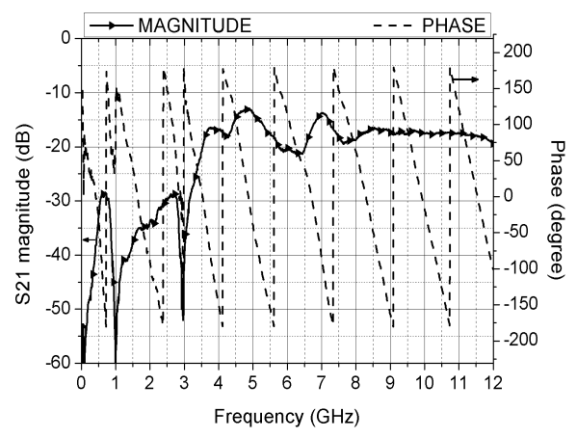
The measured transfer function at room temperature at boresight ($\theta = 0^\circ, \varphi = 0^\circ$) for two identical AVA pointing at each other with a distance $R=2$ cm is shown in figure 3.18(a). The S-parameters of the AVA were measured by an Agilent 37369A vector network analyzer. The frequency range is from 40MHz to 12 GHz with a step of 7,475MHz. A linear phase and flat amplitude characteristics are essential for a good UWB antenna.



(a)



(b)



(c)

Figure 3.18 Measured S-parameters with two AVA distance from $R=2\text{cm}$ placed in aligned configuration. (a) Setup of two AVA (b) Magnitude and phase of S_{11} . (c) Magnitude and phase of S_{21} .

The measured S-parameters amplitude and phase of AVA are shown in figure 3.18(b, c). A good linear phase response is achieved the amplitude of the transfer function is relatively flat from 3.52-12GHz.

3.3.2.8 Extension of the low frequency performance of AVAs

The broadband range can be improved by extending the AVA size in order to provide a lower end frequency. A compact Antipodal Vivaldi Antenna (AVA) with a reduced size of 50 mm x 30 mm has been designed, simulated and fabricated in order to improve the transmission of multi-channel baseband signals over a short distance of a few millimeters between the cryogenic stage and room temperature electronics. HFSS simulations show a voltage standing wave ratio lower than 2 and a peak gain in the 0-6 dB range over the 2.5-12 GHz frequency band.

The antenna has been designed for a broadband range from 2.5 GHz to more than 12GHz with an input impedance $Z_0=50\ \Omega$, equal to the impedance of the feeding coaxial cable. Dimensions of the antenna

have been optimized with the HFSS software. The antenna is fed by a microstrip line with a width of 2.5 mm. To increase the low frequency performances, a slot has been added on the ground plane at a suitable position and a shift of the ground plane edge from the input connector was realized, as was done for the previous antennas.

Figure 3.19 (a) presents the simulated and measured reflection coefficient versus frequency of the larger AVA, along with the geometrical configuration.

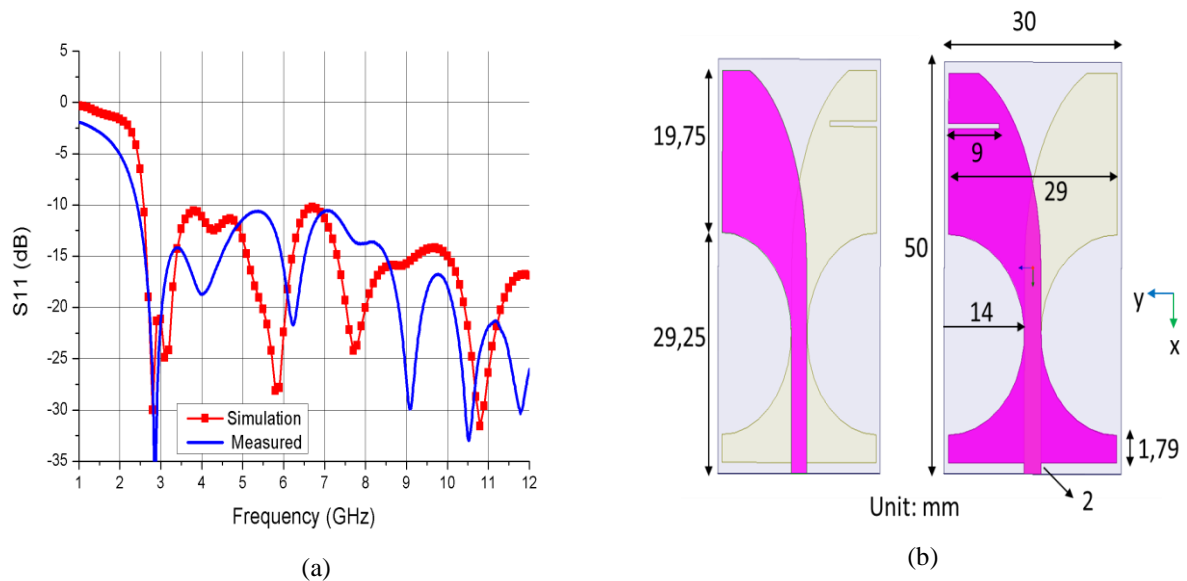


Figure 3.19 Measured, simulated return loss and schematic of AVA. Total size is $50 \times 30 \text{ mm}^2$ with FR4 substrate thickness $h=1.6 \text{ mm}$, $W_f = 2.5 \text{ mm}$. (a) Measured and simulated return loss versus frequency. (b) Schematic of AVA with slot on ground plane and shifted ground plane edge.

We observe a slight shift for the low resonant frequency (2.59 GHz for simulation vs. 2.43 GHz for measurement). The measured and simulated resonance frequencies above 5 GHz are different which may be due to slight geometrical differences associated to the soldering of the input connector, to the fabrication of the antenna and to reflections in the near environment of the antenna during measurements. The characteristics of this AVA and the short-distance configuration simulations and measurements are presented and discussed in appendix B.

3.4 Improvement of radiation characteristics by using Tapered Slot Edge (TSE)

A novel Tapered Slot Edge (TSE) structure AVA has also been studied to improve the design of a planar printed AVA. The proposed modified structure has the capacity to extend the low-end bandwidth limitation. In addition, the antenna gain and directivity of TSE structure Vivaldi antenna has been significantly improved when compared with an AVA of the same size when etched with one slot on ground plane and with shifted ground plane edge. The tapered slot edge structure is still one of the most widely used solution for wideband antennas. The TSE was first proposed to reduce the low-end cutoff frequency while keeping the dimensions of the antenna unchanged [28- 35].

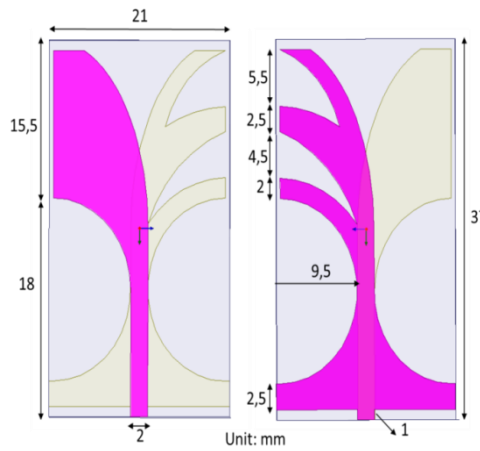


Figure 3.20 Schematic of the AVA with TSE on ground plane only: Top view (Left). Bottom view (Right).

The geometry of the TSE AVA is shown in figure 3.20. This antenna consists of an AVA with TSE structure subtracted from the ground plane with shifted ground plane edge. The total substrate size of the antenna is $37 \times 21 \text{ mm}^2$. The antenna is designed on a low-cost FR4 substrate of thickness $h=1.6 \text{ mm}$ with $\epsilon_r=4.4$ dielectric constant, and a dielectric loss tangent of $\delta=0.02$. The port width of the micro-strip feeding line is fixed to 2 mm to achieve 50Ω characteristic impedance.

3.4.1 Results and discussion

In order to validate the design of the TSE AVA antenna, two antenna prototypes have been fabricated and tested. A 50Ω SMA connector was used to feed the antennas. The fabricated antenna was measured using an Agilent 37369A programmable Network Analyzer. Simulations were carried out using HFSS. The x-z plane and x-y plane (see figure 3.23) represent the H-plane and E-plane respectively.

3.4.1.1 Return loss performance of the antenna with and without TSE

The effect of the etched TSE structure on input reflection coefficient is shown in figure 3.21. As one can see from figure 3.21, a new resonance appears around 3.4 GHz in the low frequency region when the TSE structure is added. The shift of the ground plane and the addition of a TSE to the antenna are the main significant differences compared to other Vivaldi antennas. The introduction of the TSE structure with shifted ground plane significantly improves the impedance matching at low frequencies. The lower-end $S_{11} < -10$ dB bandwidth limitation is shifted to 3.4 GHz value. This is due to the increase of the effective current path by adding the TSE structure.

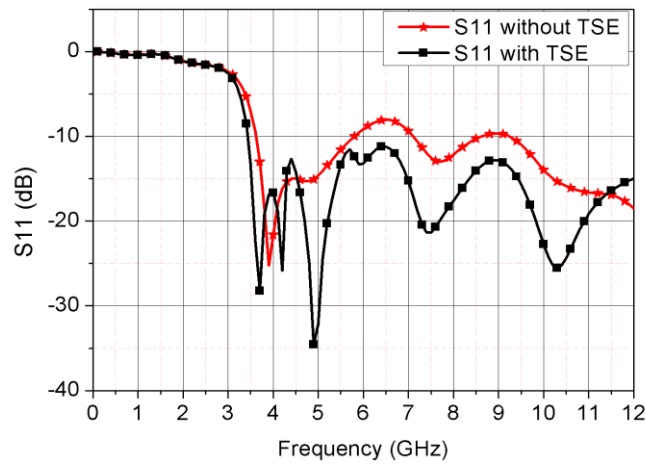


Figure 3.21 Simulated return loss of AVA with and without TSE on ground plane only and with shifted ground plane.

3.4.1.2 Voltage Standing Wave Ratio (VSWR) of the AVA with TSE

The simulated and measured results are presented in figure 3.22, clearly showing that the VSWR is less than 2 over the frequency range from 3.4 GHz to 12 GHz.

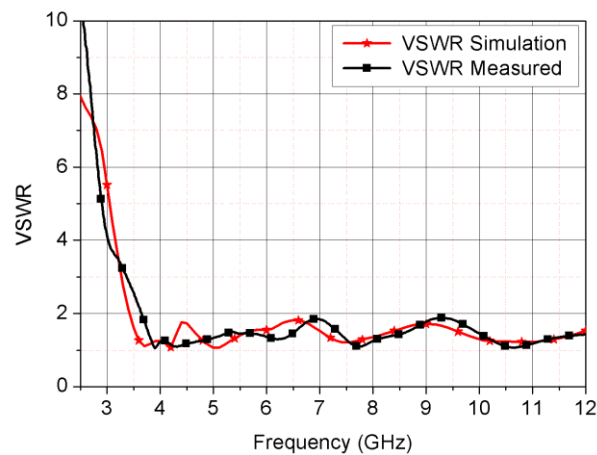


Figure 3.22 Simulated and measured VSWR of AVA with a TSE structure.

3.4.1.3 Radiation patterns characteristics of the AVA with TSE

Figures 3.23 and 3.24, show the radiation characteristics for the AVA (with TSE). Both E-plane (x-y plane) and H-plane (x-z plane) radiation patterns have been simulated using HFSS and measured in an anechoic chamber at four resonant frequencies 3.5, 7, 9, and 11 GHz.

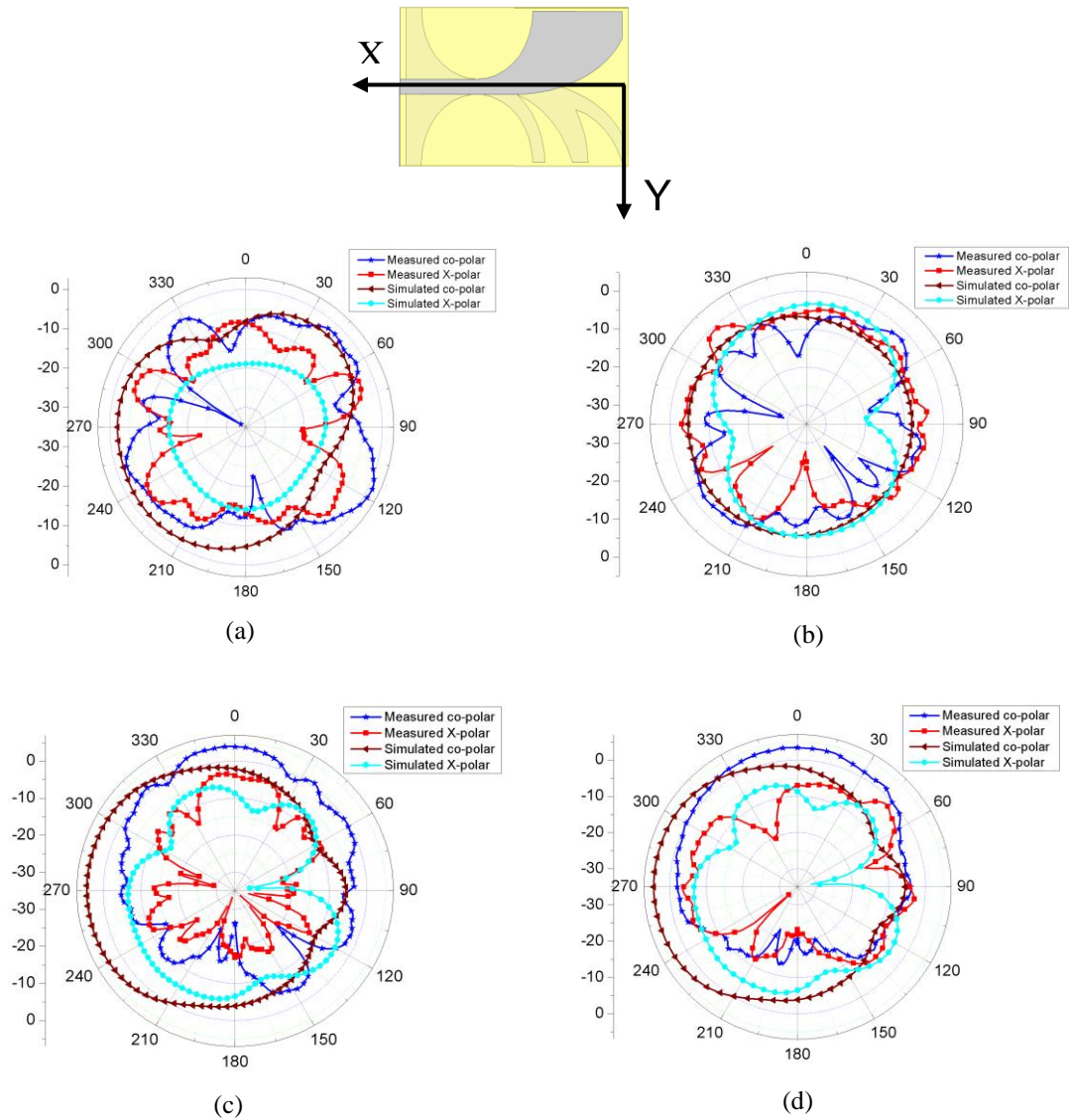


Figure 3.23 Simulated and measured radiation patterns of AVA with TSE structure in E-plane (x-y) and H-plane (x-z) at 3.5 and 7 GHz. (a) H-plane at 3.5 GHz. (b) E-plane at 3.5 GHz. (c) H-plane at 7 GHz. (d) E-plane at 7 GHz.

From the measured results, the antenna has an omni-direction radiational pattern in H-plane at lower frequencies (3.5 GHz in figure 3.24) and near omni-directional at higher frequencies (7, 9 and 11 GHz)

with good agreement with simulations. The measured E-plane radiation patterns agree with the simulations especially at higher frequencies (9 and 11 GHz) while the agreement is not as good with the H-plane patterns at lower frequencies (3.5 and 7 GHz).

There are some ripples and discrepancies in the measured radiation patterns which may be due to sensitivity and accuracy of the measuring devices at lower frequencies in addition to the effect of the SMA feed connector soldering.

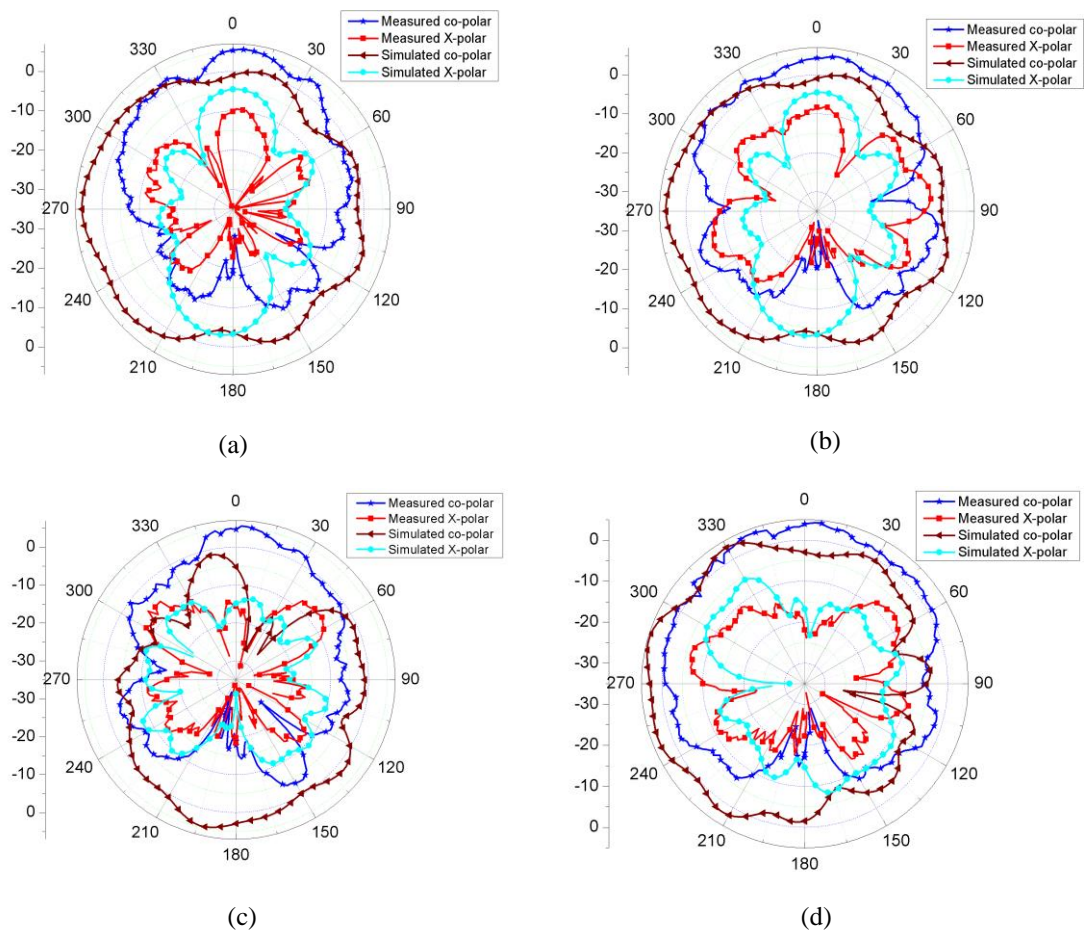
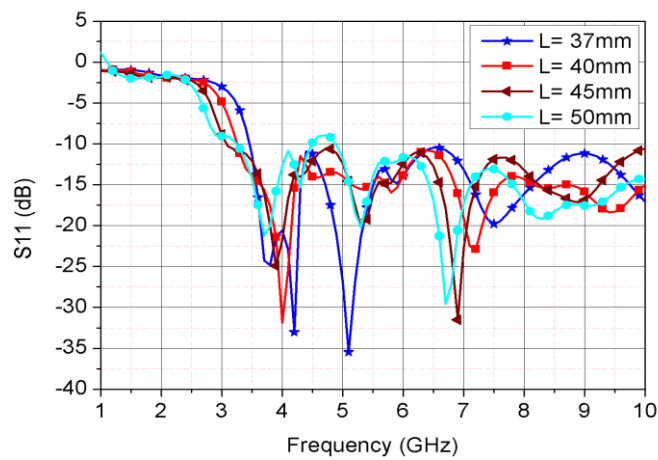


Figure 3.24 Simulated and Measured radiation patterns of AVA (TSE structure) in E-plane (x-y) and H-plane (x-z) at 9 and 11 GHz. (a) H-plane at 9 GHz. (b) E-plane at 9 GHz. (c) H-plane at 11 GHz. (d) E-plane at 11 GHz.

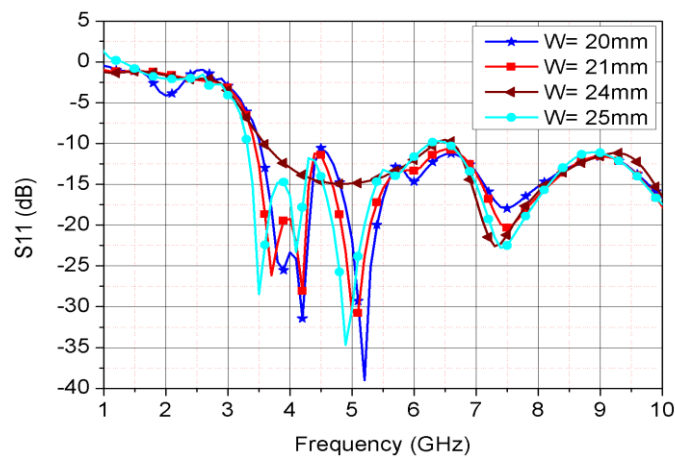
3.4.1.4 Effect of substrate width and length

The performance of the antenna is affected by several key parameters. Therefore, their effects including the width and length of the substrate are simulated as shown in figure 3.25.

Figure 3.25 (a) shows the simulated return losses when the length of the substrate varies for a fixed width of 21mm. Shift to lower frequency is found as the substrate length is increased. This may be due to the fact that the length of the substrate contributes to the resonant frequency of the antenna. Figure 3.25 (b) shows the simulated return losses for different widths of substrate and a fixed length of 37mm. It is observed that return losses shift to lower frequency when the substrate width is increased. This is attributed to the fact that the width of the substrate contributes to the resonant frequency of the antenna.



(a)



(b)

Figure 3.25 Simulated return loss of the AVA for different widths and lengths of the substrate. (a) Change of length with fixed width of 21mm. (b) Change of width with fixed length of 37mm.

3.4.1.5 Measured and simulated gains

The simulated and measured gain variations with frequency of the designed AVA with TSE are shown in figure 3.26. It can be seen that experimental measurements are in good agreement with simulated results when a TSE structure is added on the ground plane. Within the operating frequency range 5.5-12 GHz, the simulated gain with TSE structure on ground plane varies between 4.27 and 5.35 dBi with maximum gain at 8.5 GHz while the simulated gain without TSE structure on ground plane varies between 4.04 and 3.34 dBi with a maximum gain of 5.25 dBi at 8.5 GHz. The simulated and measured gains with TSE structure increase with the frequency over the whole operating band, while the simulated gain without TSE structure decreases with frequency over the 8.5 to 12 GHz band. The measured maximum gain is obtained at the frequency of 8.5 GHz with a value of 6.62 dBi.

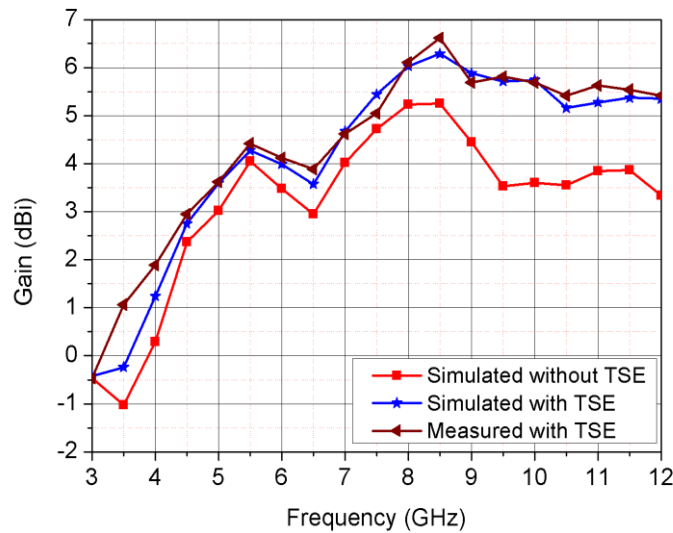


Figure 3.26 Measured and simulated gain of the designed AVA with and without TSE structure on ground plane.

3.4.1.6 Measured and simulated return loss

The comparison of measured and simulated return loss of the antenna is shown in Figure 3.27. The measurement was carried out by using a Vector Network Analyzer (37369A Anritsu).

The comparison shows a slight shift of 2.7% in frequency observed for the low resonant frequency (3.6 GHz for simulation vs. 3.7 GHz for measurements). The difference is mainly caused by fabrication and numerical errors and the connection loss between the printed circuit board and the SMA connector. It can be observed that both the simulated and measured bands of $S_{11} < -10dB$ range from 3.7 to more than 12 GHz. The photograph of the fabricated antenna is shown in figure 3.28.

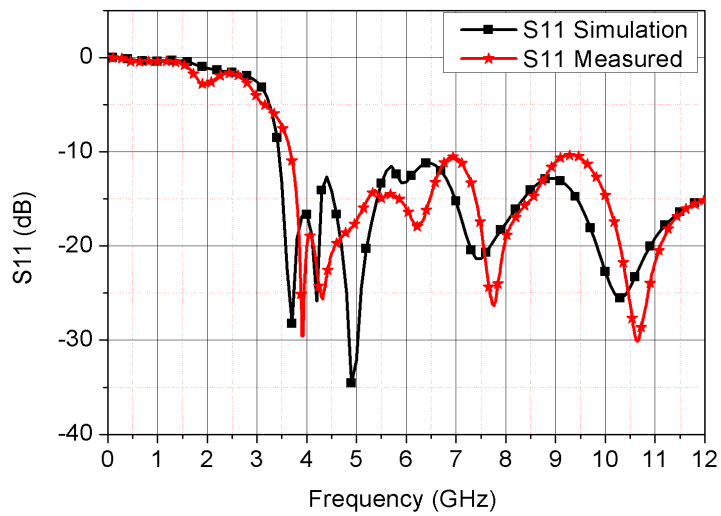


Figure 3.27 Comparison of simulated and measured return loss of AVA with TSE structure.

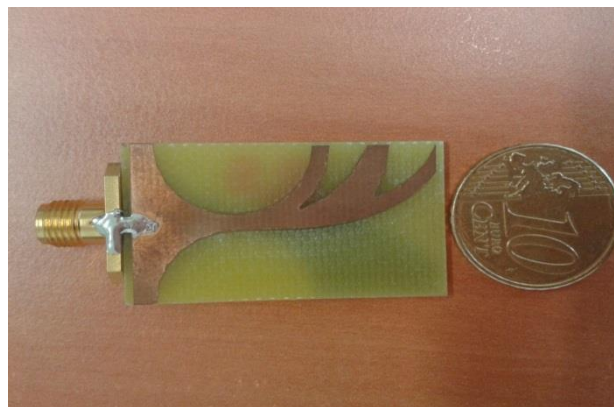


Figure 3.28 Photograph of the fabricated AVA.

3.5 Comparison of AVAs using a slot or a TSE

In order to further understand the behavior of the TSE and slot structures, the comparison between the two types of AVAs is done in this section. The results regarding return loss, far-field radiation pattern, antenna gain, and VSWR are illustrated.

4.2.1.3.1 Measured return loss of AVA with TSE and slot

The slot and TSE structures are etched on the ground plane with a shifted ground plane edge which was used to reduce the electrical size of antenna.

The effect of the etched slot and TSE structure on the input reflection coefficient is shown in figure 3.29. The return loss value for the antenna with a TSE structure is better than the one of the antenna with a slot at the lower-end frequency band, while the antenna with a slot is better at higher frequency. This is due to the increase of the effective current path added by the two structures. The current density on the edge of the TSE is relatively high while with slot the current density is lower, as shown in figure 3.30 which displays the simulated current distribution at 7 GHz for the two AVAs.

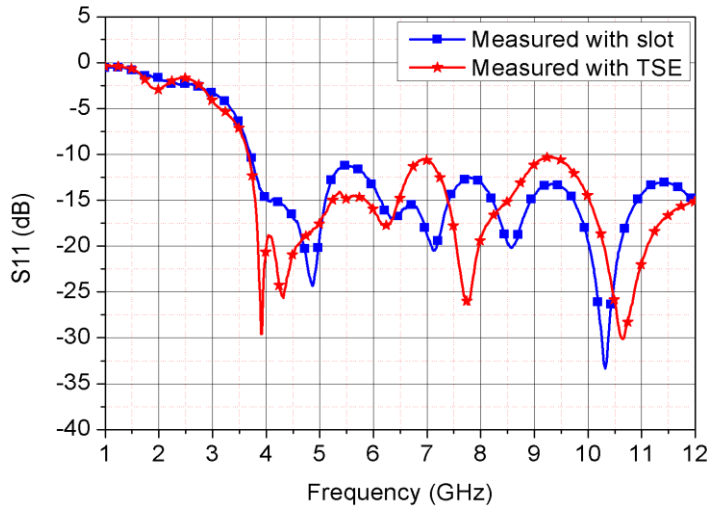


Figure 3.29 Measured return loss of AVAs with slot and TSE structure.

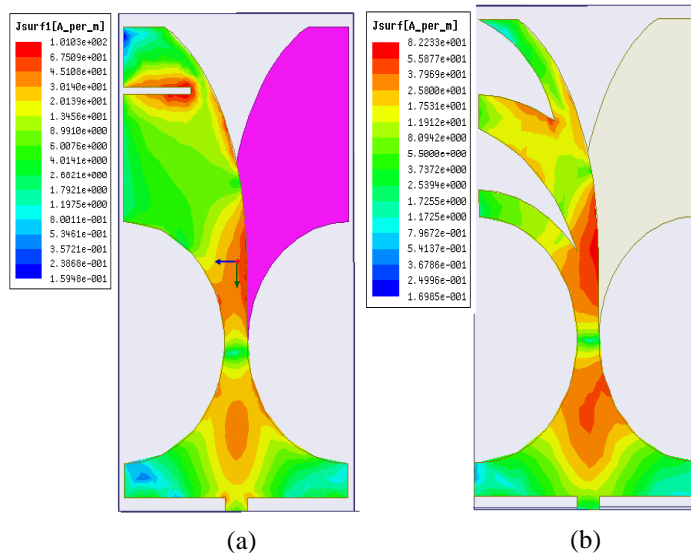


Figure 3.30 Simulated current distribution at 7 GHz for: (a) AVA antenna with etched slot. (b) AVA antenna with etched TSE structure.

4.2.1.3.2 Measured VSWR and gain of AVA with TSE and slot

The results for VSWR are shown in figure 3.31. In the case of the AVA with a slot and the AVA with TSE structure the impedance match and return loss are very good, with a VSWR < 1.8 through the frequency range.

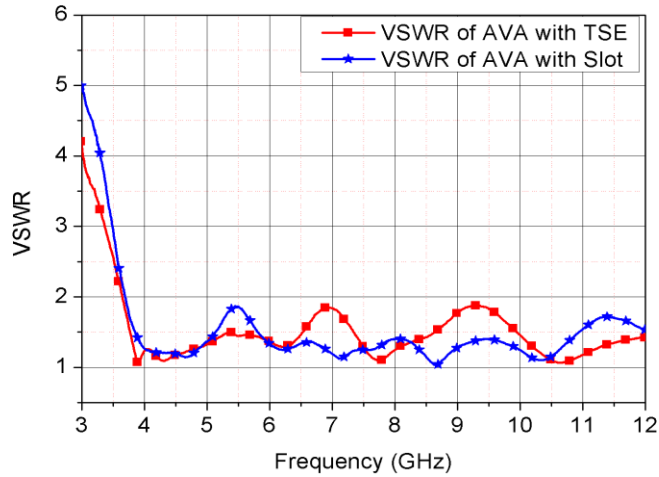


Figure 3.31 Measured VSWR of AVAs with slot and TSE structure.

The measured gains for both antennas are presented in figure 3.32. It can be seen that the gain increases when adding a TSE structure on the ground plane, where the measured maximum gain is 6.56 dBi at 8.5 GHz while the measured maximum gain for the AVA with a slot is 5.12 dBi at 11 GHz. Comparing the results one can conclude that adding the TSE structure increases the gain. This is due to the increase of the effective current density on the edge of the TSE, while with a slot the current density is lower.

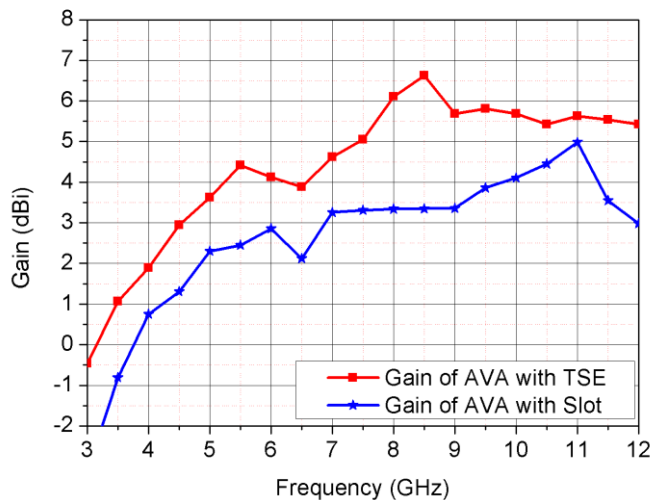


Figure 3.32 Measured gains of AVAs with slot and TSE structure.

3.6 Design of a small size UWB monopole antenna

A pair of monopole printed antennas [40] has also been designed, simulated and fabricated for our wireless UWB application. The monopole antenna is printed on FR4 substrate with a dielectric constant of $\epsilon_r = 4.25$, tangent loss $\tan \delta = 0.015$, and thickness of 1.6mm. The total size of this antenna is 18mm \times 12mm. The antenna is designed without the curved slot that was introduced in the original antenna. The simulations and measurements of the antennas were carried out using Ansoft HFSS simulation software and an Anritsu 37369A Vector Network Analyzer respectively. The geometry of the monopole antenna is shown in figure 3.33

A circular notch is etched in the ground plane to improve the impedance bandwidth of the antenna. In addition, an extension is added to each arm of the U-shaped radiating patch. These extensions are used to increase the length of the antenna to improve the low-end cutoff frequency.

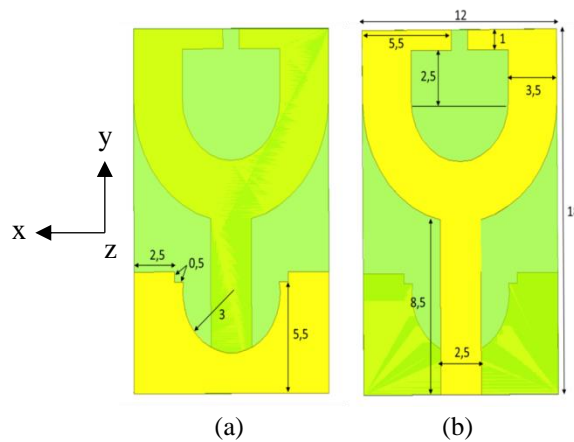


Figure 3.33 Configuration of the monopole antenna. (a) Bottom view. (b). Top view.

3.6.1 Results and discussion

The monopole antenna is designed to operate over a 3.1 to 10.9 GHz band. The antenna was simulated. The parameters of interest are the return loss, the VSWR, the gain, and far-field radiation patterns.

3.6.1.1 Return loss simulation and measurement

The simulated and measured reflection coefficients of the designed monopole antenna are plotted in figure 3.34. The return loss of the monopole antenna is adjusted to stay below -10 dB over the frequency band from 3.1 GHz to 10.9 GHz to satisfy the requirements of the UWB range.

The measurements are in good agreement with the simulated results with a measured return loss below -10dB from 3.1 to 11.3 GHz.

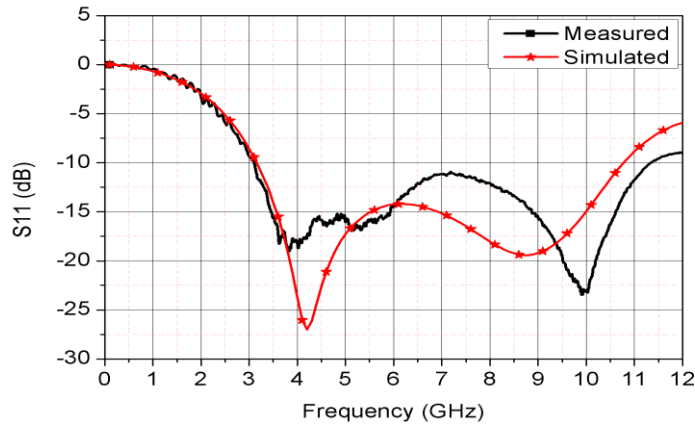


Figure 3.34 Measured and simulated return loss of the monopole antenna.

3.6.1.2 Radiation patterns

Far-field radiation patterns of the monopole antenna at different frequencies point are measured in an anechoic chamber. Co-polarization and cross-polarization patterns at 4.5, 8, 9.5, and 10.5 GHz in E-plane and H-plane are shown in figures 3.35 and 3.36. As shown in figure 3.35, it is observed that the radiation pattern of the designed monopole antenna exhibits a bi-directional pattern in E-plane while the H-plane pattern is omni-directional as shown in figure 3.36.

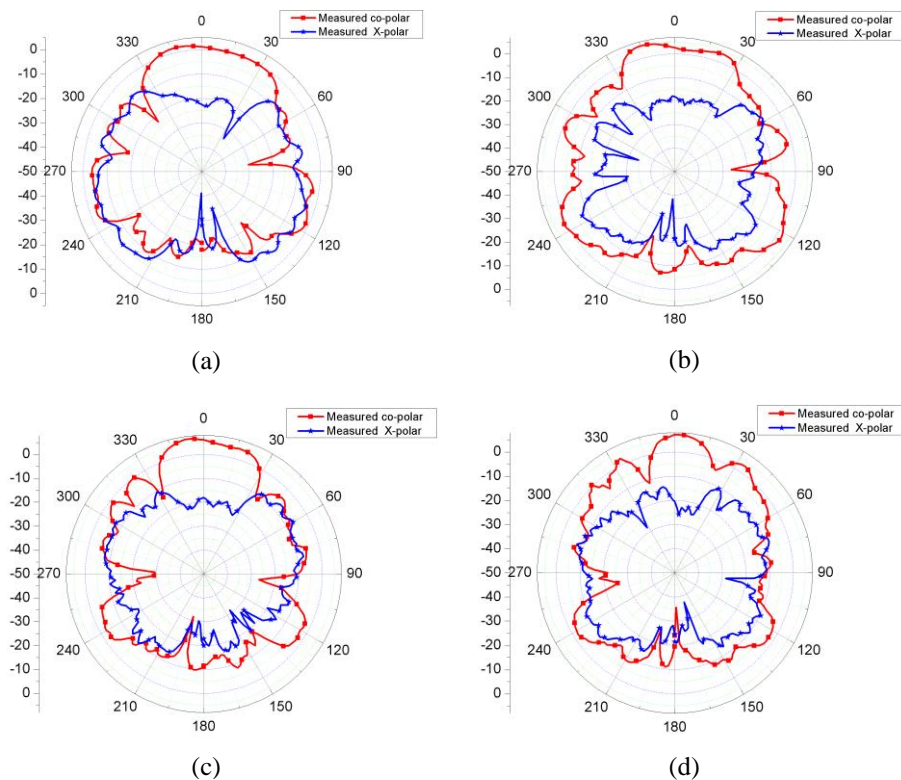


Figure 3.35 Measured radiation patterns of the designed monopole antenna in *E*-plane at (a) 4.5 GHz, (b) 8GHz, (c) 9.5GHz, and (d) 10.5GHz.

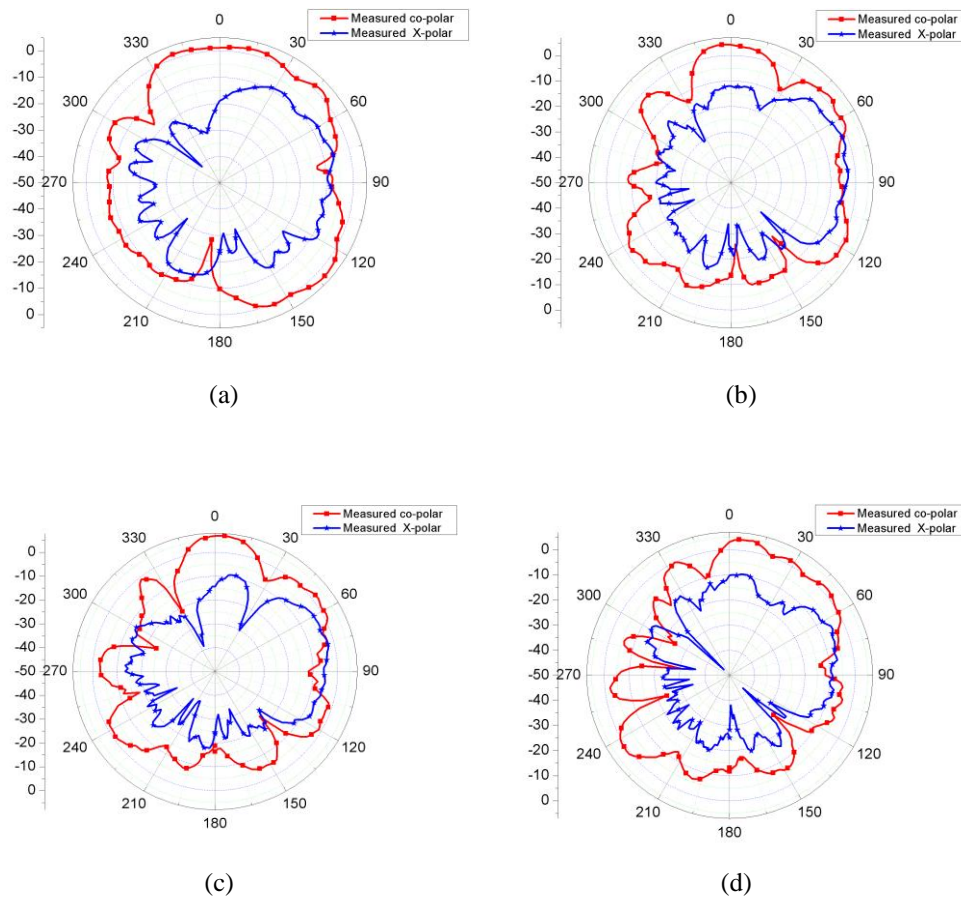


Figure 3.36 Measured radiation patterns of the designed monopole antenna in H -plane at (a) 4.5 GHz, (b) 8GHz, (c) 9.5GHz, and (d) 10.5GHz.

3.6.1.3 VSWR and gain of monopole antenna

The simulation and measured VSWR of monopole antenna are shown in figure 3.37. It can be observed that this antenna exhibits a measured VSWR lower than 2 from 3.1 to 11.3 GHz, that is for the entire UWB spectrum (3.1-10.6 GHz). The gain variation with frequency of the monopole antenna is shown in figure 3.38. As can be observed, the simulated gain increases with the frequency over the whole band of operation, while the measured gain increases from 3 to 10 GHz and decreases for frequencies between 10 to 12 GHz.

The measured maximum gain is 6.21 dBi for a frequency of 10.5 GHz, while a simulated maximum gain of 5.56 dBi was found at 12 GHz.

The difference between measurements and simulations increases with frequency with the highest difference of 2.11 dBi found at 10.5 GHz. We believe the reasons are mainly due to a delicate soldering with the connectors and possibly also an increase of substrate loss at higher frequencies. The photograph of the fabricated antenna is shown in figure 3.39.

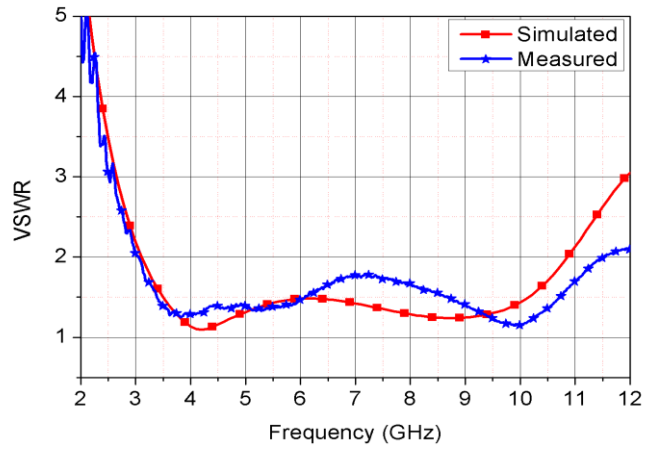


Figure 3.37 Simulated and measured VSWR of the monopole antenna.

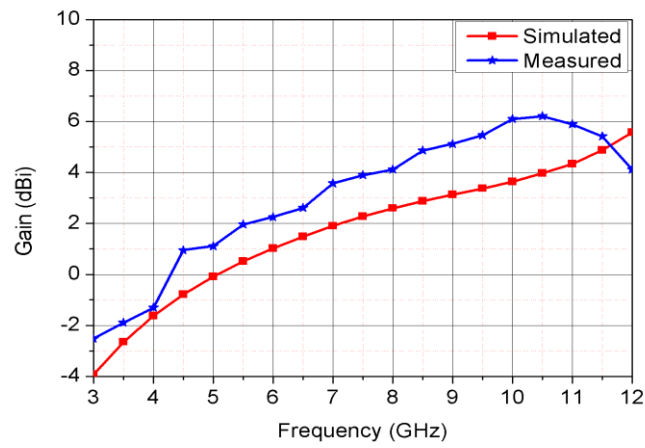


Figure 3.38 Simulated and measured gain of the designed monopole antenna.

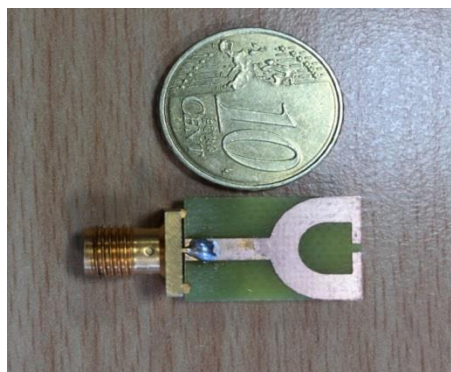


Figure 3.39 Photograph of the fabricated monopole antenna. Size is 18mm × 12mm.

3.7 SATIMO dual ridge horn antenna

In order to verify the WBT performance with a large antenna a pair of SATIMO dual ridge horn antennas with dimension (H*W*L) of 105 x 61 x 104.3 mm has been used in the frequency range from 2 GHz to 32 GHz in order to radiate digital streams such as Manchester and Polar RZ encoded signals directly without modulation techniques.

The SATIMO 2-32GHz dual ridge horn antenna is shown in figure 3.40. Figure 3.41 presents its return loss.

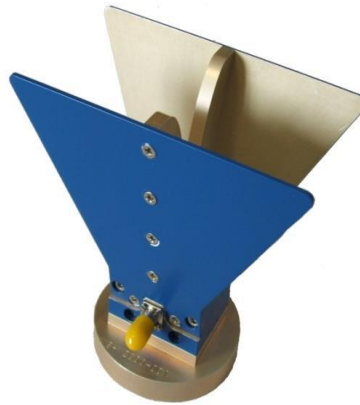


Figure 3.40 The SATIMO 2GHz–32 GHz dual ridge horn antenna. The nominal impedance is 50 ohms with return loss better than -10dB (VSWR < 1.9).

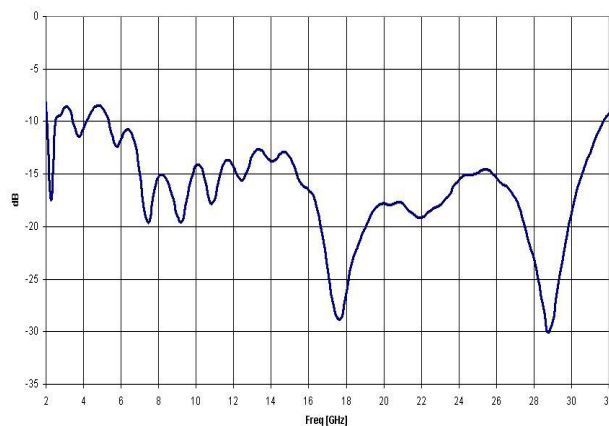
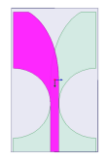


Figure 3.41 Return loss of the SATIMO dual ridge horn antenna.

Table 3.2 Summary of antennas designed in this chapter

	AVA	large AVA with slot	small AVA with slot	small AVA with TSE	Monopole antenna	Horn antenna
Antennas types						
Freq range. (GHz)	4.3- up to 12	2.5- up to 12	3.6- up to 12	3.1 - 10.9	3.1 - 10.8	2 - 32
Gain (dBi)	-----	0 - 6	-0.5 - 4.5	-0.5 - 5.5	-3.8 - 6.21	3 - 17
Dim. (mm ³) (L*W*H)	37*21*1.6	50*30*1.6	37*21*1.6	37*21*1.6	18*12*1.6	104.3*61*105
VSWR(<2)	4.3- <12	2.5 -<12	3.6 -<12	3.6 -< 12	3 - 10.9	2 - 32
Ω	50	50	50	50	50	50
radiation	directional	directional	directional	directional	Omni-directional	directional

3.8 Conclusion

In this chapter, compact size planar printed Antipodal Vivaldi and monopole antennas have been designed and fabricated. Two different Vivaldi antennas, with shifted ground plane edge and etched slot, or with a tapered slot edge on the ground plane brought significant improvements from the virtual AVA of dimensions $37*21*1.6 \text{ mm}^3$. The lower-end $S_{11} \leq -10 \text{ dB}$ limitation was extended to 3.6 GHz from the original 4.3 GHz. This indicates that the shifted ground plane edge with etched slot or TSE on ground plane are able to miniaturize the antenna by extending the lower bandwidth limit.

For the monopole antenna, the measured bandwidth is from 3.1 to 11.3 GHz with dimensions of $18*12*1.6 \text{ mm}^3$. Within the operating frequency band, the measured gain is better than 6.21 dBi. According to the characteristics, the three smaller sizes proposed antennas can be better candidates for UWB radio frequency applications. We will use them in the next chapter to transmit and receive the digital data directly.

We also used a pair of SATIMO dual ridge horn antennas with dimension (H*W*L) of 105 x 61 x 104.3 mm in the frequency range from 2 GHz to 32 GHz to radiate sequence streams such as Manchester and Polar RZ encoded signals directly without any modulation technique. This will be developed in the next chapter.

The results of this chapter are published in:

F. Abayaje, P. Febvre, "A Customized Reduced Size Antipodal Vivaldi Antenna for Transmission of Cryogenic Backend Digital Data," ESA/ESTEC Antenna workshop conference, 6-9 October, 2015.

Furat Abayaje, Pascal, Febvre, "A customized reduced size Antipodal Vivaldi Antenna used in Wireless Baseband Transmission for short-range communication," International journal of Electronic and Communications (AEU), no. 70, pp.1684-1691, 2016.

Bibliography

- [1] C. A. Balanis, *Antenna Theory: Analysis and Design*, Hoboken, New Jersey, USA, Wiley 2005.
- [2] Q. Balzano, O. Garay, "The near field of Dipole antennas, part I: theory," *IEEE Transactions on Vehicular Technology*, vol. VT-30, no. 4, November 1981.
- [3] S. M. mikki, Y. M. M. Antar, "A Theory of Antenna Electromagnetic Near Field-part I," *IEEE Transactions on Antenna and propagation*, vol. 59, no. 12, December 2011.
- [4] W. Wiesbeck, and G. Adamiuk, "Antenna for UWB systems," in *Proc. 2nd int. ITG Conf. antennas (INICA)*, pp. 67–71, March 28-30 2007.
- [5] A. Foudazi, H. R. Hassani, and S. M. A. Nezhad, "Small UWB Planar Monopole Antenna With Added GPS/GSM/WLAN Bands," *IEEE transaction on antennas and propagation*, vol. 60, no. 6, pp. 2987-2992, June 2012.
- [6] J. Bai, S. Shi, and D. W. Prather, "Modified Compact Antipodal Vivaldi Antenna for 4-50 GHz UWB Application," *IEEE Transactions on Microwave Theory and Techniques*, vol. 59, no.4, pp. 1051-1057, April 2011.
- [7] J.D.S. Langley, P.S. Hall, and P. Newham, "Balanced antipodal Vivaldi antenna for wide bandwidth Phased arrays," *IEEE Proc.-Microwave Antenna propagation*, vol. 143, no. 2, April 1996.
- [8] M. Ojaroudi, G. Ghanbari, N. Ojaroudi, and C. Ghobadi, "Small Square Monopole Antenna for UWB Applications with Variable Frequency Band-Notch Function," *IEEE Antennas and Wireless Propagation Letters*, vol. 8, pp. 1061-1064, 2009.
- [9] A. M. Abbosh, Senior, "Miniaturization of Planar Ultra-wideband Antenna via Corrugation," *IEEE Antenna and Wireless Propagation Letters*, vol. 7, 2008.
- [10] A. M. Abbosh and M. E. Bialkowski, "Design of Ultra- Wideband Planar Monopole Antenna of Circular and Elliptical Shape," *IEEE Transaction Antennas Propagation Letters*, vol. 56, pp. 17-23, January 2008.
- [11] X. Lai, Z. Xie, and X. Cen, "compact Loop Antenna for Near-Field and Far-Field UHF RFID Applications," *Progress in Electromagnetics Research*, vol. 37, pp. 171-182, 2013.
- [12] Ahmed A.Kishk, "Fundamental of antennas", center of electromagnetic system research (CEDAR), department of electrical engineering, University of Mississippi.
- [13] A. Bensky, "Short-rang wireless communication ", fundamental of RF system Design and Application, book, a volume in the demystifying technology series www.LLH-publishing.com.

- [14] John Choma, "Scattering parameters: concept, theory, and applications", University of Southern California, Ming Hsieh Department of Electrical Engineering, November 2002.
- [15] Teguh Prakoso, Razali Ngah, and Tharek Abdul Rahman, "Representation of Antenna in two-Port Network S-Parameter", wireless communication center faculty of Electrical Engineering, University Teknologi Malaysia, IEEE international RF and microwave conference proceeding, December 2-4, 2008.
- [16] Hailong Zhu, Y.C. Andrew Ko, and Terry T. Ye, "Impedance Measurement for Balanced UHF RFID Tag Antennas", Hong Kong R&D Centre for Logistics and Supply Chain Management (LSCM).
- [17] P. J. Gibson, "The Vivaldi aerial", Proc. 9th European Microwave Conf., pp.101-105, 17-20 Sept. 1979.
- [18] P. Fei, Y.C. Jiao, W. Hu, and F.S. Zhang, "A Miniaturized Antipodal Vivaldi Antenna with Improved Radiation Characteristics", IEEE Antenna and Wireless Propagation Letters, vol. 10, pp.127-130, 2011.
- [19] Z. Aaron, K. Tutku, and T. Erdem, "A Small Antipodal Vivaldi Antenna for Ultra-wide-Band Applications", IEEE Antennas Wireless Propagation Letters, vol.7, pp. 656-660, 2008.
- [20] R. Natarajan, J. V-George, M. Kanagasabai, and A. Kumar-Shrivastav, "A Compact Antipodal Vivaldi Antenna for UWB Applications", IEEE Antenna and Wireless Propagation Letters, vol.14, pp. 1557-1560, 2015.
- [21] G. Teni, N. Zhang, J. Qiu, and P. Zhang, "Research on a Novel Miniaturized Antipodal Vivaldi Antenna with Improved Radiation", IEEE antennas and wireless propagation letters, vol. 12, pp. 417-420, 2013.
- [22] G. Brzezina, R.E. Amaya, A. Petosa, and L. Roy, "Vivaldi Antenna for MM-Wave Communications", High Frequency Electronics, pp.22-30, Oct.2014.
- [23] M.C. Greenberg, K.L. Virga, and C.L. Hammond, "Performance characteristics of the dual exponentially tapered slot antenna (DE TSA) for wireless communications applications", IEEE transactions Vehicular Technology, vol. 52, no. 2, March 2003.
- [24] D. M. Pozar, "Microwave Engineering," John Wiley and Son, pp.148-150, 2005.
- [25] Z. Wang, Y. Yin, J. Wu, R. Lian, "A Miniaturized CPW-Fed Antipodal Vivaldi Antenna with Enhanced Radiation Performance for Wideband Applications", IEEE Antenna and Wireless Propagation Letters, vol. 15, pp. 16-19, 2016.
- [26] J. Y. Siddiqui, Y. M. M. Antar, A. P. Freundorfer, E. C. Smith, G. A. Morin, and T. Thayaparan, "Design of an Ultra-wideband Antipodal Tapered Slot Antenna Using Elliptical Strip Conductors", IEEE Antennas Wireless Propagation Letters, vol. 10, pp 251-254, 2011.

- [27] M. A. Kenari, M. N. Moghadasi, R. A. Sadghzadeh, B. Virdee, E. Limiti," Bandwidth extension of planar antennas using embedded slits for reliable multiband RF communications. *AEU-International Journal of Electronics and Communications*, 70(7), pp.910-919, 2016.
- [28] B. Roy, A. Bhattacharya, S. K. Chowdhury, A. K. Bhattacharee," Wideband Snowflake slot antenna using Koch iteration technique for wireless and C-band applications, *AEU-International Journal of Electronics and Communications*, 7(10),pp.1467-1472, 2016.
- [29] S. E. Hosseini, A. R. Attari, and A. Pourzadi," A Multiband PIFA with a Slot on the Ground Plan for Wireless Applications," *International Journal of Information and Electronics Engineering*, vol. 3, no. 4, pp. 349-352, July 2013.
- [30] Q. Ying, and W. Dou," Simulation of Two Compact Antipodal Vivaldi Antenna with Radiation Characteristics Enhancement," *IEEE international Symposium Antenna and Propagation (ISAP)*, vol.1, pp.523-526, 23-25 Oct.2013.
- [31] Y.W. Wang, G.M. Wang, and B.F. Zong,"Directivity Improvement of Vivaldi Antenna Using Double-Slot Structure," *IEEE Antennas Wireless Propagation Letters*, vol. 12, pp. 1380-1383, 2013.
- [32] M. Ostadrahimi, S. Noghianian, and L. Shafai," A Modified Double Layer Tapered Slot Antenna with Improved Cross Polarization," *International Symposium on Antenna technology and Applied Electromagnetics and the Canadian Radio Sciences Meeting*, 2009.
- [33] M. Chiappe, and G.L. Gragnani," Vivaldi Antenna for Microwave Imaging: Theoretical Analysis and Design Considerations," *IEEE Transaction on Instrumentation and Measurement*, vol. 55, no.6, pp.1885-1891, Dec. 2006.
- [34] G. Brzezina, L. Roy, and L.Mac-Eachern," Planar antennas in LTCC Technology with Transceiver Integration Capability for Ultra-Wideband Applications," *IEEE Transactions on Microwave Theory and Techniques*, vol. 54, no. 6, June 2006.
- [35] G. Teni, N. Zhang, J. Qiu, and P. Zhang," Research on a Novel Miniaturized Antipodal Vivaldi Antenna with Improved Radiation," *IEEE Antennas Wireless Propagation Letters*, vol. 12, pp. 417-420, 2013.
- [36] S. Wang, X. D. Chen, and C. G. Parini, "Analysis of ultra-Wideband antipodal Vivaldi antenna design," *Proc. Loughborough Antennas and Propagation Conference (LAPC)*, pp. 129-132, April 2007.
- [37] Y. X. Che, K. Li, X.Y. Hou, and W.M. Tian," Simulation of A Small Sized Antipodal Vivaldi Antenna for UWB Applications," *ICUWB. Nanjing, China*, pp. 1-3, 20-23 Sept 2010.
- [38] S. A. Shetawy, E. A. Abdallah, and D. Abdel-Aziz, "Slotted Ground Plane of Rectangular Patch Microstrip Antenna with Enhanced Bandwidth and size Reduction," *Proc. 12th WSEAS International Conference on Communications, Heraklion, Greece*, July 23-25, 2008.

- [39] M. Karahan, D. S. A. Sahinkaya,” A Reduced Size Antipodal Vivaldi Antenna Design for Wideband Applications,” *IEEE Antennas and Wireless Propagation Letters*, pp. 1588-1589, 2014.
- [40] E. Tammam, L. Yang, A. Allam, M. Ragab, K. Yoshitomi, R. Pokharel, and K. Yoshida,” Design of a Small Size UWB Antenna with Band-rejection Characteristics,” *IEEE, Japan-Egypt Conference on Electronics, Communications and Computers*, pp. 112-117, 2012.

4 Experimental assessment of WBT with a short distance configuration

4.1 Introduction

Wireless Baseband Transmission at short distance with small size antennas has been studied in the two previous chapters. In chapter 2, the transfer function characterization of a printed UWB antenna has been used for better UWB channel and communication system designs using frequency domain simulations. Two different approaches were used to estimate the BER at 1Gbps for a distance in the range 1-15 cm between antennas. In the first approach, the first harmonic of input signal in the 0.5-1.5 GHz frequency band was transmitted with a large size antenna, which has a lower cutoff frequency of 0.5GHz. In the second approach we have observed that a small size antenna is applicable for WBT when the lower cutoff frequency is 4GHz, using only higher harmonics of the signal.

In chapter 3, an Antipodal Vivaldi Antenna with a reduced size of 37mm×21mm has been designed, simulated, fabricated and measured on 1.6mm-thick FR4 substrate. A monopole antenna with a reduced size of 18mm×12mm has also been designed and fabricated on 1.6mm-thick FR4 substrate. These two antennas can be used for WBT.

In this chapter, a full simulation and experimental study of WBT at short distance with 1Gbps data rate is done. The received signals in the time domain were captured with a Digital Storage oscilloscope (DSO) and the results of those measurements were used to carry out calculations of BER. In this chapter, two methods are considered to transmit and receive the encoded Manchester and Polar RZ signals directly from an antenna at 1Gbps and on a short distance. The first method is based on using two small AVA antennas and monopole antennas. The second method is based on using standard horn antennas.

The measurement is done at room temperature in order to make WBT assessment more practical. The space around the receiving antenna can be divided into two main regions: far field and near field. In the far field, electric and magnetic fields propagate outward as an electromagnetic wave and are perpendicular to each other and to the direction of propagation. The near field region includes two sub-regions: radiating and reactive. The approximate boundary between the far field and near field regions is commonly given by $r = 2\lambda$ when $D \ll \lambda$ and $r = 2D^2/\lambda$ when $D \gg \lambda$ where D is the largest antenna dimension and λ is the wavelength. In order to calculate the inner boundary of the far field region for broadband WBT, one needs to know the maximum frequency that is transmitted. It depends on the number of samples per bit in our case since the antennas we use transmit signals up to frequencies above 12 GHz. As mentioned earlier in chapter 2, the maximum frequency with 12 samples per bit is 6GHz for a data rate of 1Gbps. For 8 samples it is 4GHz.

Figure 4.1 gives the far-field region boundary according to the number of points per bit. From this figure, the far field boundary with 12 points per bit is $r = 5.5\text{cm}$ with AVA and $r = 43.5\text{cm}$ with horn antenna.

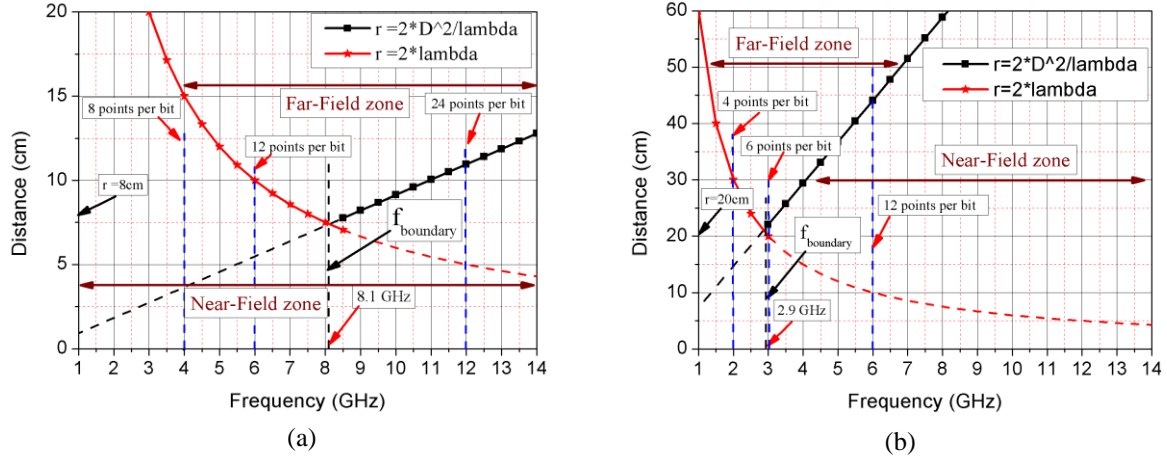


Figure 4.1 Far-field region boundary according to the number of points per bit for (a) antipodal Vivaldi antenna ($D = 3.7 \text{ cm}$ and $f_{\text{boundary}} = 8.1 \text{ GHz}$) and (b) horn antenna ($D = 10.5 \text{ cm}$ and $f_{\text{boundary}} = 2.9 \text{ GHz}$).

The simulations of the power spectrum of encoded signals at 1Gbps are shown in chapter 1 (see figure 2.12). The Nyquist frequency is pushed at higher values and the upper frequency of the FFT increases with number of points per bit. The frequency of the boundary between near-field and far-field zones is $f_{\text{boundary}} = \frac{c}{D}$. For AVA $f_{\text{boundary}} = 8.1 \text{ GHz}$ while for horn antenna $f_{\text{boundary}} = 2.9 \text{ GHz}$. The far-field region of the AVA is always satisfied when the distance is $\geq 8 \text{ cm}$ while the distance from horn antenna is $\geq 20 \text{ cm}$ as shown in figure 4.1.

The S-parameters of the antenna system were measured in the frequency domain using an Anritsu 37369A Vector Network Analyzer (VNA). The analyzer is swept from close to DC to about 12 GHz and the complex response of the system measured. An Arbitrary Wave Generator (Tektronix 7122B AWG, 12-24GS/s, 4.8-9.6GHz) is used as a transmitter and a digital storage oscilloscope (Tektronix DSO TDS6604B, 6GHz and 20GS/s) is used as a receiver. Manchester and Polar RZ encoded signals at 1Gbps are generated using a computer and are supplied to the AWG, which sends them directly to the emitting antenna at room temperature.

4.2 Small size antennas used for wireless baseband transmission in a short distance configuration

In this section, two different types of small antennas are used to transmit and receive the encoded signals at short distance. The first type is an antipodal Vivaldi antenna (the antenna with etched slot and TSE), while the other one is a monopole antenna. In the previous chapter, we saw that a directional antenna is capable of directing most emitted power in a lobe or beam, while a standard omnidirectional antenna transmits the energy in all directions. With a directional transmitting antenna, the receiving antenna can get more radiated energy, thus reducing the required transmission power. Therefore, we decided to use the two types of antenna in order to find the best solution.

4.2.1 WBT measurements with Antipodal Vivaldi Antenna

We estimated the performance of AVA antennas placed at short distance in an aligned configuration to transmit and receive directly Polar RZ and Manchester digital signals without modulation technique. The transmitting and receiving antennas were oriented with the same polarization so that the same parts of their radiation patterns point at each other. The distance between the closest edges of each AVA has been varied from 1cm to 15cm. The lower frequency transmitted by antipodal Vivaldi antennas is 3.6 GHz, as observed in chapter 3.

In this section, two steps are considered for the characteristic of wireless baseband transmission. The first step is based on using S-parameters based transfer functions of antipodal Vivaldi antennas. The second step is based on using an AWG and a DSO to transmit and receive the digital data signal directly between two identical antennas.

4.2.1.1 Measurements of S-parameters of Antipodal Vivaldi Antenna

An antipodal Vivaldi antenna was studied to validate the transfer functions (magnitude together with phase) experimentally. Two identical AVA antennas were placed at short distance in an aligned configuration, the transmitting and receiving antennas were oriented with the same polarization so that the same parts of their radiation patterns point at each other as shown in figure 4.2. The distance between the closest edges of each AVA has been varied from 1cm to 15cm.

The S-parameters values were captured from the VNA and calculations of BER were carried out to assess the WBT performance at 1Gbps using 1000 bit-code patterns. The measured S-parameters (S_{11} and S_{21}) of the AVA antennas are shown in figure 4.3. They show a linear phase response over most of the frequency range of antennas. The bandwidth of linear phase response is important for baseband pulse transmission.

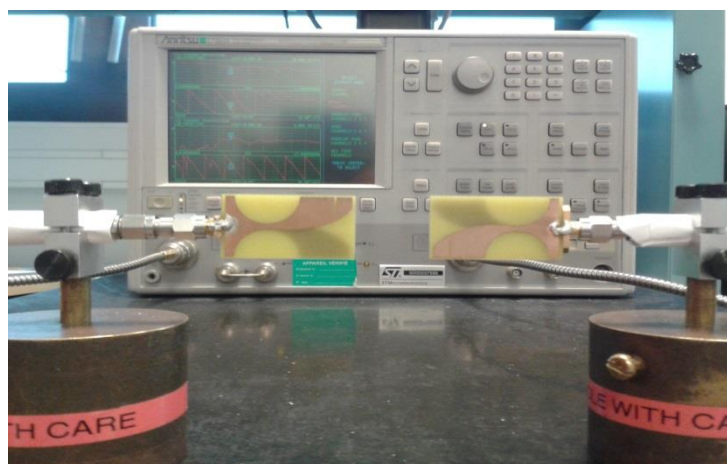


Figure 4.2 Setup of two antipodal Vivaldi antennas placed in an aligned configuration. The S-parameters of the antenna system were measured using an Anritsu 37369A Vector Network Analyzer (VNA).

Results shown in figure 4.3 (a, b) correspond to the case where the two antennas were placed at a 2 cm distance from each other corresponding to the near field case (see figure 4.1(a)). S_{21} shows a flat amplitude and a linear phase from 3.6 GHz to 12 GHz. Also, the two antennas were placed with a sufficient horizontal distance of 10cm to be in the far field, as shown in figure 4.3 (c, d). Clearly, the linear phase is also observed from 3.6 GHz to 12 GHz.

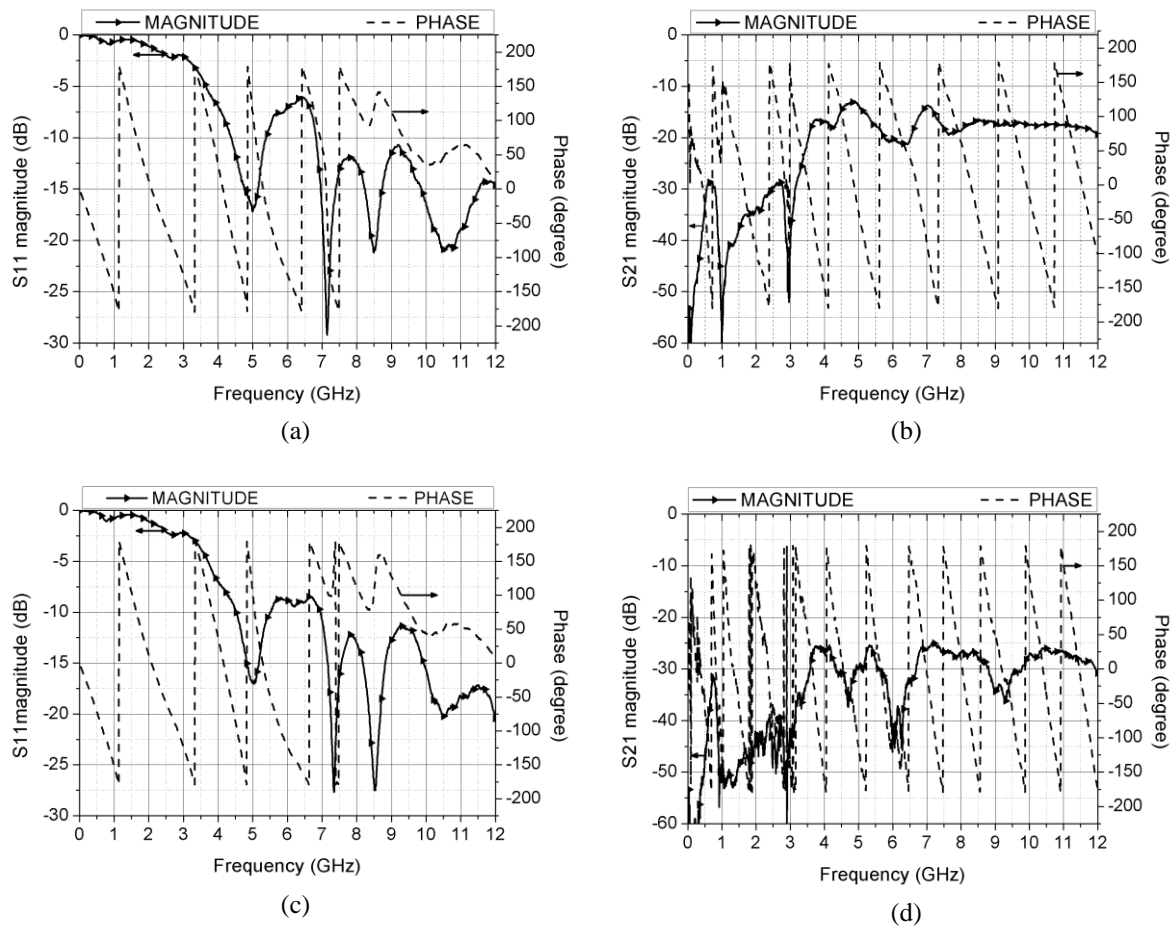


Figure 4.3 Measured S-parameters of the set of two antipodal Vivaldi antennas placed in an aligned configuration. (a) S_{11} at 2 cm distance. (b) S_{21} at 2 cm distance. (c) S_{11} at 10 cm distance. (d) S_{21} at 10 cm distance.

4.2.1.2 Simulations of WBT with measured S-parameters

Simulations in the frequency domain have been done with two identical antennas in an aligned configuration. Figure 4.4 shows the transmission characteristics of the antenna system for Polar RZ line code. The input data stream and the antenna transmission transfer function are multiplied in the frequency domain, while the output data is shown in the time domain after inverse FFT. In this section, the measured S-parameters were used to perform simulations and the BER values results are an average based on 100 simulations with random digital input signals.

The comparison between the digital input and output signals is also presented in this figure. It is observed that the output digital signal agrees well with the input digital signal when the distance is lower than 7cm, because of the exponential decay of BER with distance. These cases correspond to the near-field configuration for the whole transmitted frequency range (see figure 4.1-a).

Figure 4.4 indicates also the simulated BER values versus distance based on two BER techniques:

- Digital input signal of Polar RZ line code at 1Gbps using 1000-bit code pattern and 12 points per bit;
- S_{11} (red) and S_{21} (blue) S-parameters measured using a VNA;
- Digital output signal at receiver side (after inverse FFT) and BER values obtained for two BER techniques;
- Comparison between the input and output digital data signals.

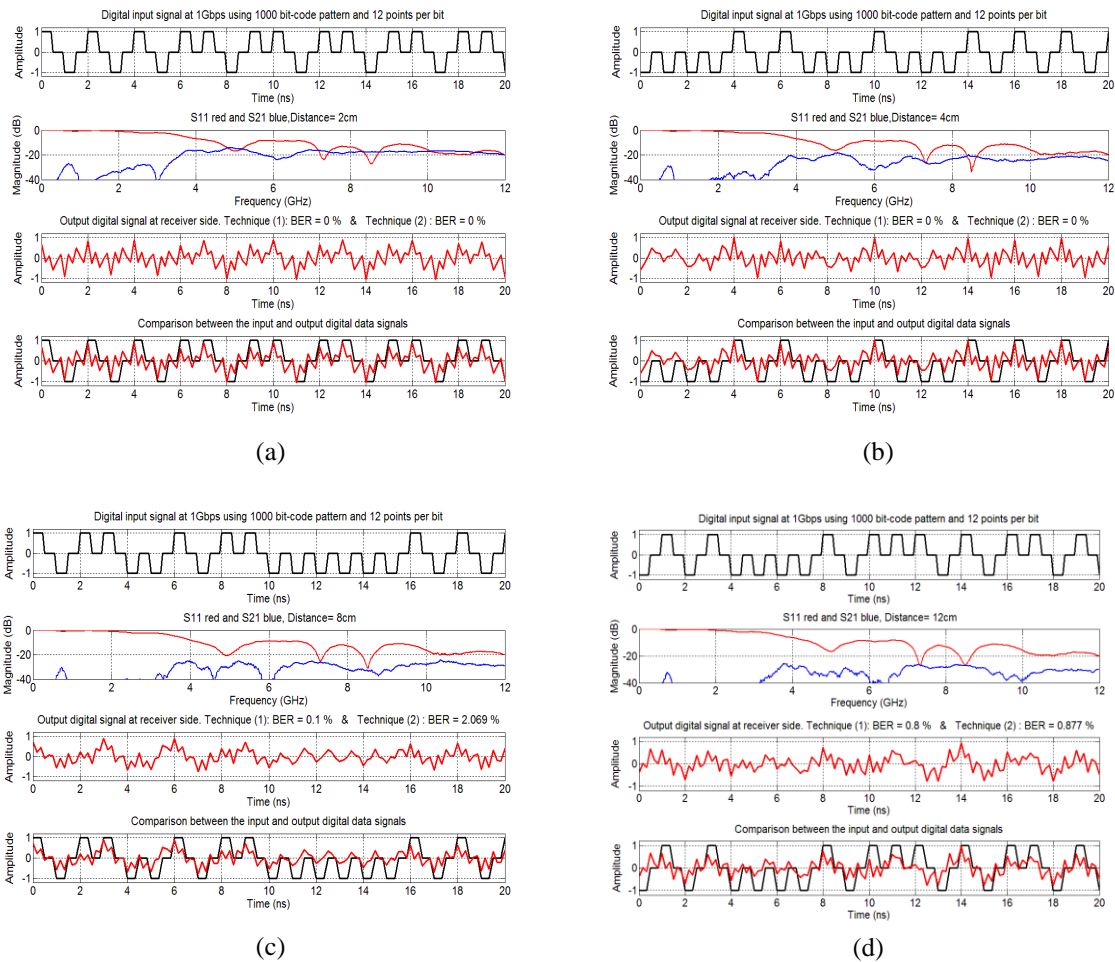


Figure 4.4 Simulations of WBT for a Polar RZ encoded signal at 1Gbps with 12 points per bit and 1000-bit code pattern, BER are obtained after 100 simulations with random input sequences. (a) $d=2\text{cm}$. (b) $d=4\text{cm}$. (c) $d=8\text{cm}$. (d) $d=12\text{cm}$. Measured S-parameters were used to perform simulations.

WBT simulation results are obtained using two BER techniques described before in chapter 2 (section 2.5) by comparing input and output signals.

The comparison between figures 4.4(a, b) and figures 4.4(c, d) reveals that the same digital waveforms are obtained for figures 4.4(a, b) while in figures 4.4(c, d) we can find one error and eight errors when the distances between antennas are 8cm and 12cm respectively.

Figure 4.5 shows the transmission characteristics of the antenna system for Manchester line code at a data rate of 1Gbps using 1000-bit code pattern and 12 points per bit. BER are calculated from 100 simulations with random input sequences.

It is observed that the output digital signal agrees well with the input digital signal for the distances of 2, 4 and 8cm, while a non-zero BER is observed when the distance between antennas is higher than 10cm.

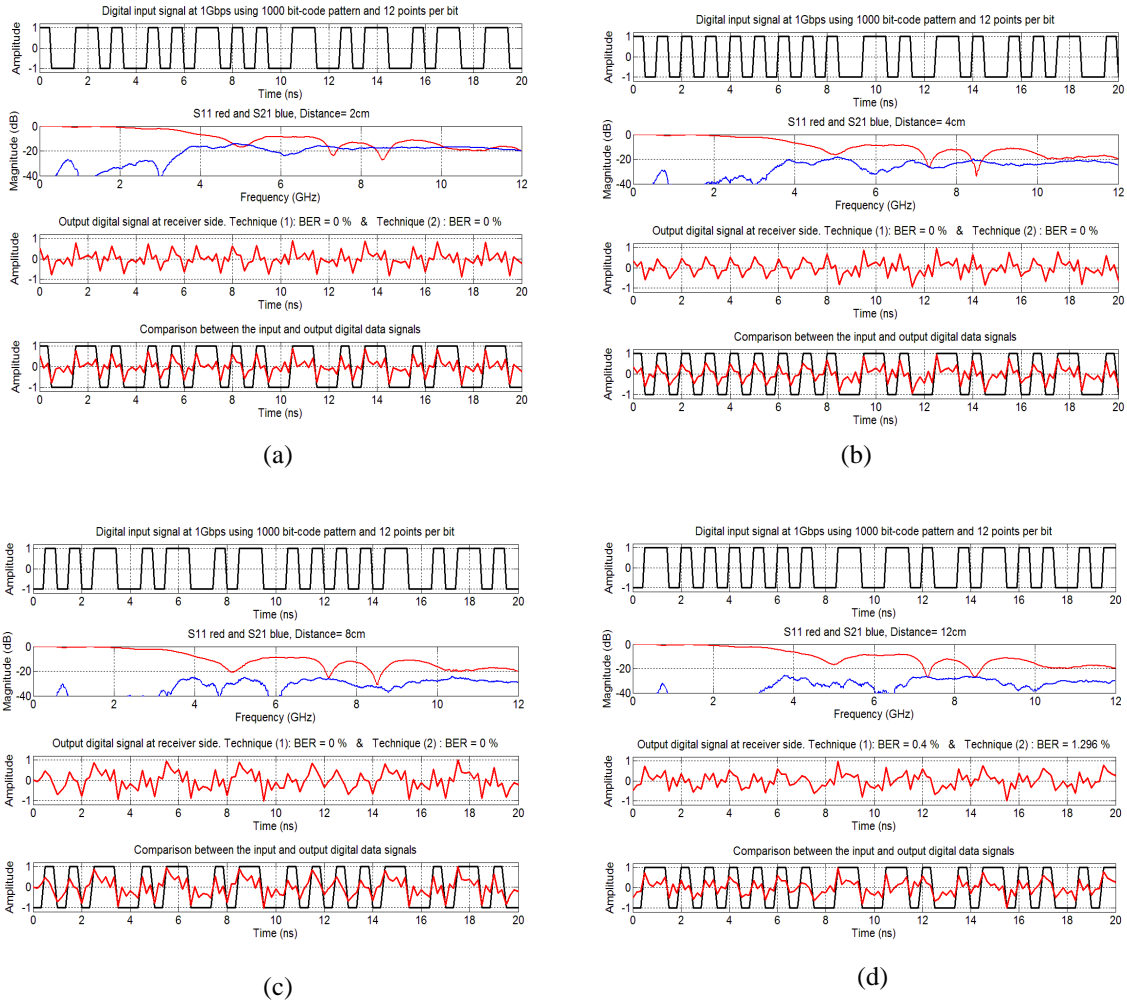


Figure 4.5 Simulations of WBT for a Manchester encoded signal at 1Gbps with 12 points per bit and 1000-bit code pattern, BER are obtained after 100 simulations with random input sequences.(a) d=2cm. (b) d=4cm. (c) d=8cm. (d) d=12cm. Measured S-parameters were used to perform simulations.

In order to analyse the transmission characteristics of WBT with different input data rates and samples per bit, some simulations were done at an input rate of 2Gbps with 6 points per bit (6 points per bit was chosen because of the limitation of our AWG (12GS/s) to compare with WBT measurements in the next section).

Figure 4.6 shows the transmission characteristics of the antenna system for Polar RZ line code at a data rate of 2Gbps with 6 points per bit using 1000-bit code pattern. BER are calculated from 100 simulations with random input sequences. It is observed that the output digital signal agrees well with the input digital signal for distances of 2cm and 4cm.

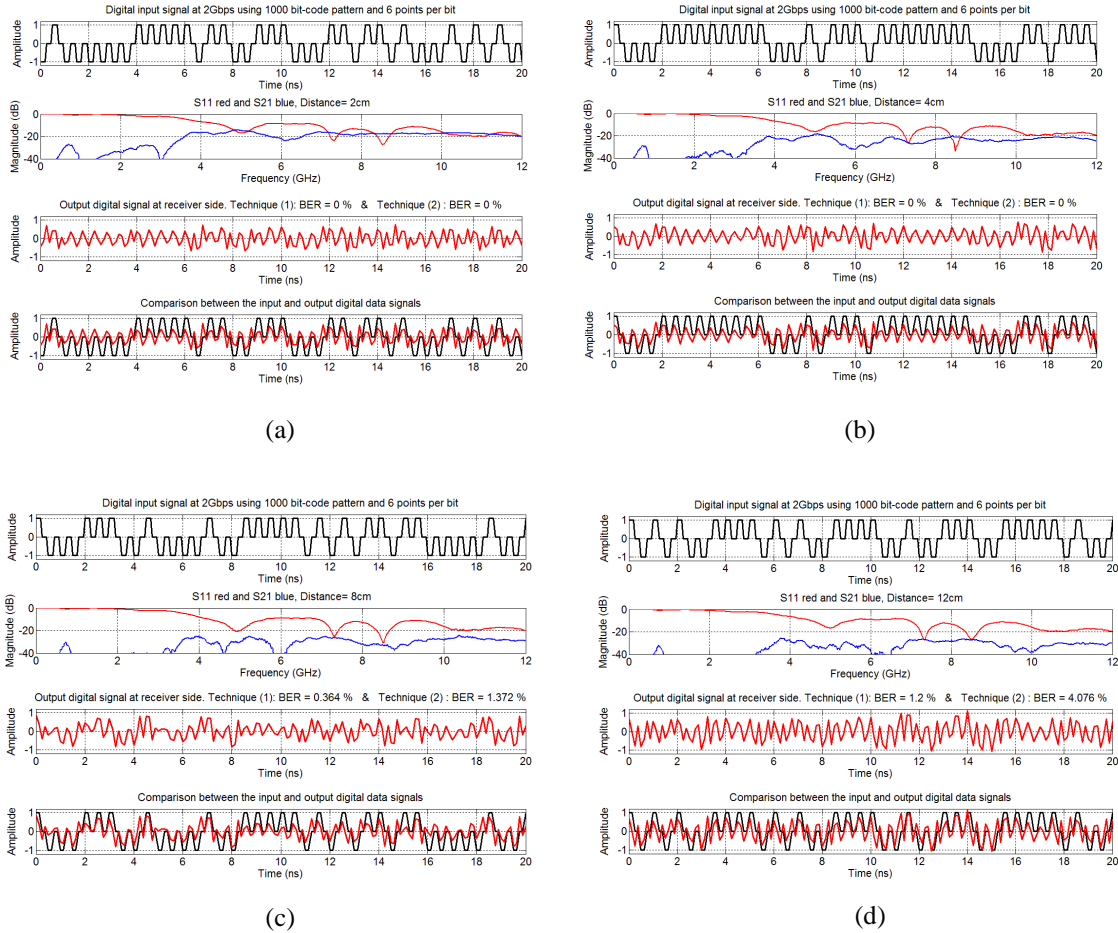


Figure 4.6 Simulations of WBT for a Polar RZ encoded signal at 2Gbps with 6 points per bit and 1000-bit code pattern, BER are obtained after 100 simulations with random input sequences. (a) d=2cm. (b) d=4cm. (c) d=8cm. (d) d=12cm.

Also with the same above procedure, figure 4.7 shows the transmission characteristics of the antenna system for Manchester line code at a data rate of 2Gbps and 6 points per bit using 1000 bit-code pattern. As can be seen in this figure, the output digital signal agrees well with the input digital signal for distances of 2, 4, and 8cm where zero BER values are observed.

Figure 4.8 shows a comparison of BER values versus distance from 1cm to 15cm for both Manchester and Polar RZ encodings at a data rate of 1Gbps and 2Gbps using 1000-bit code pattern with 12 and 6 points per bit respectively. BER values for the two line codes are higher when the distance between the two antennas is increased. When we compare results for each encoding scheme, we see that the BER for Polar RZ is 4×10^{-3} at a data rate of 2Gbps while it is 10^{-3} at a data rate of 1Gbps with the same distance of 8cm. In addition, we see that the BER for Manchester encoding is 4×10^{-3} at a data rate of 2Gbps while it is 10^{-3} at a data rate of 1Gbps with the same distance of 10cm. Both signals at 1 and 2Gbps were sampled at 12GS/s. The third harmonic (4GHz-6GHz) was transmitted at 1Gbps while the second harmonic was transmitted at 2Gbps (4GHz-6GHz).

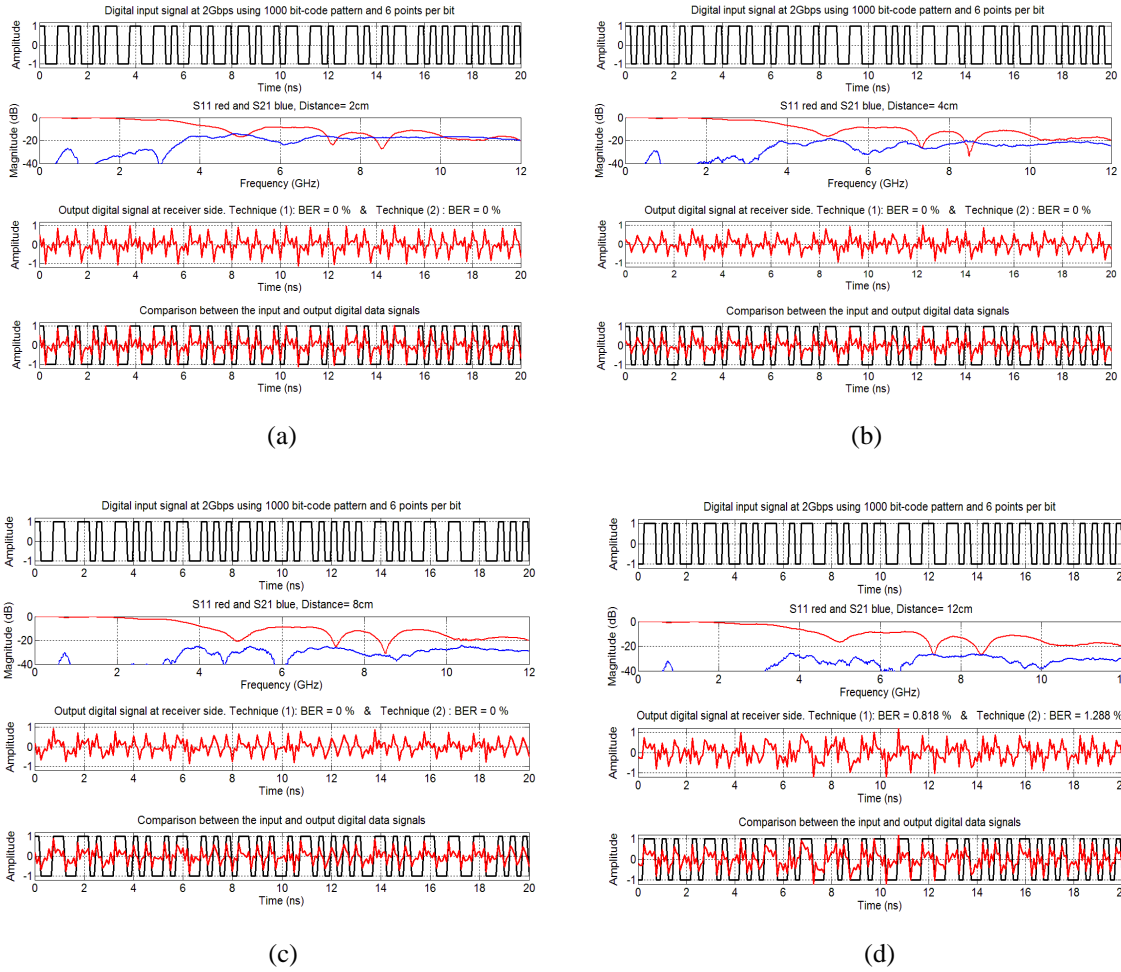


Figure 4.7 Simulations of WBT for a Manchester encoded signal at 2Gbps using a 100-loops input data with 6 points per bit and 1000-bit code pattern, BER are obtained after 100 simulations with random input sequences. (a) $d=2\text{cm}$. (b) $d=4\text{cm}$. (c) $d=8\text{cm}$. (d) $d=12\text{cm}$.

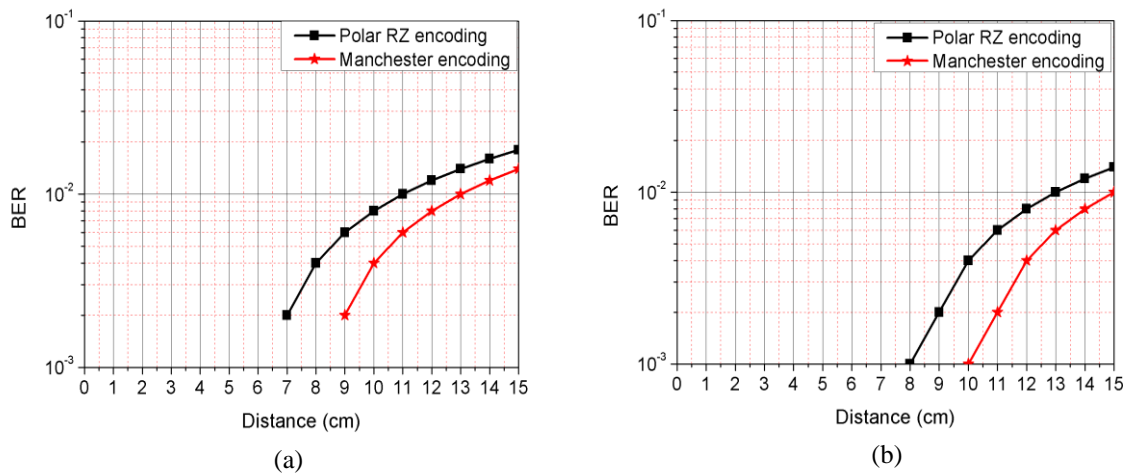


Figure 4.8 Simulated BER for polar RZ and Manchester encodings versus distance between two AVA antennas using 1000-bitcode pattern. (a) Data rate at 2Gbps with 6 points per bit. (b) Data rate at 1Gbps with 12 points per bit. Measured S-parameters were used to perform simulations.

The number of samples per bit and the line code choice play an important role in this communication system since the transmitted energy is mostly located in the high frequency part of the associated digital signal spectrum. We showed that WBT at 1Gbps and 2Gbps can be achieved for Polar RZ and Manchester encodings when antennas are placed only a few centimeters from each other.

4.2.1.3 Measurements of WBT with Antipodal Vivaldi Antenna

In order to verify WBT at short distance, measurements are presented based on the transmission over 3.6GHz to 4, 6 or 12 GHz frequency range with 8, 12 and 24 points per bit respectively.

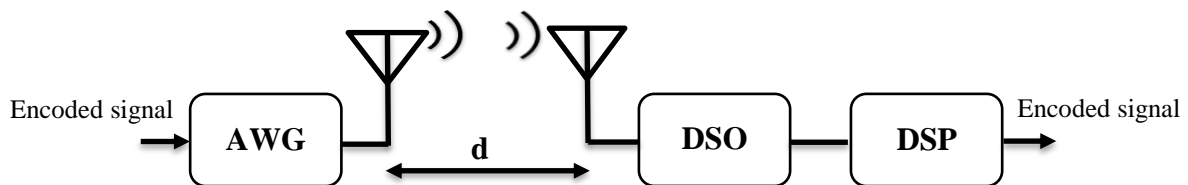


Figure 4.9 Setup of two AVA placed in an aligned configuration for WBT. Encoded signal: Manchester and Polar RZ, AWG: Arbitrary Waveform Generator, DSO: Digital Sampling Oscilloscope, DSP: Digital signal processing (with Matlab).

Two identical AVAs were placed in an aligned configuration to transmit and receive directly digital Polar RZ and Manchester encoded signals without any modulation technique as shown in figure 4.9.

An Arbitrary Wave Generator (Tektronix 7122B AWG, 12-24GS/s, 4.8-9.6GHz) is used as a transmitter and a digital storage oscilloscope (Tektronix DSO TDS6604B, 6GHz, and 20GS/s) is used as a receiver. Manchester and Polar RZ encoded signals at 1Gbps are generated using a computer and are supplied to the AWG, which sends them directly to the emitting antenna at room temperature. The received signals were captured with the DSO with 20GS/s and processed with Matlab to calculate the BER values using two BER techniques.

The transmitting and receiving antennas were oriented with the same polarization so that the same parts of their radiation patterns point at each other. The distance between the closest edges of each AVA has

been varied from 1cm to 15cm as shown in figure 4.8. The lower frequency for the antipodal Vivaldi antennas is 3.6 GHz, as observed in chapter 3.

In this section, simulations and measurements are also compared. The simulations are based on measured S-parameters. BER obtained for simulations and measurements use the same input data signals. Also with the smaller AVAs, BER were estimated for three different random digital input signals for the purpose of confirming the WBT performance measurements.

BER values were estimated for Manchester and Polar RZ encodings sampled with 8 points per bit of digital input signal at a data rate of 1Gbps using 20 and 1000-bit code patterns. Non-zero BER are observed with all bit code patterns, because the spectrum of digital input signal is mostly outside the bandwidth of AVA antennas (3.6 up to 12GHz): indeed the spectrum is 0-4GHz with 8 samples per bit as shown in figure 4.10. The transmitted bandwidth of 3.6 to 4 GHz does not carry enough information for recovering correctly the input signal.

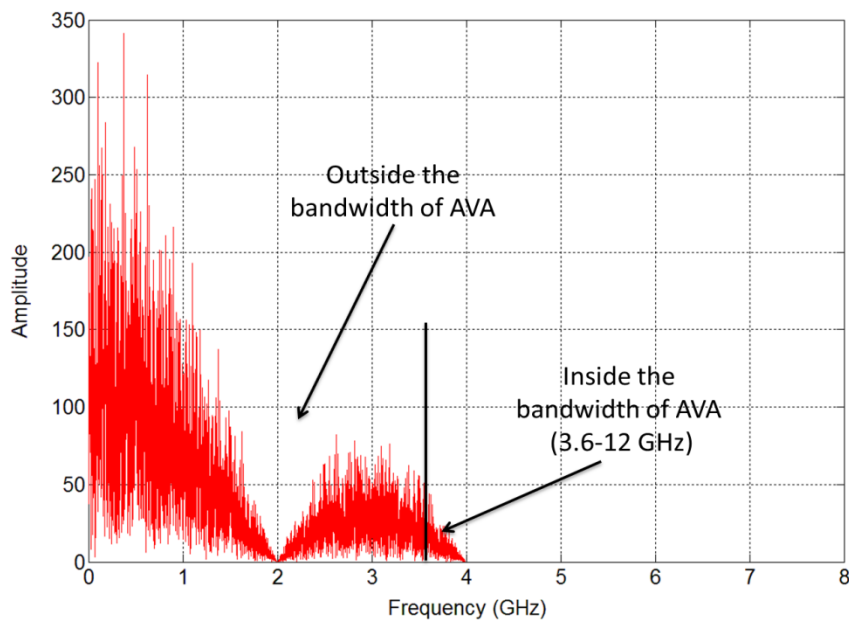


Figure 4.10 Simulated spectrum of Polar RZ line code at a data rate of 1Gbps with 8 samples per bit.

4.2.1.3.1 Comparison of simulations and measurements for WBT with Polar RZ encoding

A 20 bit-code pattern signal [bit stream = 10110110110001011001] fabricated with 12 points per bit has been generated at a data rate of 1Gbps with Polar RZ line encoding and propagated between antennas separated by distance from 1cm to 15cm. The received signals were captured by the DSO (20 points per bit) and processed with Matlab to calculate the BER using the two techniques described in chapter 2 (section 2.5).

Figure 4.11 shows measurements of WBT of a Polar RZ encoded signal at data rate of 1Gbps using 12 points per bit and 20-bit code pattern. The output digital signal agrees well with the input signal for distances of 2, 4 and 8cm. The measurement of WBT output signal allows to identify correctly the input signal.

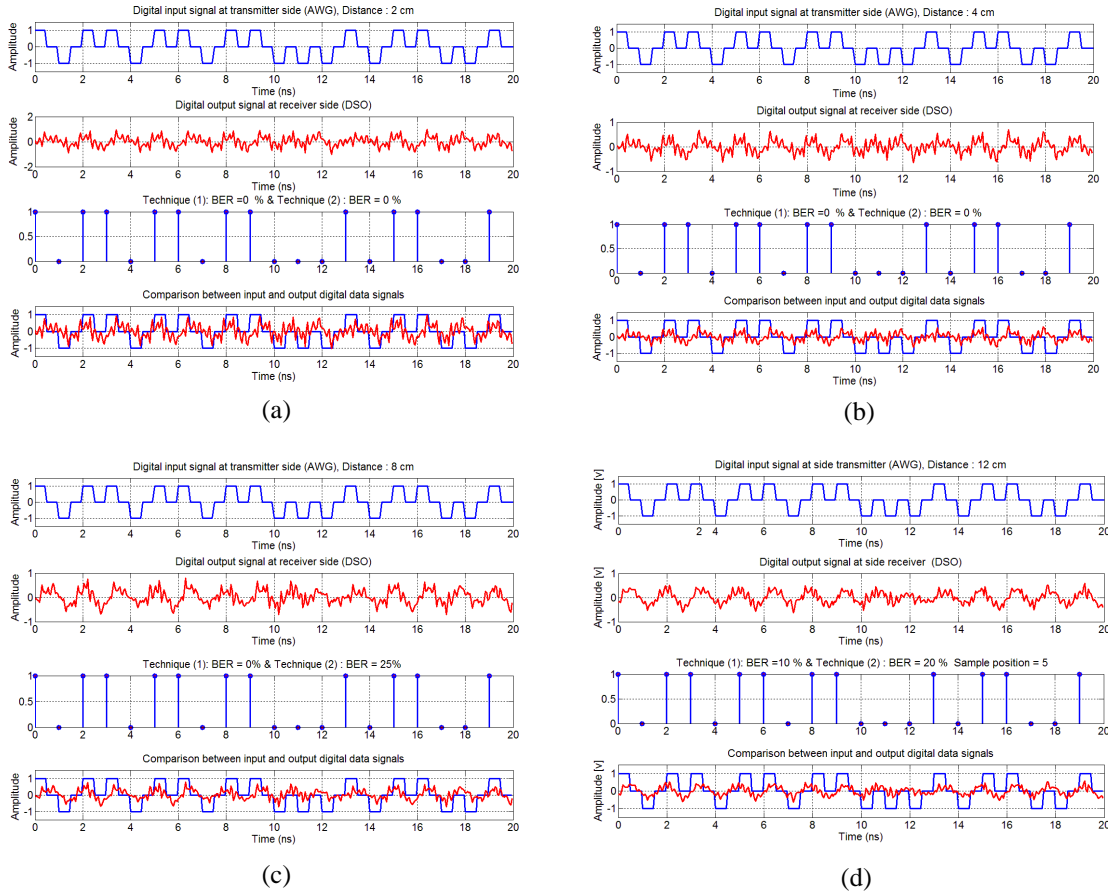


Figure 4.11 Measured 20-bit Polar RZ encoded signal at a data rate of 1Gbps with 12 points per bit for different distances between antennas: (a) $d = 2\text{cm}$. (b) $d = 4\text{cm}$. (c) $d = 8\text{cm}$. (d) $d = 12\text{cm}$.

In order to make this wireless baseband transmission closer to real conditions of operation, the measurements and simulations were done using two different random input signals with 20- and also 1000-bit streams with the same data rate of 1Gbps and 12 points per bit.

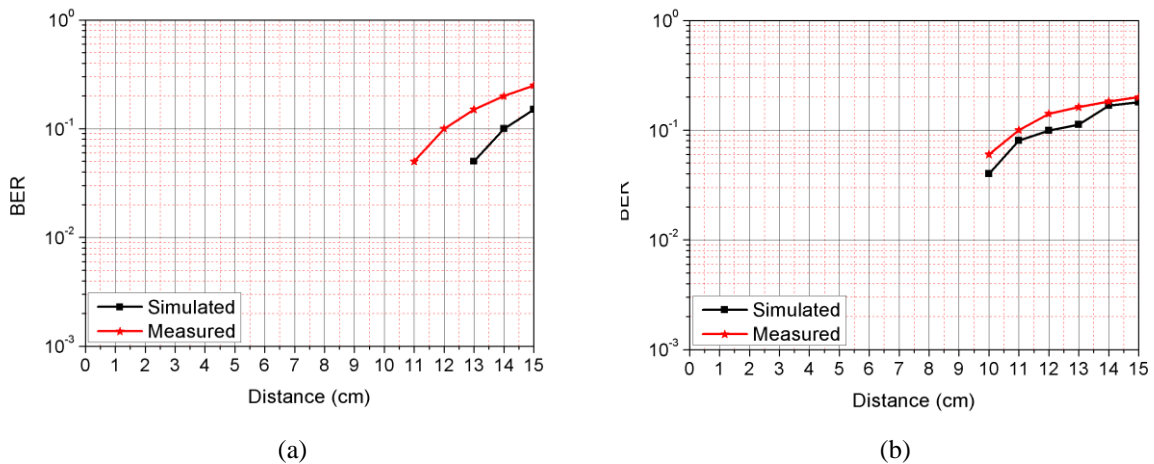


Figure 4.12 Measured and simulated BER of Polar RZ encoding versus distance from 1cm to 15cm at a data rate of 1Gbps using two different random input signals for 20 and 1000-bit code patterns with 12 points per bit. (a) With a 20-bit code pattern. (b) With a 1000-bit code pattern.

The available storage of the DSO limits the maximum number of bits. Figure 4.12 shows a comparison of BER values simulated and measured versus distance from 1cm to 15cm for Polar RZ encodings using two different random input signals at a data rate of 1Gbps for 20 and 1000-bit code patterns with 12 samples per bit. In order to verify the accuracy of the first results, additional measurements based on 24 points per bit instead of 12 points per bit are presented in figure 4.13 with the same input data rate of 1Gbps. In this measurement, the interleaved option of the AWG (24SG/s data rate) was used to select 24 points per bit. The spectrum range is 0-12 GHz which means that the upper frequency of the FFT increases, therefore more energy and more bandwidth are captured by the DSO. Figure 4.14 shows a comparison of BER values versus distance from 1cm to 15cm for Polar RZ encoding at a data rate of 1Gbps using 1000-bit code pattern with 12 and 24 points per bit. Due to the increase of the captured bandwidth, BER decreases when more samples are taken, for a given data rate. This indicates that the number of samples per bit plays an important role in this communication system. Also, BER increases when the code pattern comprises these bits, which is a statistical artefact associated to the accuracy of the measurement. The experiments showed that wireless baseband transmission is realisable when using antennas with a linear phase characteristic and broadband under short distance condition.

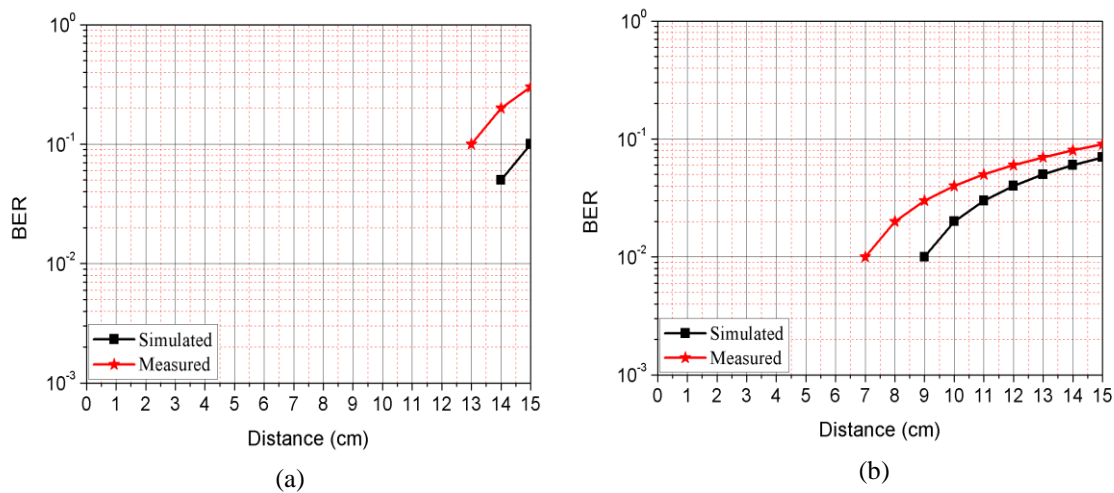


Figure 4.13 Measured and simulated BER of Polar RZ encoding versus distance from 1cm to 15cm at a data rate of 1Gbps for 20 and 1000-bit code patterns with 24 samples per bit. (a) With a 20-bit code pattern. (b) With a 1000-bit code pattern.

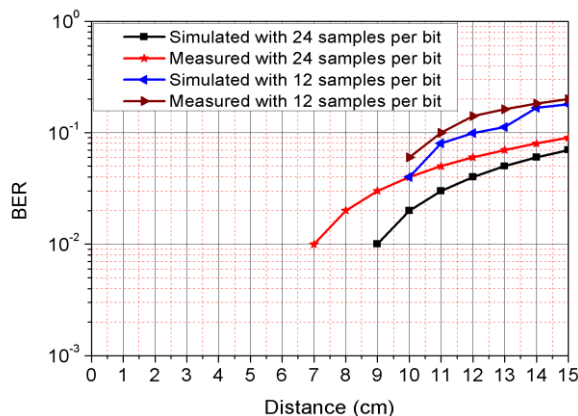


Figure 4.14 Measured and simulated BER for Polar RZ encoding versus distance antennas at a data rate of 1Gbps using 1000-bit code pattern with 12 and 24 points per bit.

4.2.1.3.2 Comparison of simulations and measurements for WBT with Manchester encoding

In the previous section, we have shown the performance of Polar RZ encoding to send and receive digital data signal at short distance and data rate of 1Gbps. In this section, the Manchester encoding performance for WBT is studied with the same procedure and steps.

A 20 bit-code pattern signal [bit stream = 10110110110001011001] fabricated with 12 points per bit has been generated at a data rate of 1Gbps with Manchester line encoding.

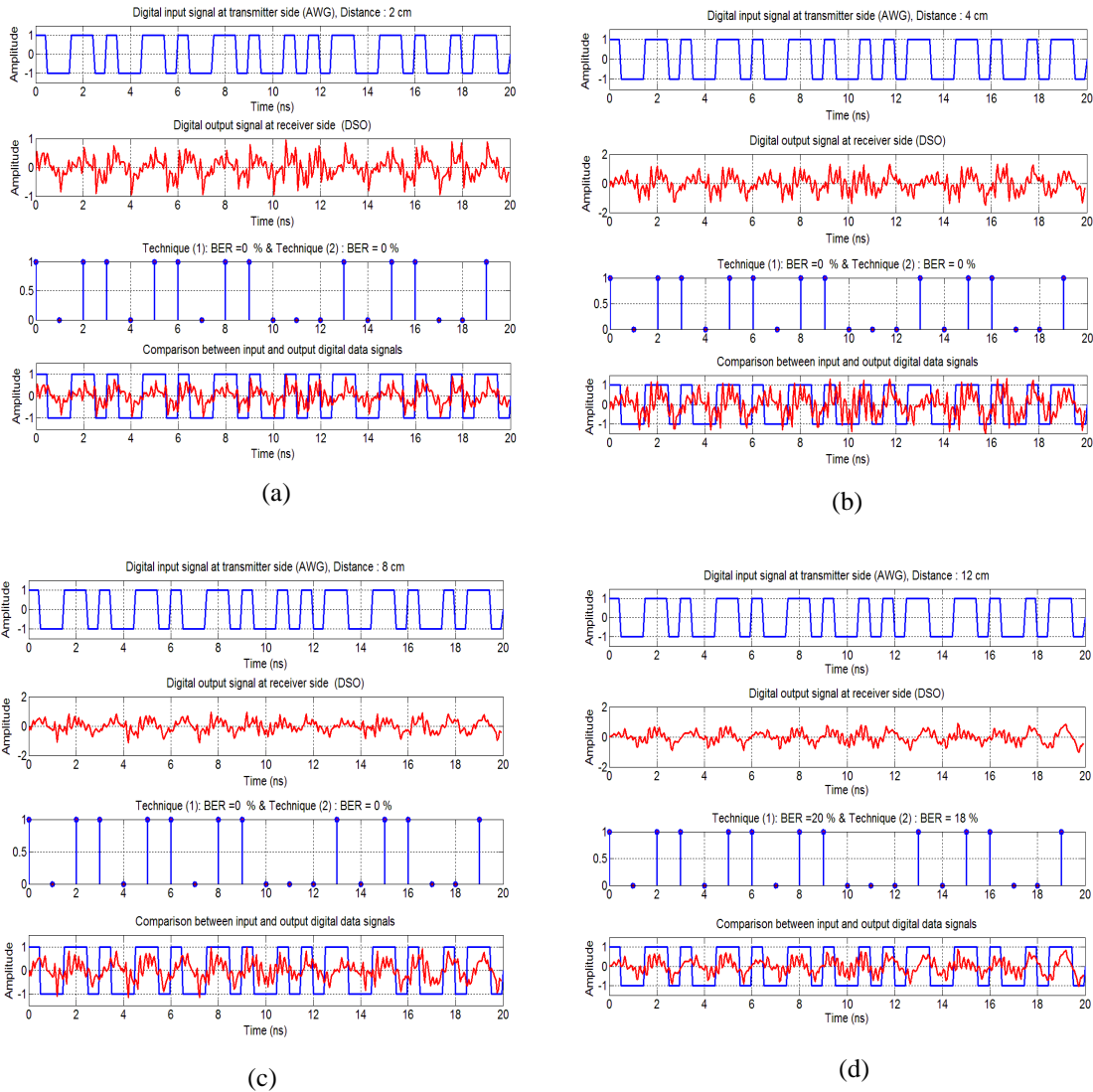


Figure 4.15 Measured transmission of a Manchester encoding at a data rate of 1Gbps with 12 points per bit for a 20-bit code pattern and different distances between antennas: (a) $d=2\text{cm}$. (b) $d=4\text{cm}$. (c) $d=8\text{cm}$. (d) $d=12\text{cm}$.

Figure 4.15 shows measurements of WBT for a 20-bit Manchester encoded signal at a data rate of 1Gbps using 12 points per bit. The digital output signal agrees well with the input signal when the distance is lower than 8cm.

Figure 4.16 shows a comparison of simulation and measurement BER values versus distance from 1cm to 15cm for Manchester encoding at a data rate of 1Gbps for 20 and 1000-bit code patterns with 12 points per bit.

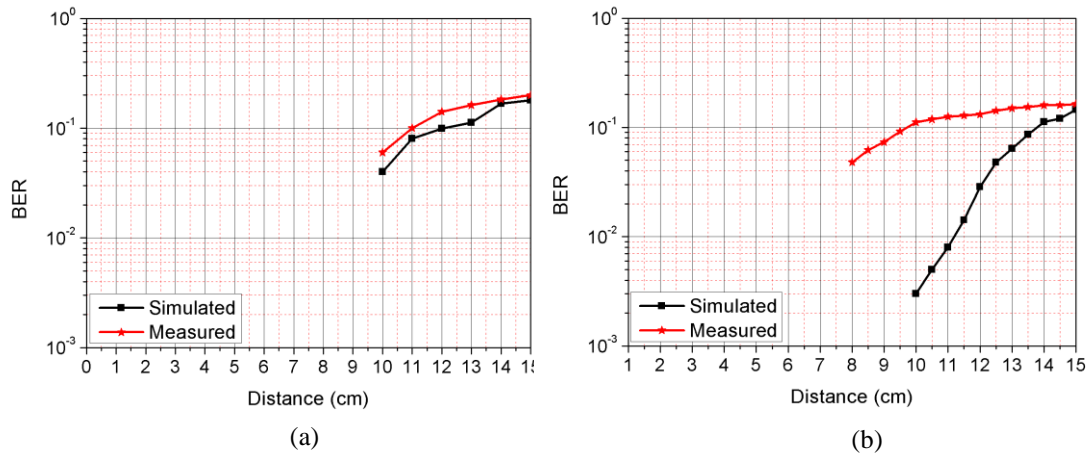


Figure 4.16 Measured and simulated BER of Manchester encoding versus distance at a data rate of 1Gbps using two different random input signals with 12 points per bit. (a) With a 20-bit code pattern. (b) With a 1000-bit code pattern.

A zero BER is observed with a 20-bit code pattern when the distance between antennas is less than 10cm for both simulations and measurements while zero BER is obtained with 1000-bit code pattern when the distance is less than 10cm and 8cm for simulation and measurement respectively. A similar study has been done with 24 points per bit. Results are compared with the ones at 12 points per bit in figure 4.17.

Figure 4.18 shows a comparison of BER values versus distance for Manchester encoding at a data rate of 1Gbps using 1000-bit code pattern with 12 and 24 points per bit.

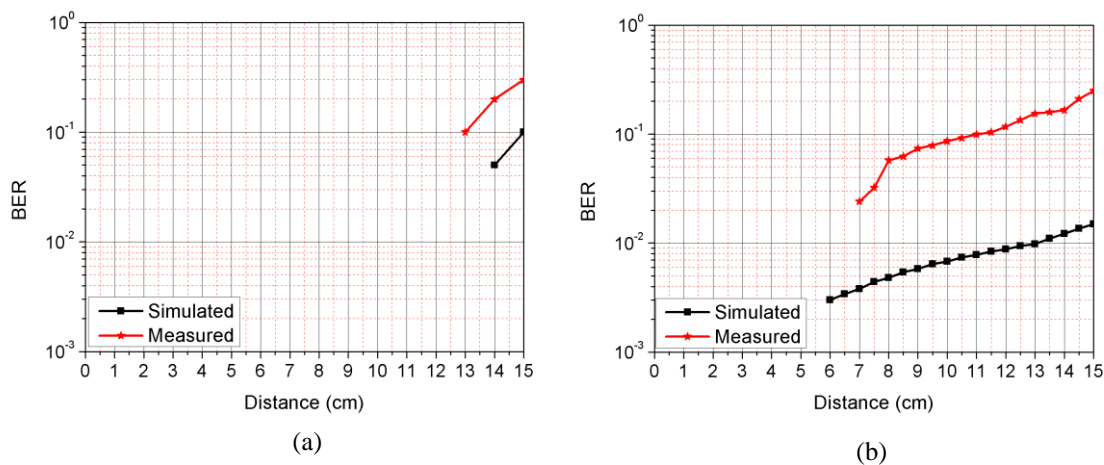


Figure 4.17 Measured and simulated BER of Manchester encoding versus distance at a data rate of 1Gbps with 24 points per bit. (a) With a 20-bit code pattern. (b) With a 1000-bit code pattern.

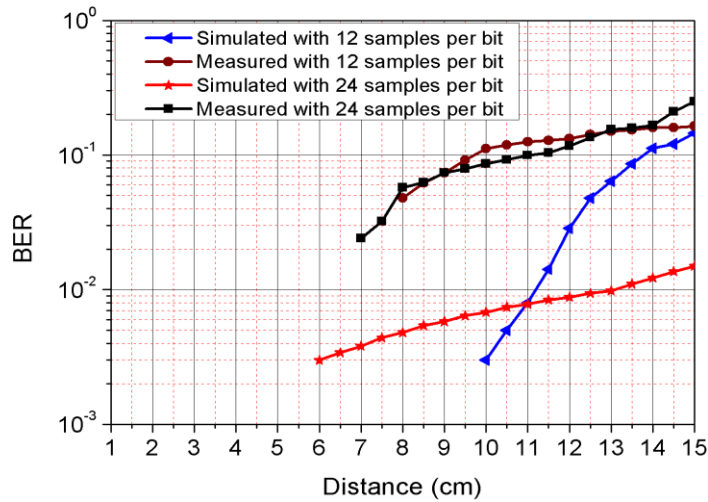


Figure 4.18 Measured and simulated BER for Manchester encoding versus distance between antennas at a data rate of 1Gbps using 1000-bit code pattern with 12 and 24 points per bit.

In order to verify the performance of WBT at data rates higher than 1Gbps, BER values with 12 samples per bit for Manchester and Polar RZ encodings were measured at a data rate of 2Gbps using 20 and 1000-bit code patterns with the same procedure as before. Zero BER values are observed for distances lower than 2cm with 1000-bit code patterns for both line codes while simulations, shown in figures 4.7(a), show zero BER for distances lower than 7cm.

From these results one can conclude that two small broadband antennas with a linear phase characteristics placed at a short distance from each other are a practical solution for WBT with Manchester and Polar RZ encodings at a data rate of 1Gbps. After wireless transmission, the signal at 1Gbps needs to be divided to packages so that the package signal can be processed at the output side.

4.2.2 Monopole UWB antennas for WBT

In this section, small omni-directional antennas are considered in order to verify the performance of WBT with the same data rate and code pattern for Manchester and Polar RZ encodings.

The transmitting and receiving antennas were oriented with the same polarization so that the same parts of their radiation patterns point at each other. The distance between the closest edges of each monopole antenna has been varied from 1cm to 10cm as shown in figure 4.19. The same Arbitrary Wave Generator (Tektronix 7122B AWG, 12-24GS/s, 4.8-9.6GHz) is used as a transmitter and a digital storage oscilloscope (Tektronix DSO TDS6604B, 6GHz) is used as a receiver. Manchester and Polar RZ encoded signals at 1Gbps are generated using a computer and are supplied to the AWG, which sends them directly to the emitting antenna.



Figure 4.19 Setup with two monopole antennas placed face to face in short distance configuration.

A 20-bit code pattern signal [bit stream = 10110110110001011001] fabricated with 12 points per bit has been generated at a data rate of 1Gbps for Manchester and Polar RZ line codes.

The received signals were captured with the DSO (20GS/s) and processed through Matlab to calculate the BER using the two techniques described in 2.5 (chapter 2). Figure 4.20 shows that the output signal is detected correctly.

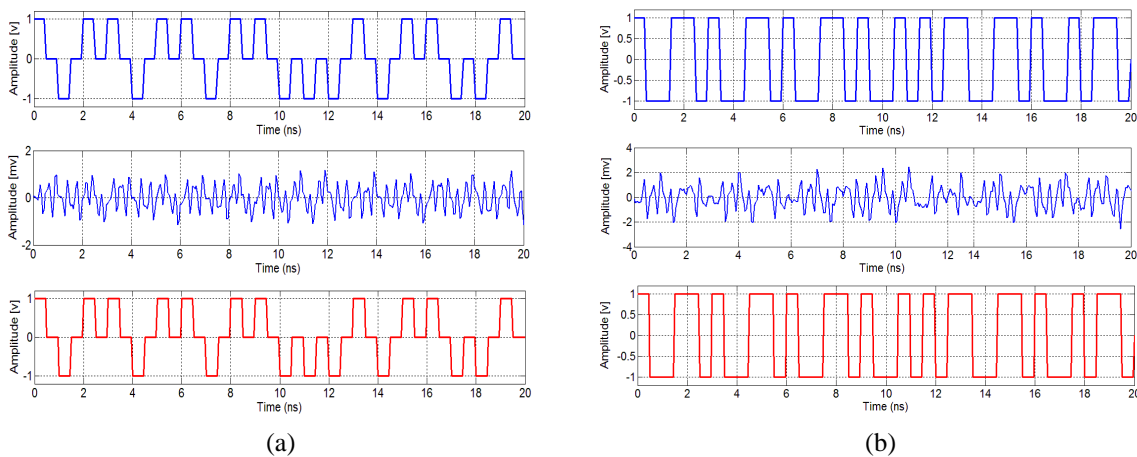


Figure 4.20 Measured transmission of two different line codes with two monopole antennas placed face to face at $d = 4\text{cm}$ with 20 bit-code pattern and 12 points per bit at an input rate of 1Gbps. (a) Polar RZ encoding with input data from AWG, output measured by the DSO (20 points per bit), and detection results after Matlab processing. (b) Same curves for Manchester encoding.

To make this wireless baseband transmission closer to real conditions of operation, the measurements were also done with a 500- and 1000-bit streams with the same data rate of 1Gbps. In these cases the available storage of DSO is limited to reach higher number of bits.

Figure 4.21 shows a comparison of BER values for 20, 500 and 1000-bit code patterns. Non-zero BER values are observed when the distance between antennas is higher than 5cm for both line codes. Below 5cm no transmission error is detected because of the exponential decay of BER with distance and of the limited experimental number of bits.

From these results one can conclude that two broadband antennas with a linear phase characteristics placed at a short distance from each other are suitable for WBT with the Manchester and Polar RZ encodings.

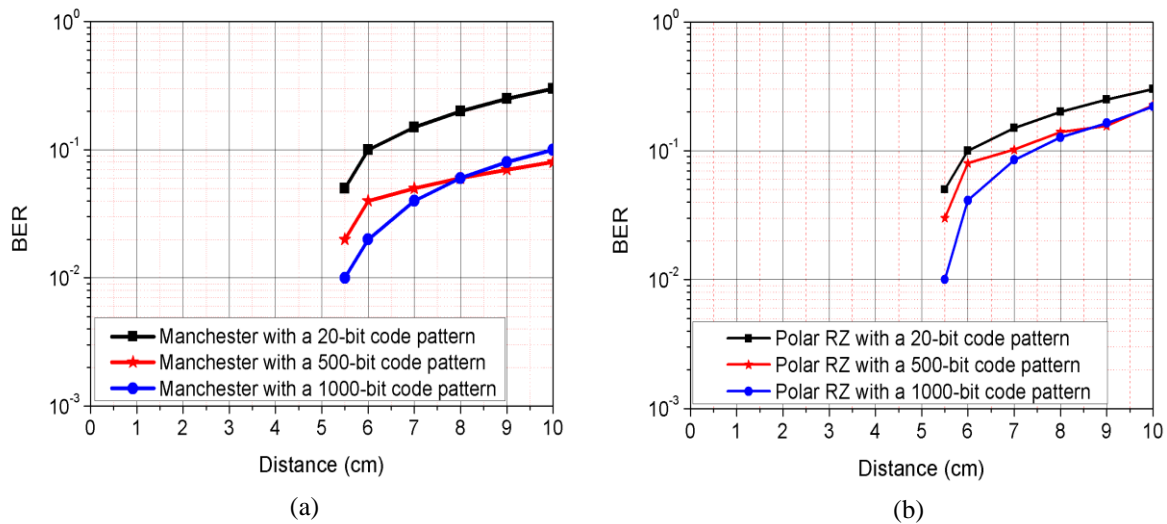


Figure 4.21 Measured BER for (a) Manchester and (b) Polar RZ encodings versus distance between antennas at 1Gbps using 20, 500, 1000 bit-code streams and 12-points per bit.

Comparing the results between AVA and monopole antennas for both Manchester and Polar RZ encoded signals we found that the BER is lower with AVA than with monopole antennas for a given distance between antennas. Indeed, the energy is focused in one direction for AVA, while the energy is spread in all directions for monopole antennas.

We also used large antennas to transmit and receive the digital data directly and compare with our antenna results. To do so, the measurement is done with standard large horn antennas by using the same procedure used with AVA and monopole antennas.

4.2.3 Large size horn antenna for WBT

In this section, an experimental study of wireless baseband transmission performance with large size antenna is presented in order to verify WBT performance at distances higher than 15 cm (e.g. mostly in the far field region as shown in figure 4.1(b)) using a pair of SATIMO dual ridge horn antennas of dimensions of 105 x 61 x 104.3 mm and frequency range 2 GHz to 32 GHz. The same Arbitrary Wave Generator (Tektronix 7122B AWG, 12-24GS/s, 4.8-9.6GHz) is used as a transmitter and a digital storage oscilloscope (Tektronix DSO TDS6604B, 6GHz) is used as a receiver in order to radiate at room temperature digital streams as shown in figure 4.22.

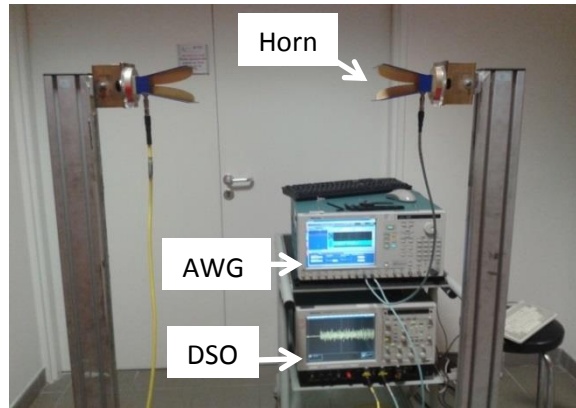


Figure 4.22 Setup with two SATIMO dual ridge horn antennas placed face to face.

The same procedure as before was considered for Manchester and Polar RZ encodings with 12 and 6 points per bit using 20-bit code pattern at a data rate of 1Gbps. Measurements (20GS/s) give no error when the distance is lower than 150cm for both line codes. Also, measurements with 4 samples per bit were done with the same data rate where non-zero BER values were observed for all distances because the bandwidth range with 4 points per bit is 0-2 GHz that is outside the bandwidth range of horn antenna (2-32 GHz).

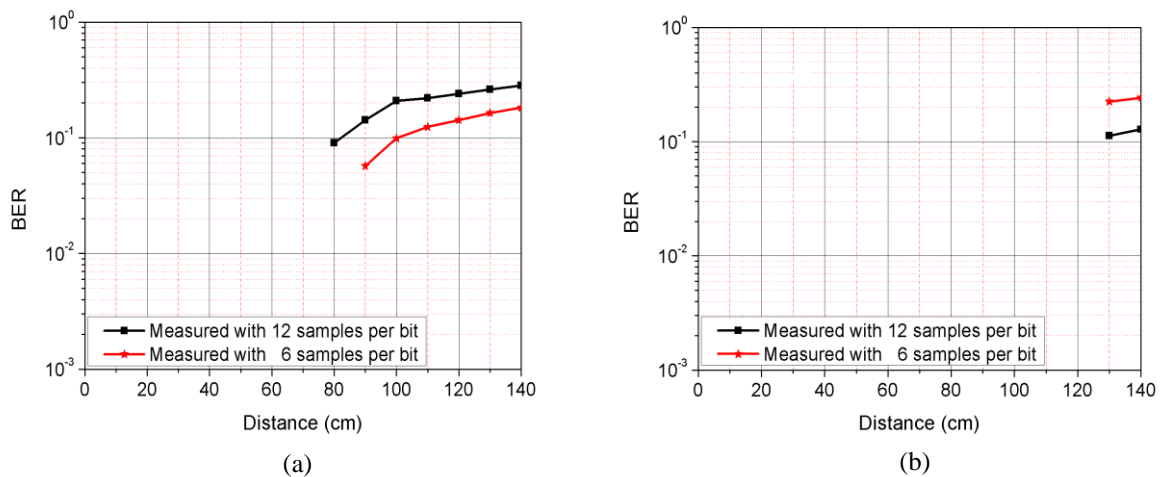


Figure 4.23 Measured BER for (a) Polar RZ and (b) Manchester encodings versus distance between horn antennas at a data rate of 1Gbps with 1000-bit code pattern using 6 and 12 points per bit.

The experimental input data was also made of 1000 random bits with 6 and 12 points per bit at a data rate of 1Gbps for both Manchester and Polar RZ encodings. For such a data rate the antennas under consideration can only transmit half of the second harmonic with 6 samples per bit since the bandwidth is 0-3 GHz, while the bandwidth is 0-6 GHz with 12 samples per bit. For this last case, the second and the third harmonics are transmitted, as mentioned in the chapter 2.

Figure 4.23 shows a comparison of BER values versus distance from 10cm to 140cm for both Manchester and Polar RZ encodings. Measurements give no error when the distance is lower than 130cm for Manchester encoding while there is no error below 80cm for Polar RZ encoding.

4.3 Conclusion

In this chapter, a baseband transmission scheme for wireless communications has been examined using a pair of AVA, monopole and horn antennas for transmission and reception of digital input signals at a data rate of 1Gbps with on a short distance of a few centimeters.

Comparing the results between AVA and monopole antennas for Manchester and Polar RZ encoded signals, the BER is lower with AVA than with monopole antennas for a given distance between antennas. Indeed, the energy is focused in one direction for AVA, while the energy is spread in all directions for monopole antennas.

In order to compare the first WBT measurements, large horn antennas have been proposed to overcome the lower limited bandwidth of AVA and monopole antennas with a broader bandwidth range from 2 to 32 GHz. Based on the same procedure used with antipodal Vivaldi and monopole antennas, wireless baseband transmissions were done when using an antenna with a linear phase characteristic over broadband range.

When we compare the two encoding schemes, we found that the BER for Manchester encoding is lower than the BER for Polar RZ encoding for a given distance between antennas. Because a long stream of 1s or 0s would not change state as much Polar RZ encoding (successive identical code pattern are generated for a long time such as “11111” or “00000”) where the Manchester encoding have a transition in middle of the bit time, so there are more transition of the bit, therefore a receiver could find that transition and lock on to the signal again.

For small size antennas with a linear phase characteristic over a given band and with appropriate encodings, wireless baseband transmission is realisable at a data rate of 1Gbps and more under short distance condition. Therefore, the two factors playing an important role during design of the WBT system are the choice of the antenna types and the choice of transmission code.

These results have been published in:

F. Abayaje and P. Febvre, “A small size Monopole UWB Antenna Used for Short Distance Wireless Baseband Transmission at High Data Rate,” Proc. International Workshop on Antenna Technology conference, Athens, 1-3 March 2017.

5 Conclusions and prospects

Some systems that require fast processing at clock rates above 20 GHz rely on superconducting digital circuits to process the signals. For such circuits, which are cooled at the temperature of liquid helium, the processed data need to be transferred at room-temperature for further processing.

This thesis deals with the study of wireless baseband transmission of Manchester and Polar RZ encoded digital signals directly through a set of antennas. The emitting and receiving antennas are placed at short distance from each other and data rate has been chosen equal to 1Gbps and 2Gbps. We found that when using an antenna with a linear phase characteristic over a given band and an appropriate encoding signal, the wireless baseband transmission is doable to transmit digital signals from a cryogenic environment.

The thesis elaborates on four crucial issues for WBT:

- ❖ Polar RZ and Manchester encodings have been proposed, after comparison of features.
- ❖ The transfer functions of the antenna system have been estimated. Simulations of the transmission of digital input data directly through a set of two antennas have been done based on different approaches: the transmission of the first harmonic or transmission of higher harmonics of digital input signals. Techniques to retrieve the input signal pattern from the measurement of the output signals have been developed to estimate the BER values and improve the quality of the transmission of digital signals.
- ❖ Monopole and antipodal Vivaldi antennas have been designed, simulated and fabricated on 1.6 mm-thick FR4 substrate. They feature omni- and one-directional radiation patterns respectively.
- ❖ S-parameters of an emitter-receiver antenna system based on a pair of small AVAs have been measured to determine the maximum distance with zero BER. A baseband transmission scheme for wireless communications has been examined using a pair of AVA, monopole and horn antennas for transmission and reception of digital input signals at data rates of 1 and 2Gbps over a short distance.

In our application, the distance between the two environments is 2cm. In practice we observed non-zero BER values based on measured S-parameters and WBT on distances longer than 2cm. The number of samples per bit and the line code choice play an important role in this wireless baseband transmission communication system when small size antennas are placed a few centimeters from each other.

Future work allocated to this thesis deals with:

This thesis was focused on WBT and the development of appropriate simulations. The simulations allowed improvements of both simulated and measured results. In this context, additional work is still needed:

- Higher data rates: this study depends on the number of points per bit. We can transmit higher data rate (3-10Gbps), but this requires more sophisticated equipment, including higher sampling rate and also a higher memory depth.
- Wireless baseband transmission over a short distance with small size antennas has been demonstrated at room temperature at 1Gbps and 2Gbps. Therefore, in the future, we intend to investigate the performance characteristics of this transmission scheme in different environments, the wireless baseband transmission performance between the cryogenic stage at the temperature of liquid helium and the outer part of the cryogenic system at room temperature is the next step in this direction.
- Multi input multi output (MIMO) communication system using WBT scheme. Based on this idea, MIMO systems will bring us an advantage of a significant increase of WBT performance between the two environments.
- Develop an appropriate model perform more accurate BER estimations by simulation. It is difficult to construct instruments to measure the BER of WBT system. Simulation is easy compared to measurement. In addition, we will investigate even better encoding schemes for WBT and also improve our AVA or use other antenna types.

APPENDIX A: Power Spectral Density (PSD) of line codes

Each line code is described by a symbol mapping function a_k and the pulse shape $p(t)$.

Symbol mapping function (a_k) are unipolar, polar, bipolar. And pulse shape $p(t)$ are NRZ, RZ, and Manchester....

In this appendix, the PSD of two encodings (Manchester and Polar RZ line codes) are presented.

❖ **The polar RZ, a_k is:**

$$\text{for 1's} \quad a_k = \begin{cases} +A & 0 \leq t \leq T_b/2 \\ 0 & T_b/2 \leq t \leq T_b \end{cases}$$

$$\text{for 0's} \quad a_k = \begin{cases} -A & 0 \leq t \leq T_b/2 \\ 0 & T_b/2 \leq t \leq T_b \end{cases}$$

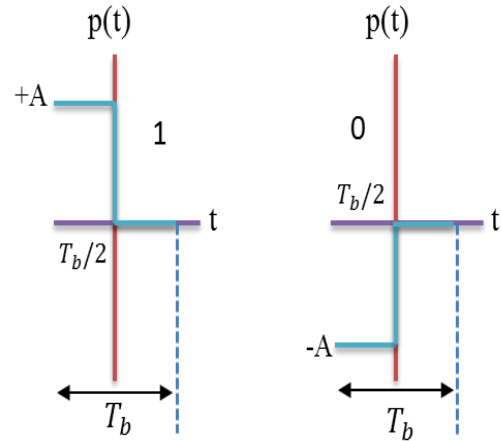


Figure A.1 Pulse shapes of "1" and "0" for Polar RZ line code.

where: T_b is bit duration, A is the amplitude

The rectangular function in the general case is:

$$\Pi = \frac{t - t_o}{T_b}$$

where t_o the center of the rectangular function and T_b is the duration of the bit.

The power spectrum density of the line code is defined as:

$$G(f) = |P(f)|^2 S(f) \tag{A.1}$$

where $P(f)$ is the Fourier transform of the pulse shape and $S(f)$ is the PSD of a digital sequence of (a_k)

$$S(f) = \frac{1}{T_b} \sum_{n=-\infty}^{\infty} R_a[n] e^{-i2\pi f n T_b} \tag{A.2}$$

$$R_a[n] = R(k) = \sum_{i=1}^I (a_n a_{n+k})_i P_i \tag{A.3}$$

where:

$R_a[n]$ is the autocorrelation function of data.

a_n and a_{n+k} are the level of the pulses at the n th and $(n + k)$ th instants.

P_i is the probability of having the i th $a_n a_{n+k}$ product, considering all possible digital values of (a_n) .

$$G(f) = \frac{|P(f)|^2}{T_b} \sum_{n=-\infty}^{\infty} R_a[n] e^{-i2\pi f n T_b} \quad (\text{A.4})$$

For polar RZ:

$$p(t) = \Pi \frac{t}{T_b/2}$$

The Fourier transform of $p(t)$ is:

$$P(f) = \int_{-T_b/4}^{+T_b/4} \Pi \left(\frac{t}{T_b/2} \right) e^{-i2\pi f t} dt = \frac{T_b}{2} \frac{\sin \pi f T_b/2}{\pi f T_b/2} = \frac{T_b}{2} \text{sinc}(f T_b/2) \quad (\text{A.5})$$

At $k=0$

$$R(0) = \sum_{i=1}^2 (a_n)^2 P_i = A^2 \frac{1}{2} + (-A)^2 \frac{1}{2} = A^2 \quad (\text{A.6})$$

At $k \neq 0$

$$R(k) = \sum_{i=1}^4 (a_n a_{n+k}) P_i = A^2 \frac{1}{4} - A^2 \frac{1}{4} - A^2 \frac{1}{4} + A^2 \frac{1}{4} = 0 \quad (\text{A.7})$$

Then $R(k)$ for polar RZ is equal to:

$$R(k) = \begin{cases} A^2 & \text{when } k = 0 \\ 0 & \text{when } k \neq 0 \end{cases}$$

From equation (A.3) we obtain:

$$G(f) = \frac{1}{T_b} \left[\frac{T_b}{2} \frac{\sin(\pi f T_b/2)}{\pi f T_b/2} \right]^2 \sum_{k=-\infty}^{\infty} R(k) e^{-i2\pi f k T_b} \quad (\text{A.8})$$

$$G(f) = \frac{T_b^2}{4T_b} \text{sinc}^2 \left(\frac{f T_b}{2} \right) * A^2 \quad (\text{A.9})$$

Finally, the PSD equation for the polar RZ is:

$$G(f) = \frac{A^2 T_b}{4} \text{sinc}^2(f T_b / 2) \quad (\text{A.10})$$

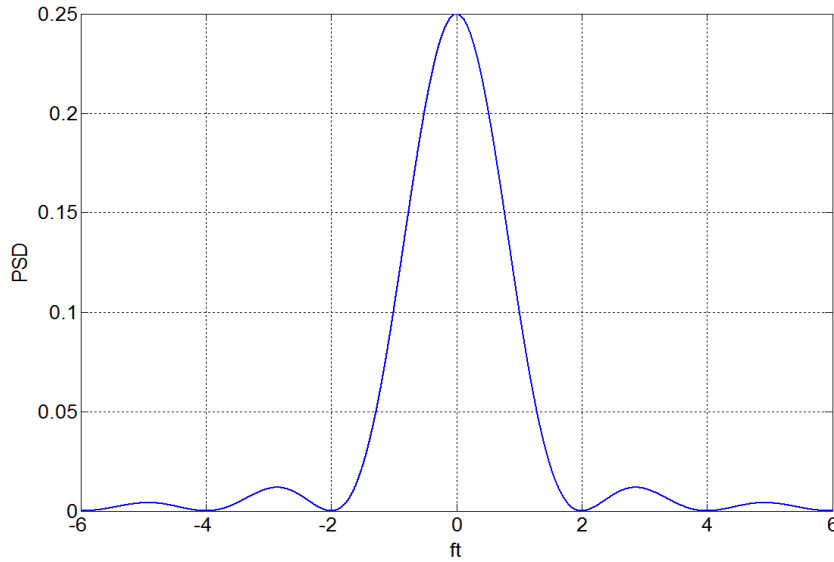


Figure A.2 Power spectrum density versus normalized frequency for the Polar RZ line code where t is the duration of bit. PSD value is different from 0 at dc frequency (there is a dc-component).

❖ For Manchester encoding, a_k is:

for 1's

$$a_k = \begin{cases} +A & 0 \leq t \leq \frac{T_b}{2} \\ -A & \frac{T_b}{2} \leq t \leq T_b \end{cases}$$

for 0's

$$a_k = \begin{cases} -A & 0 \leq t \leq \frac{T_b}{2} \\ +A & T_b \leq t \leq \frac{T_b}{2} \end{cases}$$

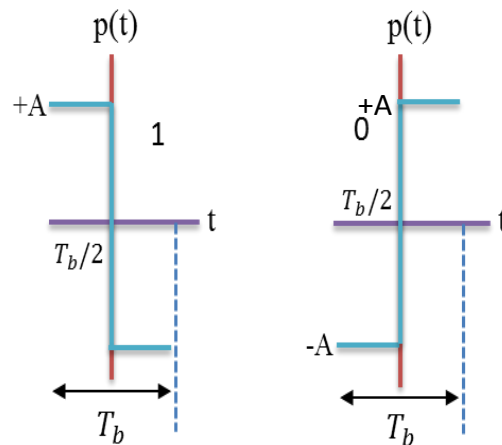


Figure A.3 Pulse shapes of "1" and "0" for Manchester line code.

Manchester code refers to the combination of a Manchester pulse with polar mapping. Then, the impulse response to the Manchester code is:

$$p(t) = \Pi\left(\frac{t + T_b/4}{T_b/2}\right) - \Pi\left(\frac{t - T_b/4}{T_b/2}\right) \quad (\text{A.11})$$

$$P(f) = \frac{T_b}{2} \text{sinc}\left(\frac{fT_b}{2}\right) e^{\frac{+i2\pi fT_b}{4}} - \frac{T_b}{2} \text{sinc}\left(\frac{fT_b}{2}\right) e^{\frac{-i2\pi fT_b}{4}} \quad (\text{A.12})$$

$$P(f) = \frac{T_b}{2} \text{sinc}\left(\frac{fT_b}{2}\right) \left(e^{\frac{+i2\pi fT_b}{4}} - e^{\frac{-i2\pi fT_b}{4}} \right) \quad (\text{A.13})$$

$$P(f) = \frac{T_b}{2} \text{sinc}\left(\frac{fT_b}{2}\right) * 2i \sin\left(\frac{2\pi fT_b}{4}\right)$$

$$|P(f)|^2 = T_b^2 \text{sinc}^2\left(\frac{fT_b}{2}\right) \sin^2\left(\frac{\pi fT_b}{2}\right) \quad (\text{A.14})$$

$S(f) = \frac{1}{T_b} A^2$ like for polar RZ. Finally the PSD equation of the Manchester is:

$$G(f) = A^2 T_b \text{sinc}^2\left(\frac{fT_b}{2}\right) \sin^2\left(\frac{\pi fT_b}{2}\right) \quad (\text{A.15})$$

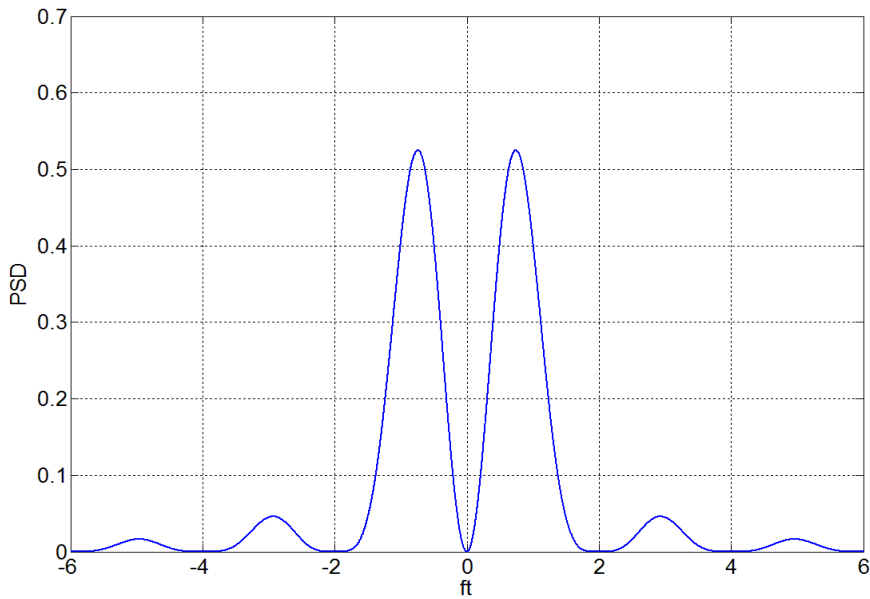


Figure A.4 Power spectrum density versus normalized frequency for the Manchester line code where t is the duration of bit. There is no dc-component.

APPENDIX B: A compact Antipodal Vivaldi Antenna (AVA)

B.1 Design of antipodal Vivaldi antenna

The antenna is designed on a FR4 substrate with a thickness $h=1.6$ mm, a dielectric constant $\epsilon_r = 4.4$, and a dielectric loss tangent $\delta = 0.02$. The antenna consists of an antipodal Vivaldi architecture with one slot resonator. The broadband range is improved by the presence of the slot and by shifting the ground plane with respect to the input port. The area of the antenna is 150 mm^2 ($50L*30W$). It includes two main parts: a feed line and radiation flares. The shape of the flares was chosen to be elliptical. This configuration presents interesting broadband characteristics, due to the smooth transition between the radiation flares and the feeding line. It is one of the optimal curvatures.

The upper frequency limit of a Vivaldi antenna is infinite in theory. The lower frequency limit can be calculated from and depends mainly on the width of the antenna and of the effective dielectric constant ϵ_{eff} .

The antenna has been designed for a broadband range from 2.5 GHz to more than 12 GHz with an input impedance $Z_0=50 \Omega$, equal to the impedance of the feeding coaxial cable. Dimensions of the antenna have been optimized with the HFSS software. The antenna is fed by a microstrip line with a width of 2.5 mm. To increase the low frequency performances, a slot has been added on the ground plane at a suitable position and a shift of the ground plane from the input connector edge was realized.

The slot and the length of the shift are the key control parameters for the impedance bandwidth in the lower frequency band and were optimized to obtain the best behavior of the antenna in the range 2.5-12 GHz. The layout of AVA is shown in figure B.1.

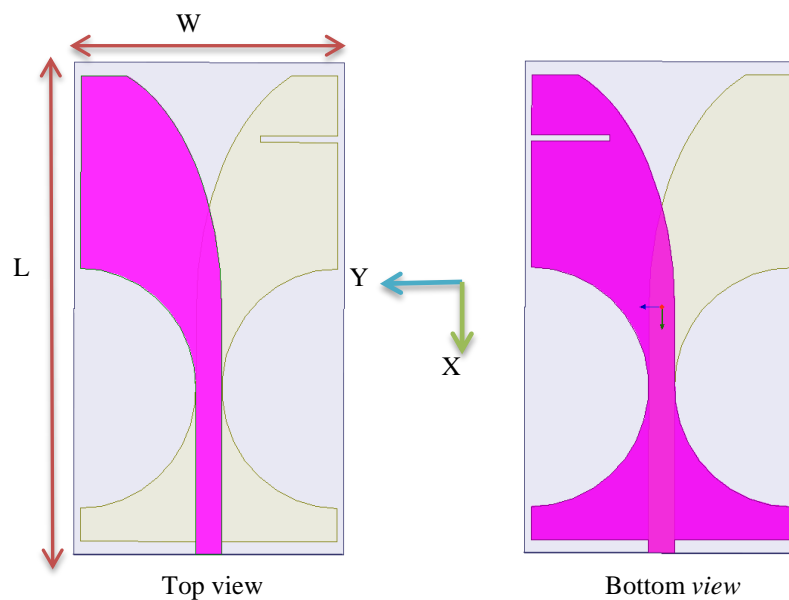


Figure B.1 Layout of the proposed Vivaldi antenna. The total area $L*W$ is $50*30 \text{ mm}^2$ with a FR4 substrate thickness $h=1.6$ mm.

B.2 Simulations and measurements

Compared to other Vivaldi antennas, our design differs by the modification of the ground plane line and by the addition of a slot to the antenna. The use of a slot to lengthen the excited surface current on the radiation elements can also be applied to the ground plane. It will significantly improve the antenna bandwidth.

B.2.1 Voltage Standing Wave Ratio (VSWR) and Antenna Gain

The VSWR provides an estimation of the matching of a given antenna with its environment. Therefore the return loss has to be smaller than 2 across the entire spectrum (2.5-12 GHz). The simulation result presented in figure B.2, clearly shows that the simulated VSWR for this antenna is lower than 2 over the entire frequency range (2.5 GHz to more than 12 GHz). Simulated peak gain over the desired band of the proposed AVA versus frequency is plotted in figure B.2. The peak gain varies from 0 to 6 dB over the frequency range of operation. The antenna clearly exhibits stable gain in the working band, which makes it very suitable for practical applications.

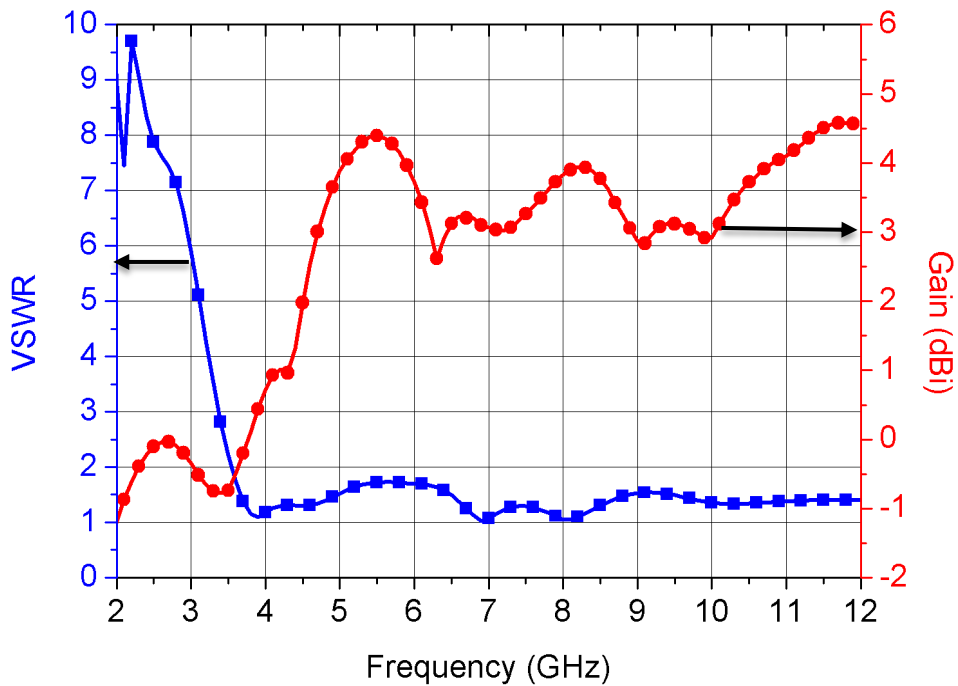


Figure B.2 VSWR and Gain vs frequency for the AVA with a slot resonator and shift ground plane line.

B.2.2 Radiation Patterns and Current Distributions

Simulated radiation patterns of the antenna in the two principal planes: X-Y plane and X-Z plane are presented. The simulated radiation patterns at different resonant frequencies of 2.8, 5.8, 6.8 and 10.8 GHz are shown in figure B.3 (a, b). Gain patterns in X-Y plane and X-Z plane are nearly omnidirectional at $\phi=0$ and bidirectional at $\phi=90$. Figure A.2 (c) shows the gain of the proposed antenna with a slot on a three-dimensional curve at 8 GHz.

The simulated surface current distributions of the proposed antenna at 2.8, 5.8, 6.8, 10.8 GHz, carried out by HFSS V15, are given in figure B.4. We notice that the current distributions at the four resonant frequencies are different. For the first resonance at 2.8 GHz, the surface current is mainly concentrated on the microstrip feed line while at resonant frequencies 5.8, 6.8 and 10.8 GHz, the surface current is concentrated at the microstrip feed line and radiation side. The fabricated antenna is shown in figure B.5. Measurements were performed by using a 37369A Anritsu Vector Network Analyzer.

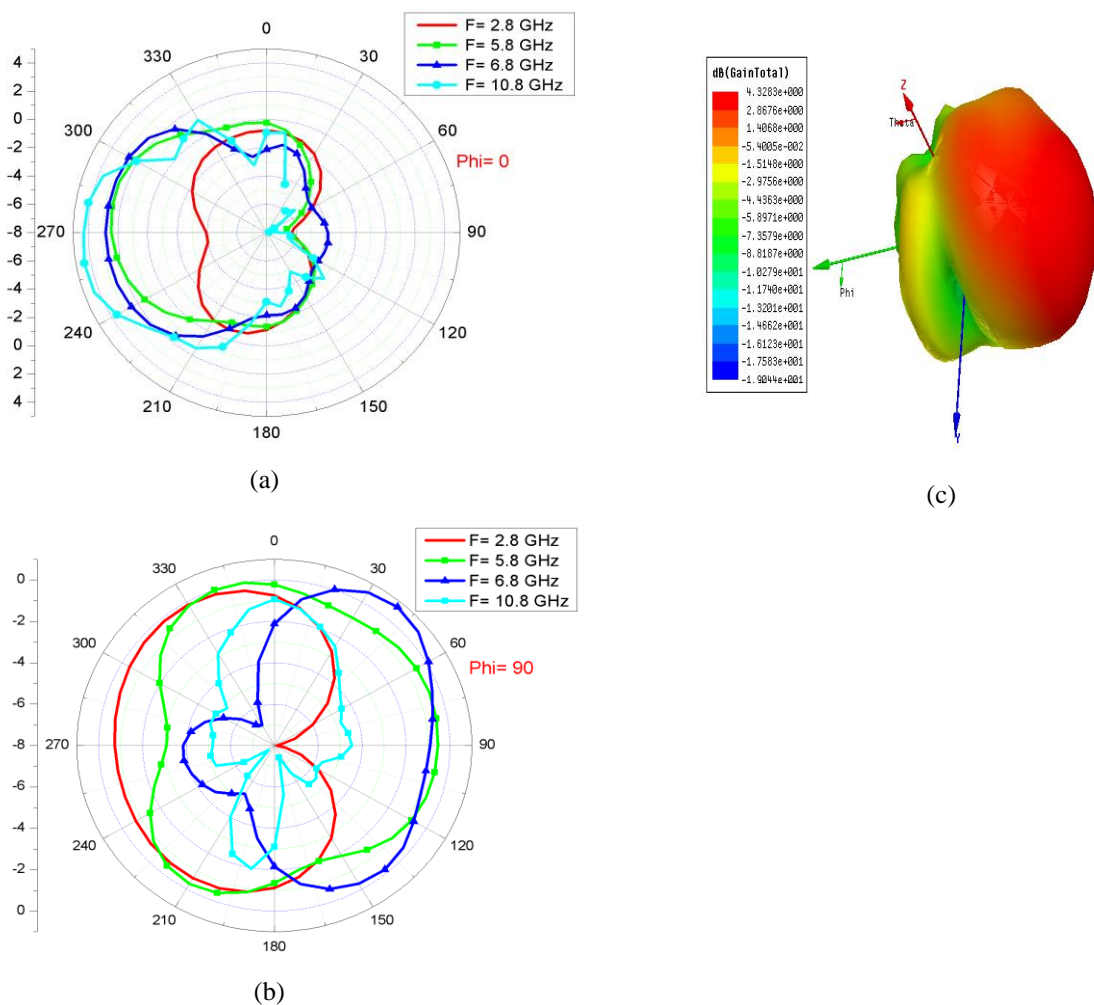


Figure B.3: Simulation Radiation patterns of AVA at frequency range 2.8, 5.8, 6.8, 10.8 GHz. (a) at the $\phi=0$. (b) At the $\phi=90$. (c) 3D curve at 8GHz.

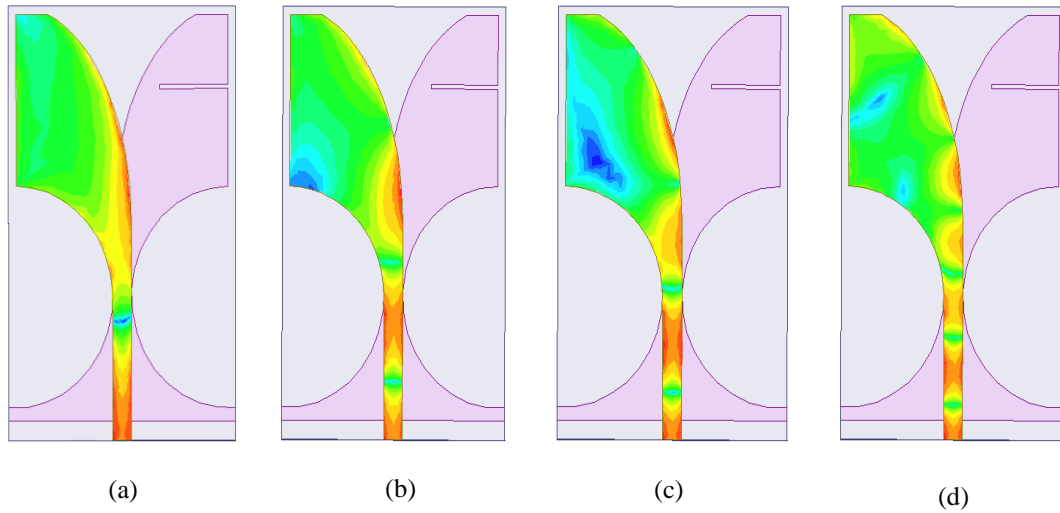


Figure B.4 Simulation of the surface current distribution of the proposed antenna. (a) 2.8 GHz. (b) 5.8 GHz. (c) 6.8 GHz. (d) 10.8 GHz.

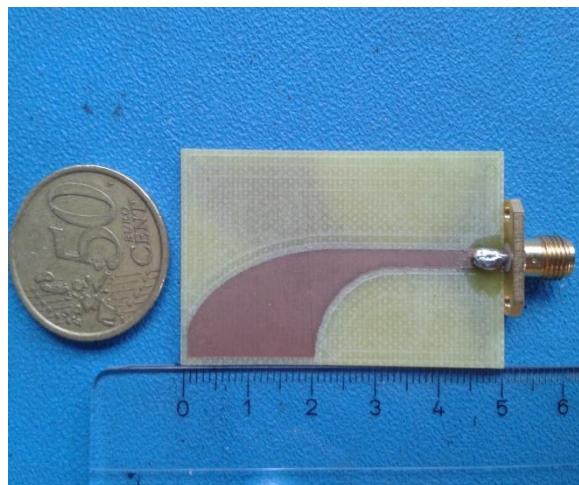


Figure B.5: Photography of the fabricated antipodal Vivaldi antenna.

B.3 Short-distance configuration

The simulated and measured reflection (S_{11}) and transmission (S_{21}) coefficient of the fabricated AVA are presented in figures B.6 and B.7. The two AVA were placed in an aligned configuration with a distance from 1 mm to 3 mm as shown in figure B.8.

Comparing all the curves, simulation results are in reasonable agreement with the measurements. Measured results of S_{21} show a slight shift at lower frequency. The observed difference can be explained by the fact that the HFSS software works with ideal parameters, whereas during the measurements, some external

uncontrolled factors like the connection losses between the printed circuit board and the SMA connector have to be taken into account

Table B.1 summarizes the comparison between the proposed antenna and antennas from literature. The proposed AVA is smaller in dimensions than the antipodal configuration as reported in [4-8 and12] and makes it suitable for broadband applications.

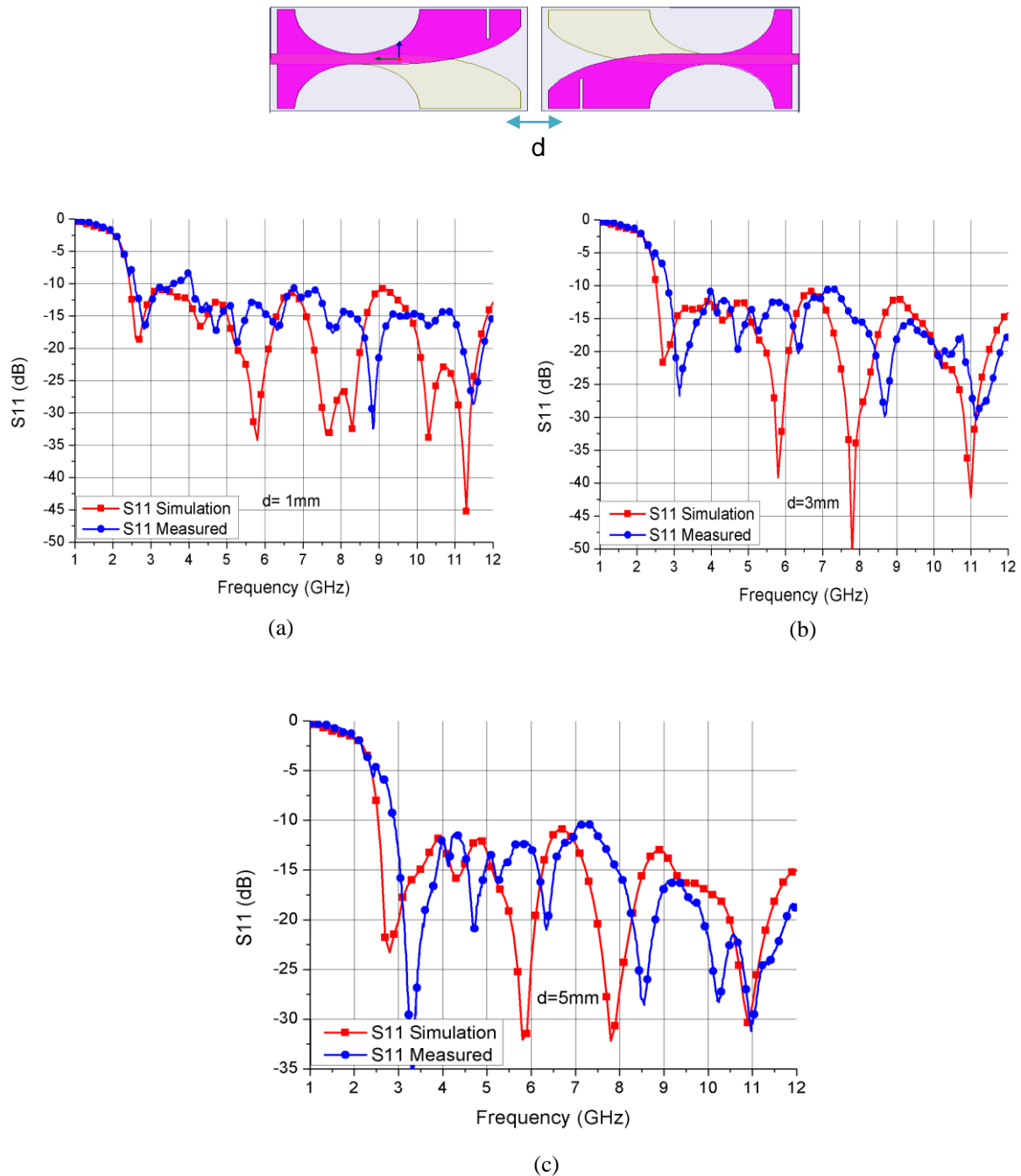
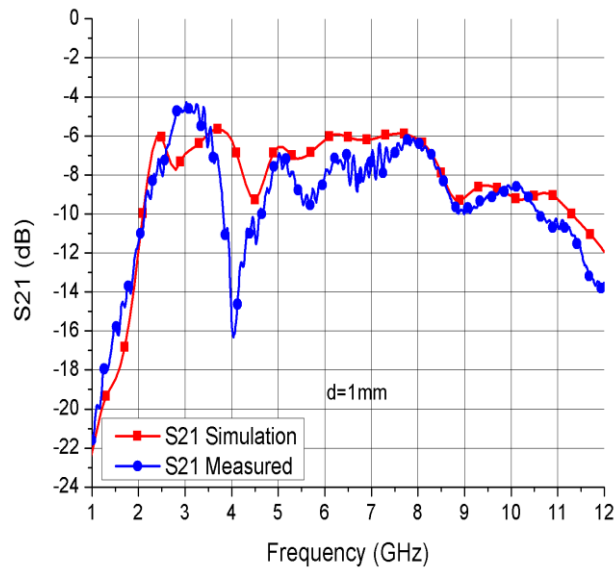
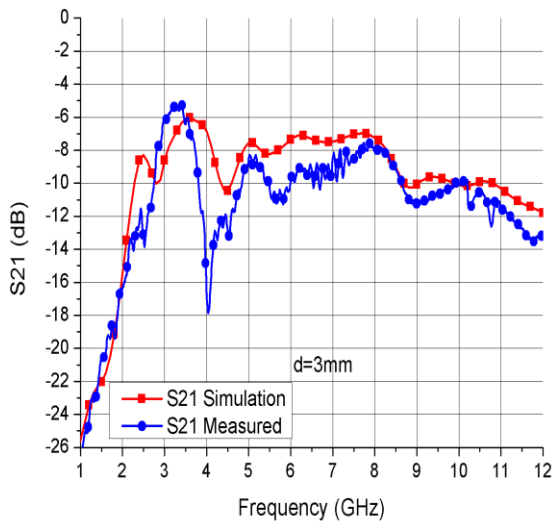


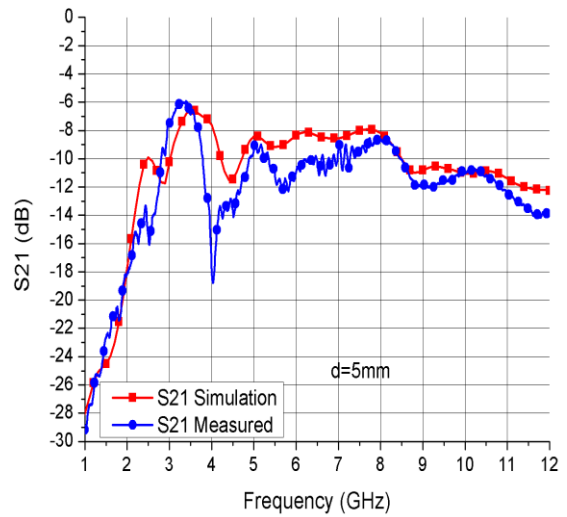
Figure B.6 Simulations and measurements of S_{11} parameters for two AVAs in an aligned configuration separated by (a) a distance $d=1\text{mm}$. (b) $d=3\text{mm}$. (c) $d=5\text{mm}$. The layout on the top shows the geometrical configuration.



(a)



(b)



(c)

Figure B.7 Simulations and measurements of S_{21} parameters for the two AVAs in an aligned configuration separated by (a) a distance $d=1\text{mm}$. (b) a distance $d=3\text{mm}$. (c) a distance $d=5\text{mm}$.

Table B.1: Comparison of our designed customized AVA with some other AVA from the literature.

AVA	Dimension L*W (mm ²)	Substrate Material	Operating Frequency (GHz)	Gain (dB)
[1]	95*100	FR4	3.1 to 10.6	6-8
[2]	60*78	FR4	2.4 to >14	3.7-10
[3]	40*35.6	FR4	3.1 to 10.6	1-5
[6]	66.4*50	-----	4 to >30	5-7
[8]	43*25	FR4	3 to 11	1-6.2
this work	50*30	FR4	2.5 to >12	0.5-6

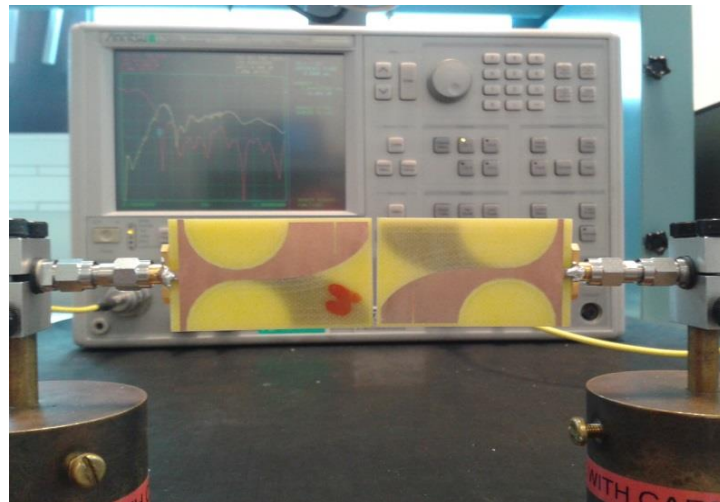


Figure B.8 Measurement setup of two aligned AVAs

The results have been published in:

F. Abayaje, P. Febvre, "A Customized Reduced Size Antipodal Vivaldi Antenna for Transmission of Cryogenic Backend Digital Data," ESA/ESTEC Antenna workshop 6-9 October, 2015.

Bibliography

- [1] C. B. Hien, S. Hiroshi, and D.N. Chien, "Analysis and Design of Antipodal Vivaldi Antenna for UWB Applications," Communications and Electronics (ICCE), IEEE 5th International Conference, pp. 391-394, 30 July-1 Aug. 2014.
- [2] F. Peng, J. Yong-chang, H. Wei, and Z. Fu-shun,"A Miniaturized Antipodal Vivaldi Antenna with Improved Radiation Characteristics," IEEE Antenna and Wireless Propagation Letters vol.10, pp. 127-130, 2011.
- [3] Z. Aaron, K. Tutku, and T. Erdem," A Small Antipodal Vivaldi Antenna for Ultra-wide Band Applications," IEEE Antenna and Wireless propagation Letters, vol.7, pp. 656-660, 2008.
- [4] Z. Wang, Y. Yin, J. Wu, R. Lian, "A Miniaturized CPW-Fed Antipodal Vivaldi Antenna with Enhanced Radiation Performance for Wideband Applications," IEEE Antenna and Wireless Propagation Letters, vol. 15, pp. 16-19, 2016.
- [5] J. Y. Siddiqui, Y. M. M. Antar, A. P. Freundorfer, E. C. Smith, G. A. Morin, and T. Thayaparan,"Design of an Ultra-wideband Antipodal Tapered Slot Antenna Using Elliptical Strip Conductors," IEEE Antennas Wireless Propagation letters, vol. 10,pp 251-254, 2011.
- [6] G. Teni, N. Zhang, J. Qiu, and P. Zhang," Research on a Novel Miniaturized Antipodal Vivaldi Antenna with Improved Radiation," IEEE Antennas and Wireless Propagation Letters, vol. 12, pp. 417-420, 2013.
- [7] A. M. Abbosh, and M. E. Bialkowski, "Design of Ultra- Wideband Planar Monopole Antenna of Circular and Elliptical Shape," IEEE Transactions on Antenna and Propagation, vol. 56, pp. 17-23, 2008.
- [8] Y. X. Che, Li, K., X.Y. Hou, and W.M.Tian," Simulation of A Small Sized Antipodal Vivaldi Antenna for UWB Applications," ICUWB. Nanjing, China, pp. 1-3, 20-23, 2010.
- [9] S. E. Hosseini, A. R. Attari, A. Pourzadi, "A Multiband PIFA with a slot on the Ground Plane for Wireless Applications," International Journal of Information and Electronics Engineering.vol. 3, no. 4, pp. 349-352, July 2013.